Leveraging Eigenvalue Veering for Improved Sensing with Microelectromechanical Systems

by

Gregory Peter Reynen

B.Sc., Queen's University, 2010

A THESIS SUBMITTED IN PARTIAL FULFILLMENT OF

THE REQUIREMENTS FOR THE DEGREE OF

MASTER OF APPLIED SCIENCE

in

THE FACULTY OF GRADUATE STUDIES

(Electrical and Computer Engineering)

THE UNIVERSITY OF BRITISH COLUMBIA

(Vancouver)

July 2012

Abstract

Energy localization in nearly periodic microsystems can be leveraged to create a new sensing paradigm that is orders of magnitude more sensitive than current resonant-frequency based systems. In this thesis, the theory which supports this claim is independently developed from a mathematical description of a two degree-of-freedom resonant system.

A novel proof-of-concept microelectromechanical system (MEMS) was also designed and fabricated to support the theoretical claims. The system employed a unique resonator design with two different approaches to inducing asymmetry in the system which in turn leads to the localization of energy in one of the resonators. The system proved the resonant frequency dependence on disorder in the system and also showed that the eigenvector sensitivity to disorder was at least an order of magnitude greater than the frequency sensitivity. However, the eigenvector sensitivity could not be matched with theory. This was likely due to the time-varying nature of the coupling spring stiffness (up to a 300% change in magnitude). The coupling spring stiffness was time-varying due to the inverse cubic relationship to coupling gap distance. The gap distance changes with time since it is practically impossible to excite only the common mode, leading to a superposition with the anti-phase mode. This was partially due to the input signal displaying non harmonic tendencies. At the same time, energy localization in the system leads to different amplitudes of vibration for each resonator which will also lead to gap distance modulation.

A three degree-of-freedom system was also examined theoretically with different approaches to stiffness perturbation and the resultant sensitivity expressions which can be leveraged for improved sensors were developed. The analysis shows that three degree-of-freedom systems can yield a 250% improvement over two degree-of-freedom systems which themselves are practically able to provide three to four order of magnitude improvements in sensitivity over resonant-frequency based sensors of the same size.

The tools and insight needed to design for higher degree-of-freedom system are also provided in the form of the eigen-derivatives approach to calculating eigenvalue and eigenvector sensitivity to disorder in a symmetric system.

Preface

Acquiring and processing the data in Chapter 3 was a collaboration between me, Dr. E. Cretu and Dr. A. Phani. I collected the data with assistance in learning how to use the equipment from Mrigank Sharma. The data was primarily analyzed in Mathematica by Dr. Cretu and in Matlab by Dr. Phani with assistance from me in the form of explaining the structure of the original data files and some scripting. The analyzed data was prepared for inclusion in this thesis by me.

Table of Contents

List of Tables

List of Figures

Acknowledgements

I would like to acknowledge the assistance and supervision of Dr. Edmond Cretu and Dr. A. Srikantha Phani for guiding me through the past two years at this school. Particularly, I would like to thank Dr. Phani for his mastery of the mathematics and theory of curve veering and Dr. Cretu for his expertise in MEMS.

I would be remiss to exclude the great contributions made by Siamak Moori, whose insight when reviewing the literature was invaluable, and Mrigank Sharma, whose familiarity with the laboratory equipment helped mitigate the frustration inherent in experimental testing.

Outside of a formal school setting, I would like to thank my friends Will Beattie, Peter Georgas, and Lindsay Wynne for impromptu conversations about my work.

With regards to the 3MT (Three Minute Thesis) Competition, I appreciate the audience that came to support me with their presence. They were Will Beattie, Brian Cheng, Elie Sarraf, and Wei You as well as the others who listened to me practice and gave feedback.

Finally, my parents are owed a huge debt for being stable sources of support, not just over the two years of this program, but for all of my previous endeavours.

Dedicated to my friends and family

Chapter 1: Introduction

1.1 Overview

The basis of this work is found in a fundamental understanding of the dynamic response of coupled resonant systems. The simplest resonant systems are analogous to a mass on a spring exhibiting simple harmonic motion. This system has a single degree of freedom and, as a result, has a single natural frequency with which it will oscillate. In more complex systems with multiple degrees of freedom (MDOF), there are multiple natural resonant frequencies, each associated with a resonant mode. The simplest example of a coupled system is perhaps two pendulums whose motions are linked by a spring. This system has two degrees of freedom (2DOF) and thus two resonant frequencies with two associated resonant modes. The first mode is the in-phase mode in which the direction of motion of each pendulum is the same. In this mode the coupling spring does zero work and therefore the frequency of motion is the same as that for a single pendulum (providing the coupled pendulums are identical). The second mode is the anti-phase mode. In this mode the directions of motion of each pendulum are always opposite of each other. In the case of a mechanical spring, the resonant frequency associated with this mode will be higher. For an electrostatic coupling, the associated resonant frequency for the anti-phase mode will be lower. This will be discussed further in Sections 1.2.3 and 2.2.

In the case that the constituent resonators of the system are not identical, energy injected into the system will be confined in a part of the system. This is called “mode localization” and is the basic idea on which the sensing paradigm presented here is

based. Physically, mode localization appears as a spatial concentration of energy in a nearly-periodic system and the term is used synonymously with energy localization. For the pendulum example, the amplitudes of vibration can be used as the measure of energy. A portion of this work was presented in February 2012 in the UBC Three Minute Thesis Competition in which it received first place in the Department of Electrical and Computer Engineering.

1.2 Historical Background

The prior research that leads to this work can be split into three time periods. The first is concerned with the recognition of a mode localization phenomenon in solid state physics and subsequent application to acoustics problems. The second is the combination of mode localization with the curve veering aberration (to be explained later). The third is the current application of this theory to a sensing paradigm in microelectromechanical systems (MEMS).

1.2.1 Mode Localization in Solid State Physics and Acoustics

The idea of mode localization was first identified in the context of solid-state physics. In a paper from 1958, Anderson describes a physical phenomenon in which wave functions of spins or electrons are localized in space within a three dimensional lattice [1]. Here the localization occurs due to impurities in the lattice structure which prevent transport across some coupling between spin sites [1]. One of the most important distinctions that are made in Anderson's work is that the model of the lattice in which this localization occurs cannot be in contact with some external energy source (a thermal reservoir in this case) which would force transport and thus overpower the phenomenon [1].

Over the following decade, numerous papers built on Anderson's work but the focus was on localization of electrons or magnetizing spins (called Anderson localization in the context of condensed matter physics). Some of the most notable advances were by N.F. Mott in papers from 1967 [2], 1968 [3], and an empirical demonstration of Anderson Localization in 1969 [4]. In fact, Anderson and Mott shared a Nobel Prize with van Vleck in 1977 for "*their fundamental theoretical investigations of the electronic structure of magnetic and disordered systems"* [5]. Beginning around the early 1970's, there appeared papers which referenced Anderson's earlier work and investigated localization of physical vibrations in nearly periodic structures [6]. In the 1980's several scientists combined the work of Rayleigh and Anderson to focus on mode localization in acoustics.

One of these early papers, published in 1981 and authored by C.H. Hodges, focused on using energy confinement in a structure in order to limit the local influence of a vibration source which was physically located somewhere else in the system [7]. This paper was the first to examine the phenomenon of mode localization in the context of acoustics and the author spends a great deal of effort in drawing parallels between the work of Anderson and Mott in solid state physics and the wider realm which includes structural dynamics.

Several other papers appeared in the 1980's including an experimental paper by Hodges and Woodhouse which followed up the theory presented in the 1981 paper [8]. This paper exhibits mode localization in a system of masses (small beads) along a string in which the mass spacing is slightly irregular and compares the measured results to the theoretical energy confinement based on a coupled pendulum model

[8]. Also in this decade, Pierre et al. built off the work of Hodges in order to describe a perturbation approach to predicting the behaviour of localized modes [9].

At this point, mode localization was a well known phenomenon, even if the mathematics of higher order systems were not completely understood. However, there remained one more step before mode localization could be extended to use in sensing rather than confined for use in understanding the dynamic behaviour of structures.

1.2.2 Eigenvalue Loci Veering

An extremely important advancement to the theory of mode localization came in 1988 in another paper by Pierre. In this paper, Pierre was the first to associate eigenvalue loci veering with mode localization [10]. In structural dynamics it is not uncommon to plot the loci of the eigenvalues of a system against a chosen system parameter. This type of plot can exhibit a strange behaviour first explored by Leissa in a 1974 paper in the context of plate vibrations [11]. When the loci of two eigenvalues approach each other, they do not intersect. Rather, they veer abruptly and continue on a path that would have been taken by the other eigenvalue if they had intersected [11]. In addition, the mode shapes are swapped in the transition zone [10]. The abruptness of the veering is related to the degree of coupling between the modes in the system, with a weaker coupling leading to a shorter transition zone and thus a more abrupt veering [10].

This behaviour is shown in Figure 1.1. The three sets of curves (red, blue, and green) correspond to different magnitudes of coupling between two degrees of

freedom in a system. The red curves[1] correspond to the highest coupling magnitude (i.e. stiffer coupling spring) and therefore the widest transition zone. The green curves correspond to the lowest magnitude of coupling and exhibit an abrupt transition zone. In other words, a smaller perturbation in the green system will cause a greater degree of energy localization when compared to the red system. The system parameter is “disorder”. It is a measure which compares the ratio of a change to the stiffness of one resonator to its natural stiffness or equivalently, the ratio of the change in mass of one resonator to its natural mass. Therefore ‘0’ disorder corresponds to a system of two identical, coupled oscillators.

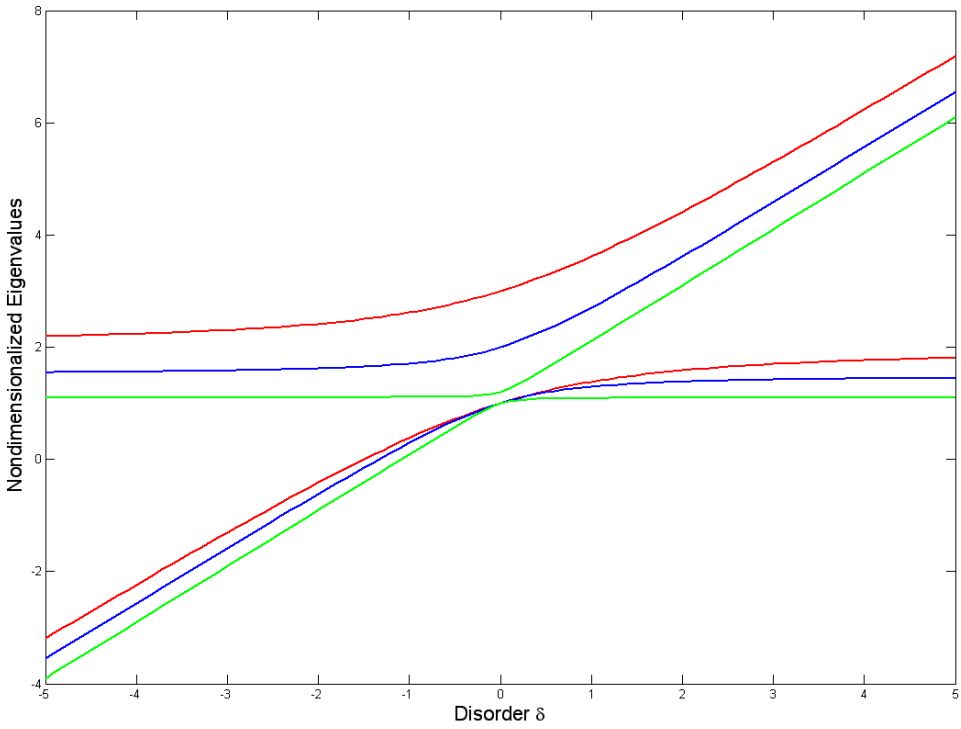

Figure 1.1: Loci of eigenvalues for a two degree of freedom system with varying magnitudes of coupling plotted against a measure of asymmetry in the stiffnesses of the resonators

[1] There are two curves of each colour. Each curve is the locus of one of the eigenvalues. Since there are two degrees of freedom, there are two eigenvalues and subsequently two loci.

In Figure 1.2, it is shown how the eigenvectors change with the disorder parameter by plotting three different eigenvectors per locus. In this simple illustration, the magnitude in the x-axis of the eigenvector plots represents the amplitude of vibration of the first oscillator and the magnitude in the y-axis represents the amplitude of the second oscillator. These eigenvector plots demonstrate the swapping of eigenvectors at either end of the transition zone.

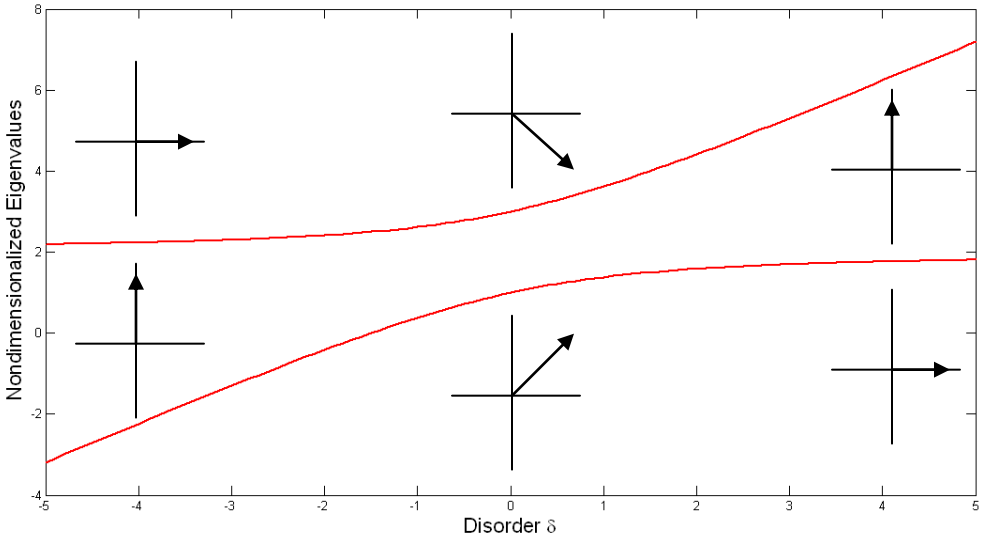

Figure 1.2: Visualization of eigenvector swapping in the transition zone

In Pierre's work and above, the eigenvalue loci are plotted versus a parameter representing the degree of disorder in the system (as in Figure 1.1 and Figure 1.2) [10]. One way to think about this disorder parameter is to consider two identical oscillators. A small perturbation can be introduced to the system in the form of a small additional mass on one of the two objects. In this case, the disorder would be the magnitude of the additional mass divided by the mass of either oscillator (since the masses are equal before the perturbation). Equivalently, the disorder can be induced as a stiffness perturbation while the mass of each oscillator remains static. It

is essential that when considering a stiffness perturbation it is not confused with adjusting the coupling stiffness. Instead, the stiffness perturbation is a small change in the stiffness of the spring which links an oscillator to a reference point. This distinction will be made clear in Section 2.1 when 2DOF systems are examined in greater detail.

Pierre describes both eigenvalue loci veering and mode localization as "*catastrophic type phenomena because small changes in the system parameters result in large variations in the eigenvalues and the mode shapes, respectively*." [10]

As an addendum to the veering theory, MacKay and Saffman used general results for Hamiltonian systems to show a criterion for veering between two eigenvalues, termed "avoided collision" in their work [12]. According to this work, when two eigenvalues exhibit codirectional coupling (their slopes have the same sign) the eigenvalue loci will avoid crossing by veering [12]. This work is elaborated on by Mace in 2012 who also notes that the phenomenon is present not only in undamped systems, but also in systems in which the damping is similar for each oscillator [13]. The veering phenomenon in systems with proportional damping is examined in this thesis in Chapter 2.

Finally, a small correction to Pierre's view of veering was made by Stephen in 2009 [14]. In Pierre's work, veering is only considered possible if the coupling between oscillators is "weak". However, Stephen shows that veering is present for any finite (and non-zero) coupling stiffness [14]. However, the width of the transition zone grows with increasing coupling stiffness, and therefore the severity of veering is reduced. Later in this thesis it will be shown that in order to improve the sensitivity of

sensors over current resonant frequency based sensors, a weak coupling is still required. The definition of “weak coupling” is also derived.

1.2.3 Current State of Research

In the last few years there has been a focus on applying the concept of eigenvalue veering in systems that exhibit mode localization for sensing purposes. The basic proposal begins with the assumption that the motions of each resonator in an identical MDOF system can be observed. When some disorder (a perturbation) breaks the symmetry of the system, the motions of each individual resonator will change abruptly, even if the perturbation is small. This change in motion leads to a sensing paradigm since each unique change can be mapped to a physical quantity through an understanding of how that physical quantity can perturb the coupled system.

The first example of this was in 2006 by Spletzer et.al. [15]. In this paper, two identical microcantilevers were fabricated with a physical coupling in the form of a “coupling overhang” with the intention of sensing changes in mass. When a small mass was added to one of the resonators, its amplitude of vibration was severely diminished while the amplitude of vibration of the other cantilever increased, effectively localizing the system energy in the unperturbed cantilever. The amount by which the system changed demonstrated a two order of magnitude improvement over frequency shift based resonators of similar size as well as benefits from intrinsic common mode error rejection [15]. One drawback of the system as presented is that ideal conditions are created. That is, the resonators are studied in a non-damped environment (vacuum) and the perturbing mass is placed at the tip of one of the

cantilevers. This highly controlled environment leaves room for improvement in building sensors which can work in more practical environments. There is also the possibility of studying the resonators in a different pass band. In this case, each of the cantilevers resonates in its fundamental mode but there is opportunity to observe the veering phenomenon when the cantilevers resonate in some higher order harmonic mode.

Subsequent work by the same group coupled 15 micro cantilevers, again for use as a mass sensor [16]. This work showed a three order of magnitude improvement over a frequency shift based resonator, being able to detect the presence of a 10 pg borosilicate sphere [16]. Additionally, they found that the specific cantilever to which the mass was applied produced a unique eigenmode shift. It is posited that this characteristic can lead to simultaneous detection of multiple analytes at the expense of requiring 15 output signals (one for each resonator) [16].

In 2008, DeMartini et al. also fabricated and studied a system for mass detection of multiple analytes using a slightly different approach than Spletzer et al. [17]. In this case, four microcantilevers were coupled to a single shuttle mass with each cantilever being sensitive to a different chemical. Each cantilever was also made a substantially different length so that their resonant frequencies were distinct. In order to make measurements, the common shuttle mass was excited with a large bandwidth signal. The motion of the common shuttle mass would then exhibit the superposition of four resonant modes, one for each cantilever. When any of the cantilevers was bound to by a target molecule, the motion of the common shuttle would change. By plotting this motion in the frequency domain, the mass of the

molecule, and its type could be determined [17]. This system does not leverage the veering phenomenon but is included as an example of a multi-degree of freedom sensor. Furthermore, this is a single input-single output (SISO) system which is much simpler than a veering system in terms of number of measurements (one output signal versus one per resonator for a total of 15 signals in Spletzer's work) but suffers from much worse sensitivity.

The work by Spletzer et al. demonstrates the power of eigenvalue veering as a sensing paradigm but it lacks tunability. A research group from the University of Cambridge that includes Woodhouse (the same Woodhouse who performed pioneering work mentioned in Section 1.2.1) has also delved into MEMS sensors based on eigenvalue veering but have used electrostatic coupling between resonators [18]. Electrostatic coupling of resonators is based on electrostatic attraction between two surfaces of different DC polarization voltage that are separated by a small gap. The attraction exhibits spring-like behaviour but the direction of action is opposite that of a mechanical spring. More specifically, the strength of the spring falls with the cube of the distance between the resonators rather than increasing linearly as with a mechanical spring [18]. This behaviour is captured in the following equation [18].

$$k_c = -\frac{\Delta V^2(\varepsilon_0 A)}{g^3} \tag{1.1}$$

In (1.1), the coupling is summarized as being proportional to the square of the difference between the DC polarization voltages (ΔV^2), proportional to both the permittivity of free space and mutual area (ε_0 and A, respectively) and inversely

proportional to the cube of the gap distance between the resonators (g^3). The derivation of this expression can be found in Appendix A.

The Cambridge group has also demonstrated two practical sensors, both in 2010. The first was an example of a mode-localized mass sensor using the electrically tunable coupling principle described by (1) [19]. By utilizing electrostatic coupling, the parametric sensitivities of the sensors were tunable by over 400% [19]. This mass sensor was based on identical MEMS ring oscillators and showed performance improvements of three orders of magnitude over a single uncoupled resonator [19].

The second sensor, also published in 2010, was an example of an electrometer based on the coupling of two double-ended tuning fork (DETF) resonators [20]. In this case the resonators are mechanically coupled at the base by means of a beam [20]. The perturbation is introduced into the system through electrostatic attraction, identical in principle to the electrostatic coupling introduced earlier. The force of attraction modifies the effective stiffness of one of the resonators. This is done by anchoring both ends of one resonator but only one end of the other. The unanchored end is suspended on a frame which allows motion only in the axial direction. A capacitor is formed between the end of the resonator and a charge input port. When a static charge is applied to the input port, an axial strain is generated in the second resonator. This strain induces a change in stiffness and subsequently mode localization [20]. High performance improvements over single resonator frequency based designs are again demonstrated however the advantage for this design is slightly less than three orders of magnitude [20]. This may be due to the use of

mechanical coupling which was not tuned optimally to the application rather than a tunable electrostatic coupling.

More recently in 2011, a paper by Gil-Santos et al. investigated a sensing topology very similar to that of Spletzer et al. The focus of this investigation was to quantify the effects of modifying the separation of microcantilevers, and thus the length of the coupling overhang [21].The main takeaway of this work confirmed the findings of the Cambridge group. That is, weaker coupling enhances the localization of energy and thus improves the sensitivity of the sensor regardless of whether the weak coupling is produced through electrostatic attraction, or by long mechanical couplings in microcantilever designs.

1.3 Research Problem

In this thesis the use of mode-localization will be explored further with an emphasis on suitability for inertial sensing applications. Specifically, research into the following areas is presented:

- Mode-localization in a real MEMS 2DOF system using plate resonators and electrostatic coupling
- Two different approaches to inducing a stiffness perturbation (one approach based on electrostatic attraction and one approach based on direct mechanical linkage)
- Theoretical approach to 3DOF systems and beyond as a stepping stone to future highly sensitive sensors

The work presented here is general to sensing as an area of research since the designs used do not measure any specific quantity. Rather, the veering

phenomenon is examined in-depth when a controlled perturbation is applied. In theory, this work can be applied to any sensor as long as the physical quantity to be measured (e.g. acceleration, mass, angular rate, etc.) causes a perturbation to one of the characteristics of the coupled system.

1.4 Thesis Organization

The remainder of this thesis will be organized as follows. Chapter 2 will delve more deeply into the theory of curve veering and mode localization including a complete analytical description derived from first principles for a 2DOF system. The analytical work is supported by numerical simulations showcasing the phenomenon. Chapter 3 focuses on the design of four different MEMS resonator pairs and experimental characterization of one of those pairs. This includes a discussion of the design choices and implications of those choices as well as experimental results. Chapter 4 lays the groundwork for later work on chains of three resonators or more. Here it is shown analytically that even greater sensitivity improvements can be expected of these systems. Chapter 5 summarizes the findings while Chapter 6 suggests several avenues for future research that are natural progressions from the work presented here.

Chapter 2: Two Degree of Freedom Systems

2.1 Introduction

An undamped two degree of freedom (2DOF) system is the simplest case in which the veering phenomenon can be observed. Analytical expressions for the sensitivity of resonant frequencies and eigenstate vectors to stiffness perturbations for 2DOF systems have already been developed using a work interpretation without damping [18]. Here, a state space approach will be used which supports the results found in [18], while also discussing the applicability to a proportionally damped system. As has been previously discussed, the veering phenomenon is pronounced in systems of periodic (i.e. identical and repeated) coupled structures. The instance of a 3DOF system and extensions to higher order systems will be explored in Chapters 4 and 6.

2.2 Analysis of a 2DOF System

2.2.1 Schematic and Mathematical Description of System

The analysis of a 2DOF system is based on the spring-mass-damper system depicted in Figure 2.1. This schematic considers two masses (m_1 and m_2) which are grounded by springs k_1 and k_2 respectively. The two masses exchange energy through a coupling spring k_c (with associated damping c_c). In addition to the grounding springs, each resonator section has an associated damping parameter, c_1 and c_2 respectively. A perturbation to the symmetry in the system is represented by a second ground spring on m_2. This spring (Δk), contrary to physical springs, is permitted to have a negative spring constant in order to preserve the generality of the results for both mechanical springs and the electrostatic couplings which exhibit negative spring constants.

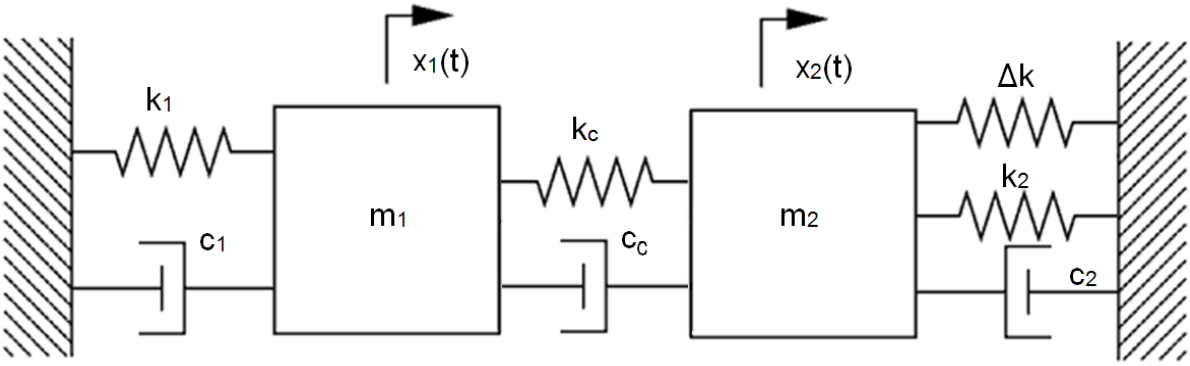

Figure 2.1: Schematic of a coupled 2DOF spring-mass-damper system

The equations of motion for this system are as follows:

$$m_1\ddot{x_1} + c_1\dot{x_1} + c_c(\dot{x_1} - \dot{x_2}) + (k_1 + k_c)x_1 - k_c x_2 = f_1 \tag{2.1}$$

$$m_2\ddot{x_2} + c_2\dot{x_2} + c_c(\dot{x_2} - \dot{x_1}) + (k_2 + k_c + \Delta k)x_2 - k_c x_1 = f_2 \tag{2.2}$$

From this point the system will be assumed symmetric. In other words, $m_1 = m_2 = m$, $k_1 = k_2 = k$, and $c_1 = c_2 = c$. The equations are also rewritten in matrix form.

$$\boldsymbol{M}\ddot{\boldsymbol{x}} + \boldsymbol{C}\dot{\boldsymbol{x}} + \boldsymbol{K}\boldsymbol{x} = \boldsymbol{f} \tag{2.3}$$

$$\boldsymbol{M} = \begin{bmatrix} m & 0 \\ 0 & m \end{bmatrix} \qquad \boldsymbol{C} = \begin{bmatrix} c + c_c & -c_c \\ -c_c & c + c_c \end{bmatrix} \qquad \boldsymbol{K} = \begin{bmatrix} k + k_c & -k_c \\ -k_c & k + k_c + \Delta k \end{bmatrix} \tag{2.4}$$

2.2.2 Proportional Damping

For undamped or proportionally damped systems, the undamped modal column matrix (Φ) diagonalizes all three of the above matrices. A proportionally damped system is one in which the damping matrix can be represented as a weighted linear combination of the mass and stiffness matrices. The weighting is represented by the two weighting factors α and β as in the following equation.

$$\boldsymbol{C} = \alpha\boldsymbol{M} + \beta\boldsymbol{K} \tag{2.5}$$

The assumption of proportionally damped systems is valid in this research since the physical systems are designed to be symmetric. The dimensions are identical and,

as will be discussed in Chapter 3, the geometry of the real system is defined by a single mask in a mature fabrication technology (SOIMUMPS). This ensures each structure is practically a perfect copy. Furthermore, the resonators have a very small spatial separation meaning they operate in an identical environment. This situation allows for the assumption that the damping factor will be the same for each resonator and thus the definition of proportional damping is met. Essentially, since Δk is very small ($k + \Delta k \approx k$), the damping matrix is simply a weighted version of the stiffness matrix. That is, β is some appropriate value based on geometry, environment etc. and α is zero.

The normalized eigenstate vectors of a proportionally damped system are the same as that for an undamped system. Therefore the sensitivity equation found here for the eigenvectors is applicable to both cases. For the case of normalized eigenvalues, the solutions are not identical for undamped and proportionally damped systems. In general, damping will change the fundamental frequencies of the system's response. However, in MEMS devices damping is usually very low so for the purposes of this research a comparison will be made between the sensitivities of the normalized eigenstate vectors (which are applicable to undamped and proportionally damped systems) and the sensitivity of the system's eigenvalues (which are only applicable to proportionally damped systems in addition to undamped systems if damping is considered to be very low).

2.2.3 The Eigenvalue Problem and Solution

Assuming a solution to the displacement vector of the form

$$\boldsymbol{x}^T = [x_1\ x_2]^T = \boldsymbol{u_n}\, e^{-j\omega_n t}\ (n = 1,2) \tag{2.6}$$

then the description of the undamped system can be rewritten as

$$\boldsymbol{K}\,\boldsymbol{u_n} = \omega_n^2\,\boldsymbol{M}\,\boldsymbol{u_n} \tag{2.7}$$

The subscript 'n' denotes the mode number. Since the system has two degrees of freedom, there are two unique modes. This will be discussed next when the eigenvalue problem has been fully defined and solved.

At this point, a modified stiffness matrix is defined as being the original stiffness matrix scaled by $1/k$.

$$\boldsymbol{K'} = \begin{bmatrix} 1+\kappa & -\kappa \\ -\kappa & 1+\kappa+\delta \end{bmatrix} \text{ where } \kappa = \frac{k_c}{k}\,, \delta = \frac{\Delta k}{k} \tag{2.8}$$

If the mass matrix is rewritten as the product of the mass variable (m) and the identity matrix, then the above equation becomes:

$$\boldsymbol{K'u_n} = \frac{\omega_n^2}{k/m}\,\boldsymbol{I u_n} = \lambda_n \boldsymbol{I u_n} \tag{2.9}$$

This is an eigenvalue problem with eigenvector $\boldsymbol{u_n}$ and an associated nondimensionalized eigenvalue λ_n. For this 2DOF system there are two solutions to this eigenvalue problem (it is quadratic) and they are presented here.

$$\lambda_1 = \frac{\delta}{2} + \kappa - \frac{\sqrt{\delta^2+4\kappa^2}}{2} + 1 \qquad \boldsymbol{u_1} = \begin{bmatrix} \dfrac{\delta+\kappa+1-\lambda_1}{\kappa} \\ 1 \end{bmatrix}$$

$$\lambda_2 = \frac{\delta}{2} + \kappa + \frac{\sqrt{\delta^2+4\kappa^2}}{2} + 1 \qquad \boldsymbol{u_2} = \begin{bmatrix} \dfrac{\delta+\kappa+1-\lambda_2}{\kappa} \\ 1 \end{bmatrix} \tag{2.10}$$

In the case of a perfectly symmetric system (i.e. $\delta = 0$) then the solutions to the eigenvalue problem reduce to:

$$\lambda_{01} = 1 \quad \boldsymbol{u_{01}} = \begin{bmatrix} 1 \\ 1 \end{bmatrix} \quad \text{and} \quad \lambda_{02} = 1 + 2\kappa \quad \boldsymbol{u_{02}} = \begin{bmatrix} -1 \\ 1 \end{bmatrix} \tag{2.11}$$

The first subscript '0' indicates that these solutions are for the unperturbed state and is only used in this special case. The second subscript indicates the mode number and in many cases will be the only subscript used. This convention will be consistent throughout this thesis.

2.2.4 Discussion of the Eigenvalue Problem Solution

This solution of the unperturbed 2DOF system is interpreted physically as representing two natural harmonic frequencies and their associated mode shapes. For a positive κ (that is, a positive spring constant coupling the two oscillators), the lower frequency has an associated in-phase mode shape. This mode shape can be described as the sign of displacements x_1 and x_2 being identical at all times and the amplitudes of displacement also being equal. Similarly, a second natural mode (the anti-phase mode) exists at a higher frequency in which the amplitudes of displacement are still identical but in this mode the signs of displacement are always opposite (180° out of phase). This solution for a 2DOF system is well known and easily verified. The solution also indicates that for negative spring coupling arrangements, such as those found with electrostatic coupling, the eigenvalue associated with in-phase motion will remain the same but the eigenvalue associated with anti-phase motion will have a magnitude that is smaller by 2κ. This can be proven intuitively by considering that for the in-phase mode the coupling spring does not do any work and thus the eigenvalue remains the same regardless of the magnitude or sign of the coupling spring's stiffness.

2.2.5 Normalized Modal Column Matrix

The solution eigenvectors are now normalized for unit modal mass. The two normalized vectors become the columns of the modal column matrix $\boldsymbol{\Phi}$. The normalization is performed using the equation:

$$\boldsymbol{\varphi_n} = \frac{\boldsymbol{u_n}}{\sqrt{(\boldsymbol{u_n^T u_n})}} \tag{2.12}$$

The normalized eigenvectors are then:

$$\boldsymbol{\varphi_1} = \begin{bmatrix} \dfrac{\frac{\delta}{2} + \frac{\sqrt{\delta^2 + 4\kappa^2}}{2}}{\kappa\left(\dfrac{\left(\frac{\delta}{2} + \frac{\sqrt{\delta^2 + 4\kappa^2}}{2}\right)^2}{\kappa^2} + 1\right)^{\frac{1}{2}}} \\ \dfrac{1}{\left(\dfrac{\left(\frac{\delta}{2} + \frac{\sqrt{\delta^2 + 4\kappa^2}}{2}\right)^2}{\kappa^2} + 1\right)^{\frac{1}{2}}} \end{bmatrix} \qquad \boldsymbol{\varphi_2} = \begin{bmatrix} \dfrac{\frac{\delta}{2} - \frac{\sqrt{\delta^2 + 4\kappa^2}}{2}}{\kappa\left(\dfrac{\left(\frac{\delta}{2} - \frac{\sqrt{\delta^2 + 4\kappa^2}}{2}\right)^2}{\kappa^2} + 1\right)^{\frac{1}{2}}} \\ \dfrac{1}{\left(\dfrac{\left(\frac{\delta}{2} - \frac{\sqrt{\delta^2 + 4\kappa^2}}{2}\right)^2}{\kappa^2} + 1\right)^{\frac{1}{2}}} \end{bmatrix} \tag{2.13}$$

For the perfectly symmetric system ($\delta = 0$), the modal column matrix is:

$$\boldsymbol{\Phi_{sym}} = \frac{1}{\sqrt{2}}\begin{bmatrix} 1 & -1 \\ 1 & 1 \end{bmatrix} \tag{2.14}$$

From this it is immediately obvious that the magnitudes of the constituent column vectors are, in fact, one.

For the general system including the possibility of stiffness perturbation, the modal column matrix is:

$$\boldsymbol{\Phi} = \begin{bmatrix} \dfrac{\Delta_1}{\kappa\sqrt{\dfrac{\Delta_1^2}{\kappa^2}+1}} & \dfrac{\Delta_2}{\kappa\sqrt{\dfrac{\Delta_2^2}{\kappa^2}+1}} \\ \dfrac{1}{\sqrt{\dfrac{\Delta_1^2}{\kappa^2}+1}} & \dfrac{1}{\sqrt{\dfrac{\Delta_2^2}{\kappa^2}+1}} \end{bmatrix} \text{where } \Delta_1 = \frac{\delta}{2} + \frac{\sqrt{\delta^2+4\kappa^2}}{2}, \Delta_2 = \frac{\delta}{2} - \frac{\sqrt{\delta^2+4\kappa^2}}{2} \quad (2.15)$$

The modal column matrix is then simplified by linearizing in δ around the point $\delta = 0$ representing small perturbations introduced into a symmetric system. The linearized modal column matrix is:

$$\boldsymbol{\Phi} \approx \frac{\sqrt{2}}{2}\begin{bmatrix} \dfrac{\delta}{4\kappa} + \dfrac{\sqrt{4\kappa^2}}{2\kappa} & \dfrac{\delta}{4\kappa} - \dfrac{\sqrt{4\kappa^2}}{2\kappa} \\ 1 - \dfrac{\delta}{2\sqrt{4\kappa^2}} & 1 + \dfrac{\delta}{2\sqrt{4\kappa^2}} \end{bmatrix} = \frac{1}{\sqrt{2}}\begin{bmatrix} 1 + \dfrac{\delta}{4\kappa} & \dfrac{\delta}{4\kappa} - 1 \\ 1 - \dfrac{\delta}{4\kappa} & \dfrac{\delta}{4\kappa} + 1 \end{bmatrix} \quad (2.16)$$

2.2.6 General Sensitivity Expressions

Before a comparison can be made of the relative sensitivities of the eigenvectors and the eigenvalues to perturbations in the symmetry of the 2DOF system, linearized expressions for the eigenvalues in δ around the point $\delta = 0$ are also found.

$$\lambda_1 \approx \frac{\delta}{2} + \kappa - \frac{\sqrt{4\kappa^2}}{2} + 1 = \frac{\delta}{2} + 1 \quad (2.17)$$

$$\lambda_2 \approx \frac{\delta}{2} + \kappa + \frac{\sqrt{4\kappa^2}}{2} + 1 = \frac{\delta}{2} + 2\kappa + 1 \quad (2.18)$$

Now an expression for the relative change in eigenvalues due to a perturbation is found for the first mode.

$$\lambda_{01} = 1 \quad (2.19)$$

$$\lambda_1 - \lambda_{01} = \frac{\delta}{2} \tag{2.20}$$

$$\frac{\lambda_1 - \lambda_{01}}{\lambda_{01}} = \frac{\delta}{2} = \frac{\Delta k}{2k} \tag{2.21}$$

Repeating the process for the second mode,

$$\lambda_{02} = 1 + 2\kappa \tag{2.22}$$

$$\lambda_2 - \lambda_{02} = \frac{\delta}{2} \tag{2.23}$$

$$\frac{\lambda_2 - \lambda_{02}}{\lambda_{02}} = \frac{\frac{\delta}{2}}{1 + 2\kappa} = \frac{\frac{\Delta k}{2}}{k + 2k_c} \text{ if } k_c \ll k \text{ then } \frac{\lambda_2 - \lambda_{02}}{\lambda_{02}} = \frac{\Delta k}{2k} \tag{2.24}$$

So, in general, the sensitivity of the eigenvalues of this 2DOF system can be expressed as:

$$\frac{\lambda_n - \lambda_{0n}}{\lambda_{0n}} = \frac{\Delta k}{2k} \tag{2.25}$$

An expression for the sensitivity of the eigenvectors is found similarly by using the columns of the modal column matrix. First, the first mode:

$$\boldsymbol{\varphi_{01}} = \begin{bmatrix} \frac{1}{\sqrt{2}} \\ \frac{1}{\sqrt{2}} \end{bmatrix}, |\boldsymbol{\varphi_{01}}| = 1 \tag{2.26}$$

$$\boldsymbol{\varphi_1} - \boldsymbol{\varphi_{01}} = \begin{bmatrix} \frac{\sqrt{2}\delta}{8\kappa} \\ -\frac{\sqrt{2}\delta}{4\sqrt{4\kappa^2}} \end{bmatrix}, |\boldsymbol{\varphi_1} - \boldsymbol{\varphi_{01}}| = \sqrt{\frac{\delta^2}{16\kappa^2}} = \frac{\delta}{4\kappa} \tag{2.27}$$

$$\frac{|\boldsymbol{\varphi_1} - \boldsymbol{\varphi_{01}}|}{|\boldsymbol{\varphi_{01}}|} = \frac{\delta}{4\kappa} = \frac{\Delta k}{4k_c} \tag{2.28}$$

And repeating for the second mode:

$$\boldsymbol{\varphi_{02}} = \begin{bmatrix} \frac{-1}{\sqrt{2}} \\ \frac{1}{\sqrt{2}} \end{bmatrix}, |\boldsymbol{\varphi_{02}}| = 1 \tag{2.29}$$

$$\boldsymbol{\varphi_2} - \boldsymbol{\varphi_{02}} = \begin{bmatrix} \frac{\sqrt{2}\delta}{8\kappa} \\ \frac{\sqrt{2}\delta}{4\sqrt{4\kappa^2}} \end{bmatrix}, |\boldsymbol{\varphi_2} - \boldsymbol{\varphi_{02}}| = \sqrt{\frac{\delta^2}{16\kappa^2}} = \frac{\delta}{4\kappa} \tag{2.30}$$

$$\frac{|\boldsymbol{\varphi_2} - \boldsymbol{\varphi_{02}}|}{|\boldsymbol{\varphi_{02}}|} = \frac{\delta}{4\kappa} = \frac{\Delta k}{4k_c} \tag{2.31}$$

So, in general the sensitivity of the eigenvectors of a 2DOF system can be expressed as:

$$\frac{|\boldsymbol{\varphi_n} - \boldsymbol{\varphi_{0n}}|}{|\boldsymbol{\varphi_{0n}}|} = \frac{\Delta k}{4k_c} \tag{2.32}$$

2.2.7 Comparison and Weak Coupling

By comparing equations (2.25) and (2.32) it is seen that the eigenvectors are more sensitive to perturbations than the eigenvalues when the following condition is met:

$$k_c < \frac{k}{2} \tag{2.33}$$

Equation (2.33) is thus the definition of weak coupling that is used throughout this thesis and describes the threshold at which improvements in sensitivity can be made over traditional resonant frequency tracking approaches. These results agree with results found independently in the literature [18].

It may have been noticed that when finding the sensitivity of the second eigenvalue to a perturbation, the equation was only valid for $k_c \ll k$. Above it is stated that it is sufficient for the coupling spring stiffness to be half of that of a grounding spring. If it

is the case where the coupling spring is half the stiffness of a grounding spring (and positive), the sensitivity of the eigenvalue of the second mode is actually $\frac{\Delta k}{4\mathrm{k}}$ which is an even lower sensitivity to perturbation than is found with the simplifying assumption. If it is the case where the coupling spring is half the stiffness of grounding spring (but negative), the sensitivity of the eigenvalue of the second mode is actually $\frac{\Delta k}{\mathrm{k}}$ which is twice as sensitive as the analytical expression would indicate and requires $k_c < \frac{k}{4}$ for sensitivity improvement with eigenvectors. However, since the coupling spring stiffness using electrostatic coupling is generally orders of magnitude less than the grounding springs this caveat to be ignored.

2.3 Practical Measurement Considerations

In this section one of the practical considerations regarding system design and measurements is analyzed. A possible solution to this practical consideration is suggested for use in systems which must balance complexity with accuracy.

2.3.1 Practical Considerations

In the 2DOF system, a perturbation affects both the eigenvalues and the eigenvectors. In Section 2.2.6 a sensitivity expression was developed considering the magnitude of the difference between the perturbed eigenvector and the unperturbed eigenvector, normalized by the magnitude of the unperturbed eigenvector. This approach is applicable when the frequency of the driving signal in the system tracks the changes in resonant frequency. That is, an unperturbed system is measured while being driven at the unperturbed resonant frequency and

subsequent measurements are made when driven at the new resonant frequency. Graphically the approach is shown in Figure 2.2.

Some notes regarding Figure 2.2 must be made. First of all, the basis for the coordinate system used is a unit vector representing displacement of the first mass, and a unit vector representing displacement of the second mass. Therefore, the

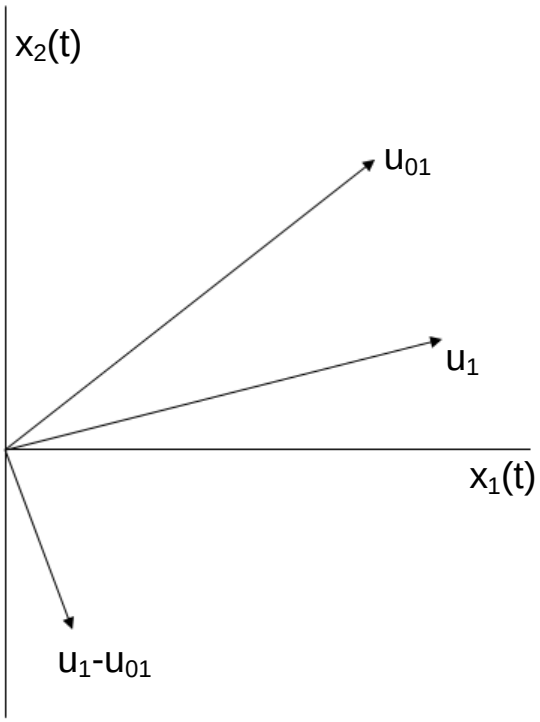

Figure 2.2: Graphical representation of the changes in eigenvectors

vector u_{01} represents in-phase motion of equal amplitude. This is expected for the unperturbed case. Vector u_1 represents the system after a perturbation which increases the stiffness or mass of the second resonator. The result, if the system has tracked the change in resonant frequency, is a vector of the same magnitude but the component that represents the first mass's displacement is larger than the component for the second mass. This indicates energy localization in the first mass.

If the driving signal does not track the change in resonant frequency, the magnitude of the vector after perturbation is not the same as the unperturbed vector. Graphically this can be shown as in Figure 2.3.

In this case the magnitude of vector u_1 is diminished and the error manifests quite severely, affecting the accuracy of the measurement. As a result, a different approach to examining the eigenvectors must be used when the system does not track the resonance frequency.

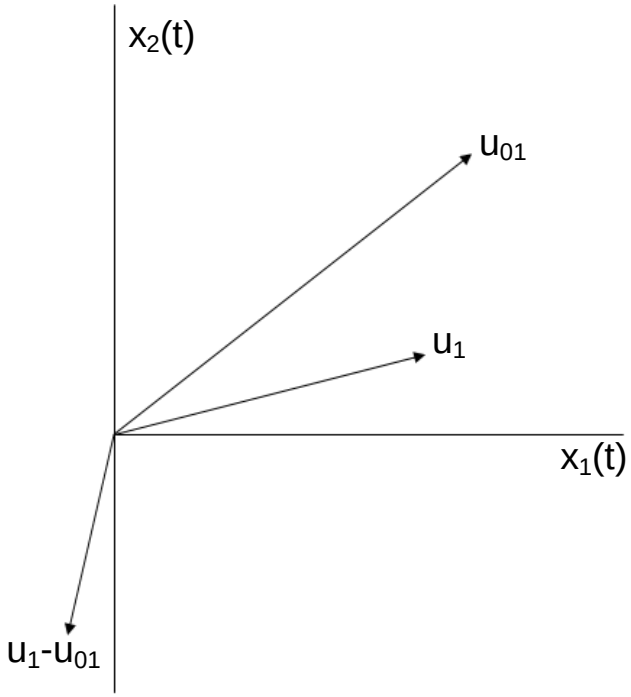

Figure 2.3: Graphical representation of the eigenvectors when resonant frequency is not tracked

2.3.2 Eigenvector Characterization for Non-Tracking Systems

Practically, it is more difficult to design a feedback system that tracks the resonant frequency. For open-loop systems, the angle of the eigenvectors can be used as a

substitute for the method introduced earlier. This method is described graphically in Figure 2.4.

Now the expression used for quantifying perturbations is:

$$\frac{\varphi_1 - \varphi_{01}}{\varphi_{01}} \qquad (2.34)$$

where φ_1 is an angle rather than a mass-normalized eigenvector. The same method can be used for the second mode of vibration.

One warning that must be mentioned when using this method is that exciting the system at a frequency different than one of the two natural frequencies will actually cause a superposition of both modes. This will affect both the angle and the magnitude of the perturbed eigenvector. However, the reduced amplitude of the eigenvector is more pronounced than a change in angle therefore the method of

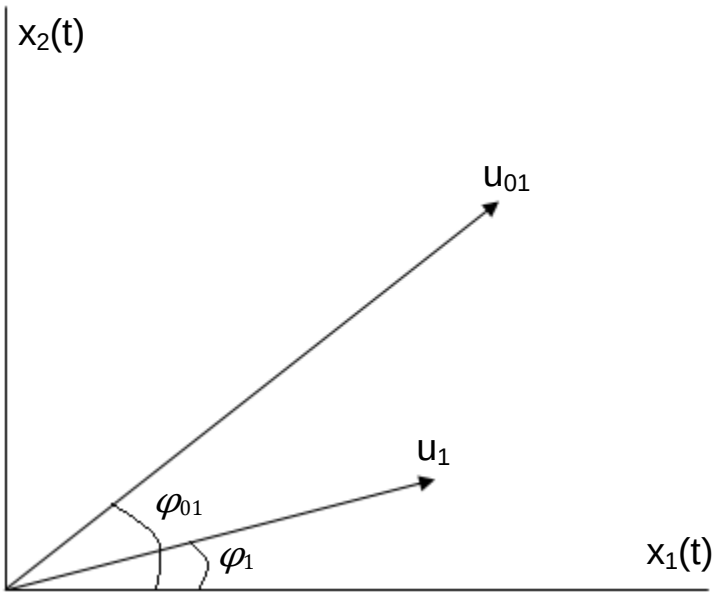

Figure 2.4: Graphical representation of measurement approach when resonant frequency is not tracked

measuring angle is superior and can be used for small perturbations. To find the angle of the eigenvector experimentally, the amplitudes of each mass are measured and the arctangent of the quotient of the components is computed.

2.4 Tunable Coupling Stiffness

It has been shown that the sensitivity of the eigenvectors to perturbation is inversely proportional to the magnitude of coupling. It may appear that the limit of sensitivity is then the practical problem of creating very weak springs. However, the expressions developed earlier are only applicable within the veering zone. As was explained in Section 1.2.2, the width of the veering zone is also dependent on the degree of coupling; greater coupling means a wider veering zone and vice versa. Therefore there is a tradeoff between sensitivity and the range of perturbations for which the technique is valid. In this section, the valid regions for three different degrees of coupling are presented graphically along with the associated change in resonant frequencies. The advantages of an experimental system with tunable coupling are also discussed.

2.4.1 Veering and Degrees of Coupling

The following set of figures compares the sensitivities of eigenvectors and eigenvalues to perturbations. These figures were produced by using the EIG function in MATLAB to find the eigenvalues and eigenvectors of a 2DOF system for different degrees of coupling and for a range of disorders. As seen in the figures, disorder is again defined as the change in stiffness of one of the masses, normalized by the magnitude of stiffness for the unperturbed mass and is denoted by 'δ'. The range of disorder is from -50% to +50%. In addition, a negative coupling coefficient

was used to be consistent with electrostatic coupling. This means the first mode of vibration (lower frequency) is the anti-phase mode and the second mode of vibration (higher frequency) is the in-phase mode. Three distinct degrees of coupling are explored; one relatively strong coupling (the coupling stiffness magnitude is 40% of a grounding spring), one weak coupling (coupling stiffness magnitude is 10% of a grounding spring), and one very weak coupling (coupling stiffness magnitude is 1% of a grounding spring). These figures are presented in pairs on the following pages.

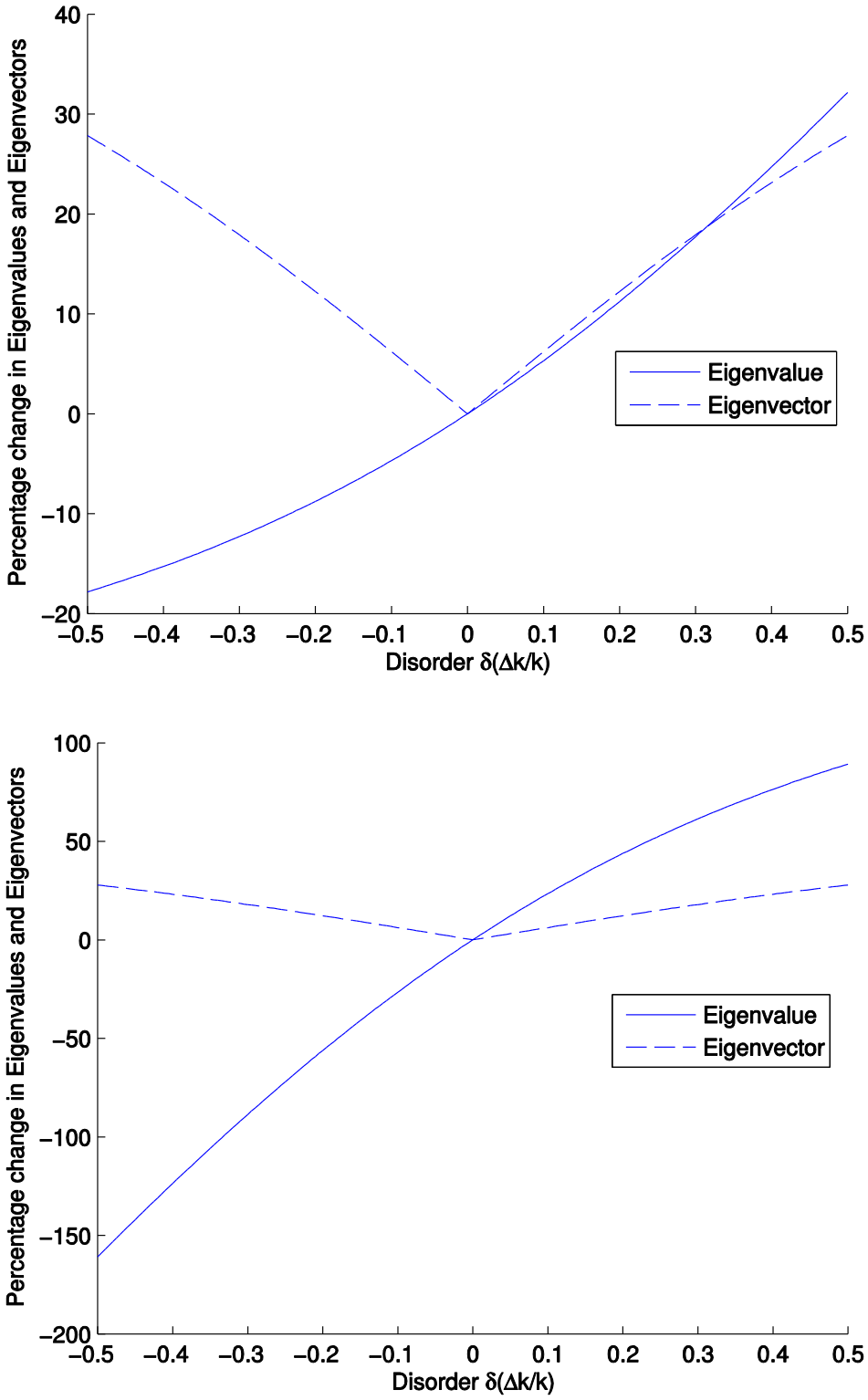

Figure 2.5: Comparing sensitivities with a coupling stiffness magnitude of 40% of a grounding spring. Top plot is the in-phase mode; bottom plot is the anti-phase mode.

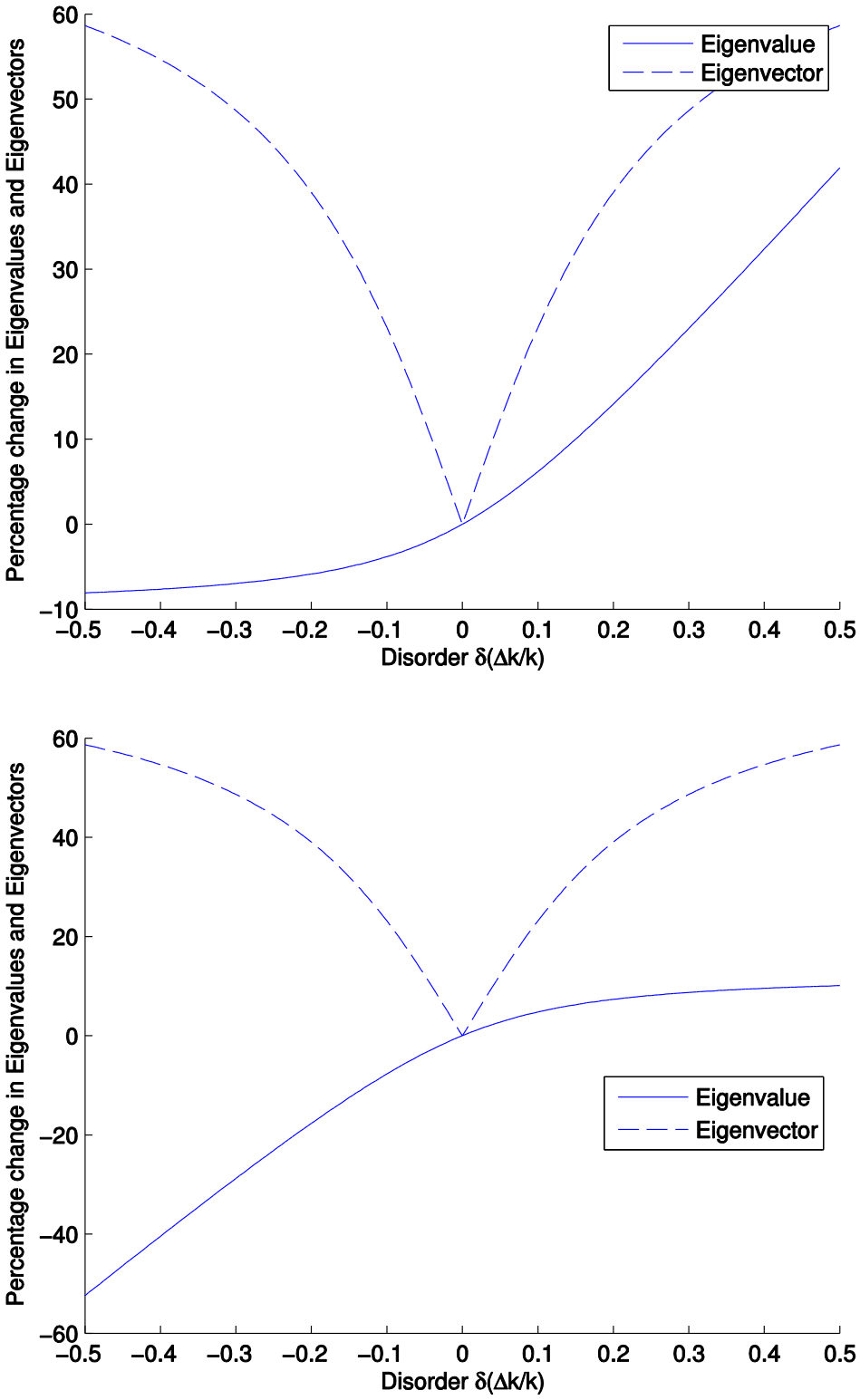

Figure 2.6: Comparing sensitivities with a coupling stiffness magnitude of 10% of a grounding spring. Top plot is the in-phase mode; bottom plot is the anti-phase mode.

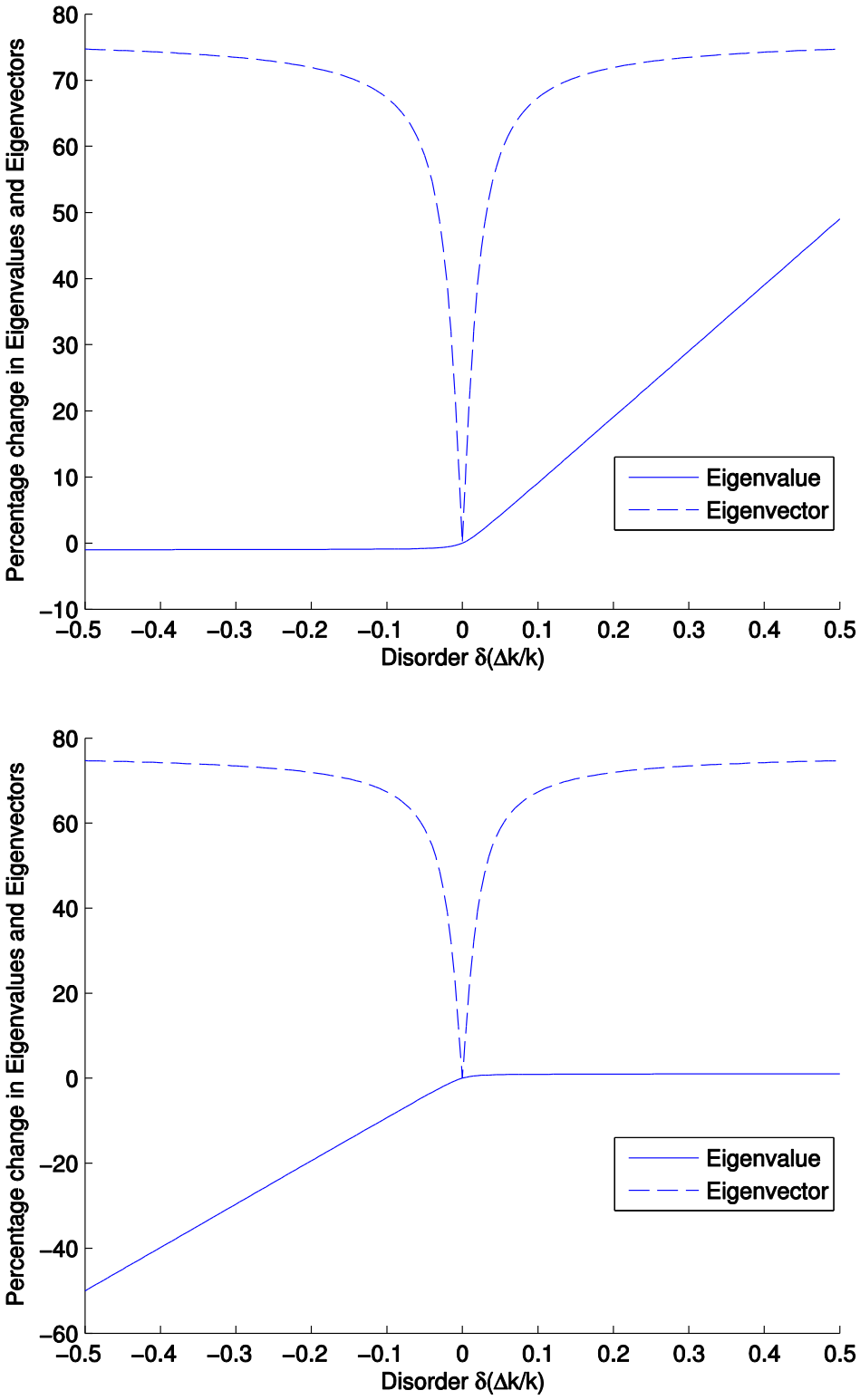

Figure 2.7: Comparing sensitivities with a coupling stiffness magnitude of 1% of a grounding spring. Top plot is the in-phase mode; bottom plot is the anti-phase mode.

Figure 2.5 - Figure 2.7 show graphically that the earlier expressions for sensitivity have a limited range for which they are valid, and that this range is a function of the stiffness of the coupling spring. It is also evident for the in-phase mode that as the stiffness of the coupling spring approaches 50% of a grounding spring, the slope of the eigenvectors curve becomes tangential to the eigenvalue curve. The same behaviour is not exhibited by the anti-phase mode for the reason discussed in 2.2.7. When comparing the theoretical results, remember that the anti-phase mode was the second mode of vibration in the earlier analysis but in the simulations in this section a negative coupling constant was assumed. At this point for the in-phase mode, any relative increase in stiffness of the coupling spring would result in higher sensitivity by tracking the eigenvalues rather than the eigenvectors.

Lastly, the eigenvector curves are symmetric about a cusp at the system's symmetry point. Based just on the graphical evidence, it seems as though a sensor leveraging this phenomenon is unable to differentiate between perturbations that positively affects stiffness and an equal in magnitude perturbation which negatively affects the spring. However, a comparison of the amplitudes of vibration for each mass at the perturbed state will reveal this additional information. If the amplitude of vibration is higher for the second mass, the perturbation decreased the stiffness of the second grounding spring and vice versa. The apparent uncertainty is a result of the components of the φ_2 vector being equal in magnitude for each case, but swapped in position.

2.4.2 Benefits of Tunable Coupling

The previous investigation reveals a huge advantage of practical systems with a tunable coupling stiffness, such as a MEMS system which uses electrostatic coupling, when compared to a fixed coupling system, such as microcantilever systems which are coupled through a substrate overhang. The key takeaway is that the maximum sensitivity of the system can always be achieved by adjusting the coupling magnitude to the smallest value that ensures all perturbations stay within the veering zone. For environments which induce small perturbations, a small potential is applied across the gap between the resonators. For larger perturbations the veering zone can be widened by increasing the potential across the gap while maintaining the condition that the coupling magnitude does not exceed half of the grounding stiffness magnitude.

Chapter 3: Experimental System

3.1 Introduction to the Experimental System

The experimental system was designed to build off the previous success of other researchers (for example using electrostatic coupling [18]) while introducing several novel concepts. First, the resonators in this design are suspended plates driven by electrostatic comb actuators. This is the first time this type of resonator has been used in a veering system. Second, the method of inducing a stiffness perturbation by directly affecting the suspensions is original. The system was designed using proprietary MEMS design software (CoventorWare) and fabricated in one of the most mature micromachining processes available (SOIMUMPs).

3.2 Design of System

Given the nature of micro device fabrication, one full production iteration; consisting of design, simulation, fabrication, and testing, could be achieved over the course of the project. Since this is the first device of this type at this university, advice on how to guide future endeavours based on experience gained in this iteration will be discussed in Chapter 6. This section will first explore the design tools and fabrication technology used, and then it describes the experimental systems themselves.

3.2.1 Design Tools - CoventorWare

The MEMS structures were designed and simulated using CoventorWare 2010. CoventorWare can perform three major parts of the design process for micro devices: system-level modeling (Architect), mask design and layouts (Designer) and numerical analysis (Analyzer).

The first step in the design process was to use the Process Editor to define the number of layers, the layer thicknesses, and the materials used in the fabrication process. Some standard fabrication processes are predefined, including SOIMUMPS (see Section 3.2.2). The only change the user must make to the predefined SOIMUMPS process flow is adjusting the device layer thickness to the 25 μm ± 1 μm wafer instead of the default 10 μm wafer.

Then, using SaberSketch, system-level macro models of the devices were built from the provided parametric libraries of components (see Figure 3.2). These libraries contain reduced-order models of common structures like plates and beams and can also model electrostatic interactions. Using built-in signal sources (voltage, current, force or other domains) the responses of the macro models can be simulated for DC operating point, AC analysis, transient analysis and others. It also provides the flexibility for looped simulations which sweep variables that can be signals or physical dimensions of the structures themselves for analysis of the sensitivity of the structures to fabrication tolerances. The advantage of using these macro models is greatly reduced simulation time when compared to more intensive numerical simulations with reportedly comparable results [22]. Architect also allows 3D visualizations of simulation results using Scene3D (refer to Figure 3.1). This is a particularly useful visual tool when analyzing the mode shapes of coupled resonators.

The macro models can then be automatically converted into layouts in standard formats like GDS and CIF by Coventor's Designer [23]. Designer is also used to

create 3D models that can be meshed and analyzed using Coventor's Analyzer or other third-party FEA software [23].

More intensive numerical approaches to device analysis in CoventorWare are performed in the Analyzer. There are several approaches to numerical simulation depending on the type of analysis desired. For determining the system's mechanical behaviour, the MemMech solver (based on ABAQUS) uses a finite-element method (FEM) [24]. For electrostatic interactions, the MemElectro solver uses a boundary-element method (BEM) [24]. To combine these domains, CoSolveEM (static) and HarmonicEM (frequency domain) solvers are used for coupled electromechanical analysis [24].

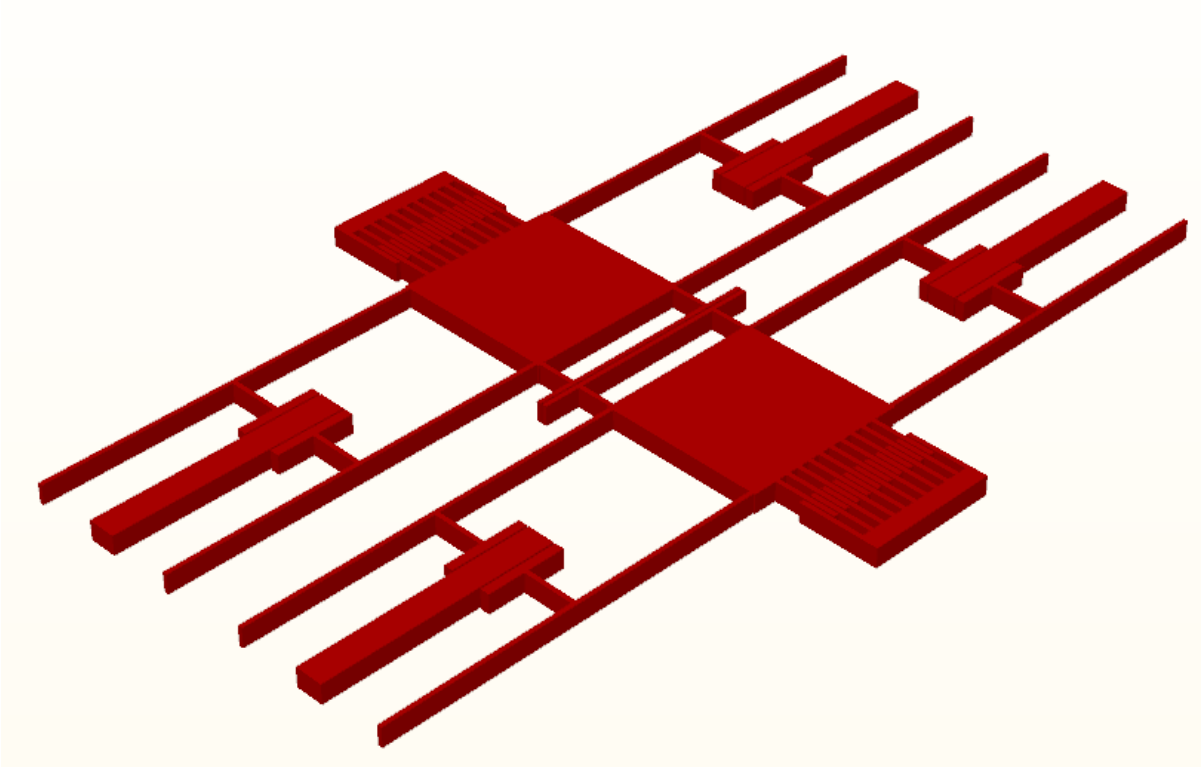

Figure 3.1: Visualization of the system schematic from Figure 3.2 in Scene3D

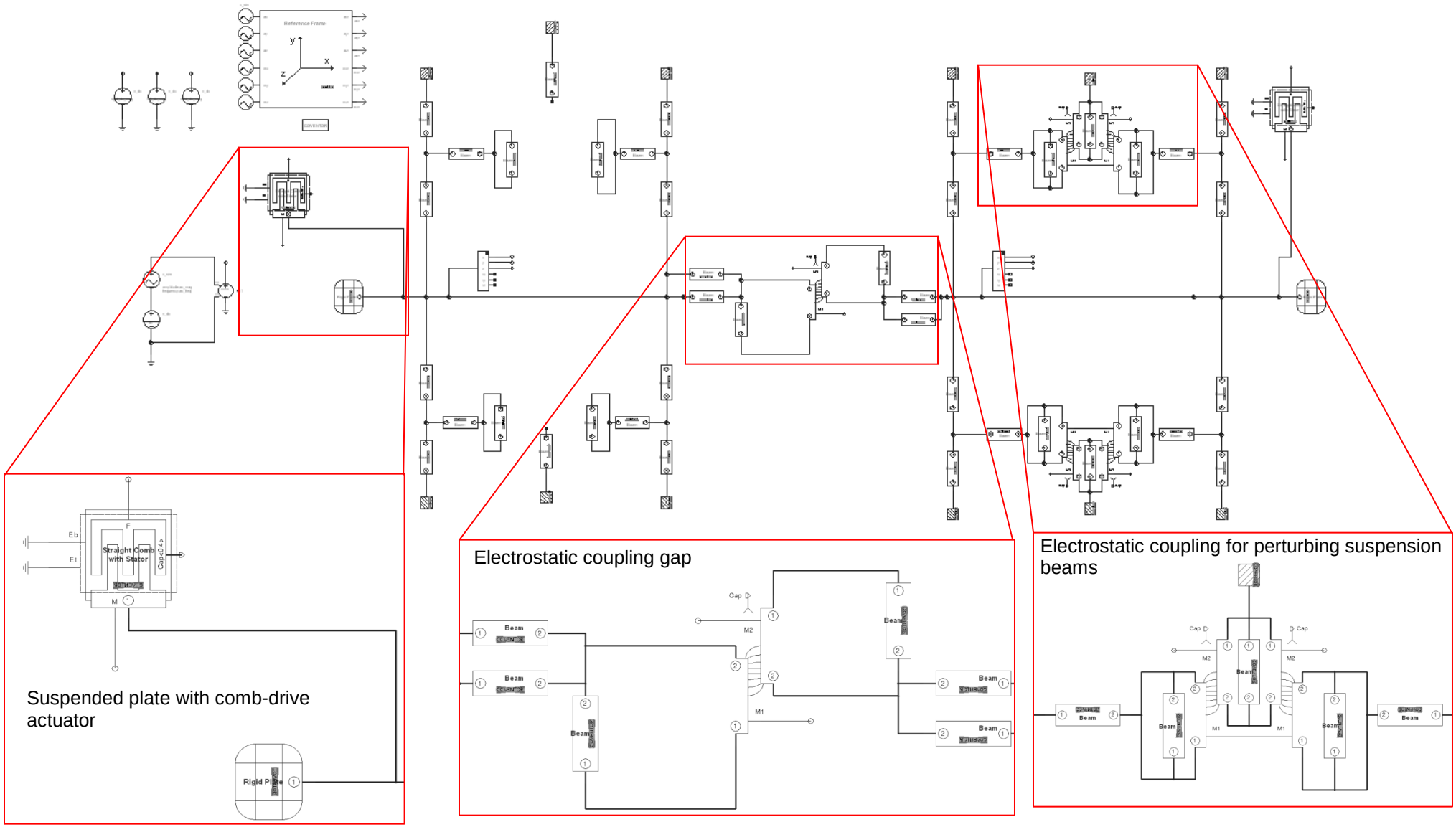

Figure 3.2: Schematic of a complete macromodel of a coupled resonator system made in Architect

The ability to use one software package for the entire design process is desired from a consistency and reliability standpoint. The capabilities of CoventorWare matched what was desired for development of the physical resonator structures and was therefore used extensively in the design phase of this project.

3.2.2 SOIMUMPs and Fabrication

SOIMUMPs is a mature, 4-mask, silicon-on-insulator (SOI) micromachining process offered by MEMSCAP [25]. The chosen SOI wafer has a silicon device layer thickness of 25 μm, an insulating oxide thickness of 1 μm and a substrate thickness of 400 μm [25]. The tolerances of each layer are ±1 μm, ±0.05 μm, and ±5 μm respectively [25]. This process was chosen for several reasons; it has been used with success in the past by other members of the research group, the relatively thick device layer is amenable to inertial sensors, and the process has been available since 2003 with 36 previous successful fabrication runs. This reliability was desired to maximize the likelihood of obtaining functional devices.

The general process flow begins with doping of the device layer by depositing phosphosilicate glass (PSG) and annealing [25]. Next, the pad metal (a lamination of 20 nm of chrome followed by 500 nm of gold) is patterned with a liftoff process [25]. This step is for making low resistivity routings and bond pads. The next step is to pattern the device layer silicon and then etch it to the insulating oxide layer in order to create the mechanical structures [25]. This is followed by a backside etch through the substrate in order to create through-holes which free the mechanical structures [25]. Another benefit to the backside etch is it dismisses the need for release holes in the mechanical structures. This yields two benefits. First larger inertial masses in

a given footprint, such as those desired in accelerometers and gyroscopes, can be fabricated. Second, a lack of release holes leads to large flat surfaces with high reflectivities which are well-suited to laser interferometry. The remaining oxide is removed and a final metal layer (this time 50 nm of chromium followed by 600 nm of gold) is patterned using a shadow mask and evaporation [25]. This layer can be used to create optical quality mirrored surfaces [25].

The masks were generated from the macromodels in CoventorWare and fine detailing of the layouts was finished with CleWin 4. The masks were submitted to CMC Microsystems in October 2011 and were subsequently forwarded to MEMSCAP for fabrication in the 37th SOIMUMPs run. Twelve chips were returned in 68 pin ceramic pin-grid array (CPGA) packages and three chips were returned unpackaged in February 2012.

3.2.3 Designs

All of the experimental structures share the same basic design; two suspended plate resonators that are excited by electrostatic comb drive actuators and are coupled electrostatically through a mutual capacitance formed along the adjacent sides of the plates. A perturbation is induced into the structure by slightly bending all of the suspension beams which support one of the two resonators. This perturbation is achieved in one of two ways: electrostatically or mechanically. Photos of each design can be seen in Figure 3.3 and Figure 3.4. For ease of discussion, the convention will be that the resonators on the left in these figures will be referred to as the “first resonator” and the resonator on the right will be referred to as the “second resonator”. All perturbation signals are applied to the second resonator.

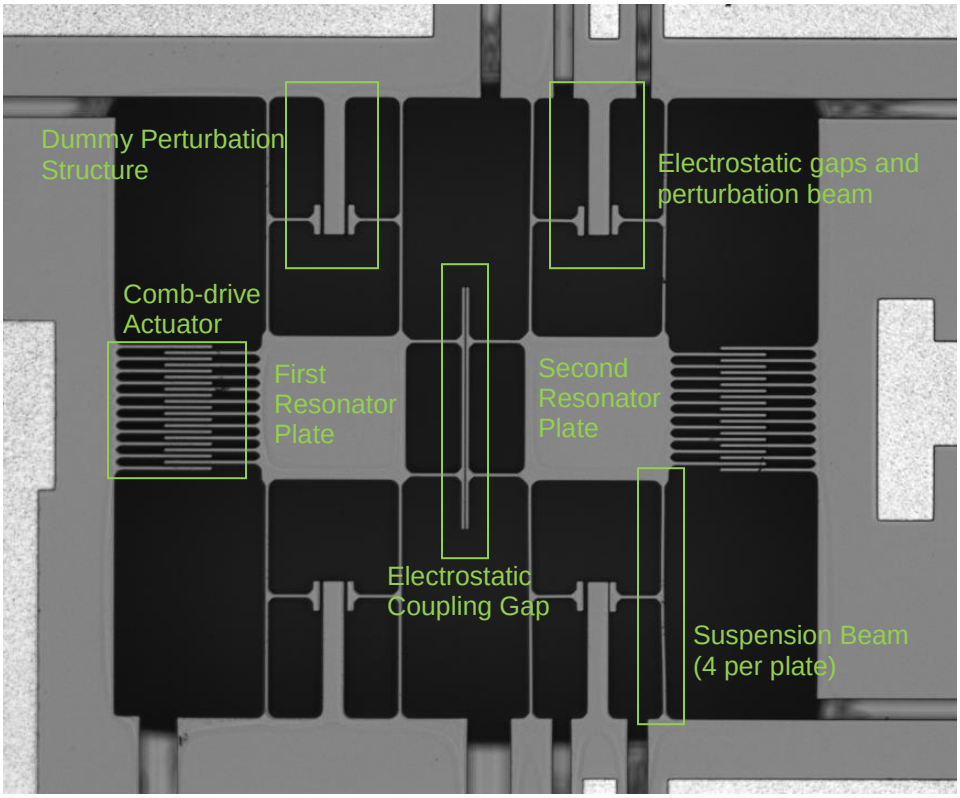

Figure 3.3: Photograph of experimental system which uses an electrostatic perturbation

Notice the “Dummy Perturbation Structure” in Figure 3.3. This exists only to maintain the physical symmetry between the two suspended masses. It can be seen that the dummy structure and the suspensions beams are electrically shorted for the first resonator but are electrically insulated on the second structure such that a voltage can be developed between the perturbation beam and the suspension beams. This voltage leads to an electrostatic attraction which will change the shape of the suspension beams. The perturbations to the suspension beams on the second resonator are also developed by the identical perturbation beam on the bottom of the second resonator to maintain symmetry in the suspensions (while simultaneously breaking symmetry between the first and second resonator).

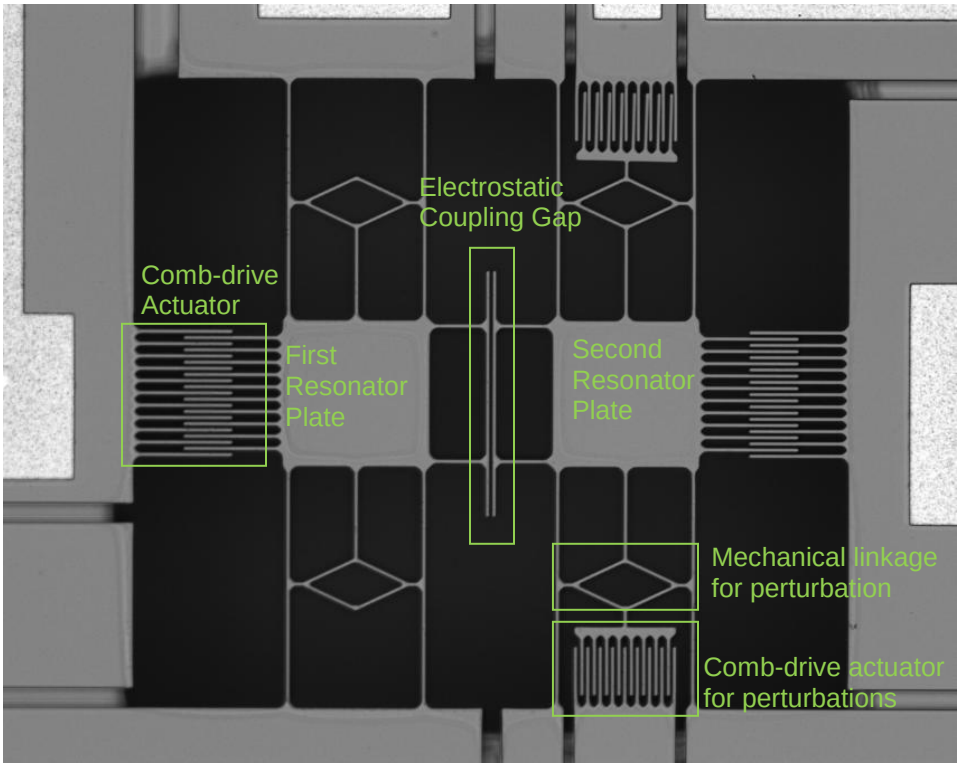

Figure 3.4: Photograph of experimental system which uses a mechanical perturbation

For the mechanically perturbed system, the force is still generated by electrostatic attraction in the “Comb-drive actuator for perturbations”, but this force is then mechanically linked to the suspension beams through the parallelogram structures. These structures also serve to translate a force in the y-direction into a force on the suspension beams in the x-direction. The perturbations to the suspension beams on the second resonator are also developed by the identical comb-drive and parallelogram linkage at the top of the second resonator. The first resonator includes the parallelogram linkage to maintain symmetry but omits the comb-drive actuators.

In addition to two different methods of perturbing each system, two sizes of each system were also designed. For the small systems, the minimum feature size of 3 μm is used for the beam widths and the minimum gap size of 2 μm is used for all electrostatic coupling. The plates are 110 μm squares and the suspension beams

are 200 μm long. The large size uses 6 μm for the beam widths but maintains the 2 μm gap size. These plates are 210 μm squares and the suspension beams are 500 μm long. All design parameters can be found in Appendix B.

For the structures with electrostatic perturbation, a structure that forms a mutual capacitance with the suspension beams at their midpoint is the source of a small force when a voltage is developed between the structure and the suspension beams. The result is to slightly bend the suspension beams inward. Ordinarily a straight fixed-guided beam with a load applied at the guided end has an effective spring constant defined by $k = \frac{Etw^3}{L^3}$ where E is Young's modulus of the material, L is the length of the beam, w is the width of the beam and t is the thickness. The perturbation changes the shape of the beam while also inducing an axial strain due to the symmetry of the structure (since there are beams on either side of the plate, the total length is fixed). However, additional effects that perturb symmetry will be discussed in Section 3.3.

3.3 System Perturbation

The key to creating a practical MEMS sensor based on eigenvalue veering is creating a scheme which will perturb the symmetry of the 2DOF system. Either a mass or stiffness perturbation is equally valid but the design approach depends on the quantity to be sensed. As has been shown repeatedly, selective coating on microcantilever resonators can be used for chemical detection [26]. Molecules of interest adsorb on the surface of the microcantilever and change its resonant frequency [26]. This same approach can be used in veering sensors by selectively coating one of the two resonators. The resulting adsorption will change the mass of

one of the two resonators, thereby breaking symmetry and leading to energy localization.

Other (i.e. nonchemical) quantities of interest may include inertial quantities such as acceleration. In order to sense acceleration using veering, the acceleration needs to affect either the stiffness or the mass of one of the sensors. One approach could be to couple an inertial mass to the suspensions of one resonator such that an external acceleration would cause a strain on the suspensions. The strain would break symmetry in the system by affecting the stiffness parameter. This approach was used successfully for charge sensing in [20] and the principle of operation of this sensor was described in the introduction to this thesis. While typically beams are extremely stiff when regarded as springs in the axial direction, the sensor in [20] proves that veering sensors can be used to detect these incredibly small quantities.

The systems designed for this thesis also use a controllable stiffness perturbation rather than a mass perturbation. In this case, electrostatic comb-driven plates suspended by four straight beams are used as resonators. The stiffness perturbation is induced by applying a transverse force to the center of each suspension beam on one of the resonators. The hypothesis is that bending the beams in such a way will lead to increased beam stiffness and therefore a breaking of symmetry.

3.3.1 Description of the Beam Shape

It can be useful to have a mathematical description of the shape of the beam when it is bent by an applied force. This can be found as a function of two variables: the length of the beam $\mathcal{L}'$ and the maximum out-of-line displacement at the center of the

beam 'α'. These variables in relation to the suspended plate can be seen in Figure 3.5 below.

A polynomial '$f(x,\alpha)$' can be found which describes the beam shape as a function of position along the beam 'x' and of the variable 'α' subject to some initial conditions. The conditions are summarized in the following table.

Table 3.1: Summary of the boundary conditions needed to solve a mathematical description of the perturbed beam's shape.

Boundary Condition	Description
$0 \leq x \leq L$	n/a
$f(0,\alpha) = 0$	Beam displacement at origin is zero
$f(L,\alpha) = 0$	Beam displacement at terminal zero
$f(L/2,\alpha) = \alpha$	Beam displacement in the center is α
$f'(0,\alpha) = 0$	Beam rotation at origin is zero
$f'(L,\alpha) = 0$	Beam rotation at terminal is zero

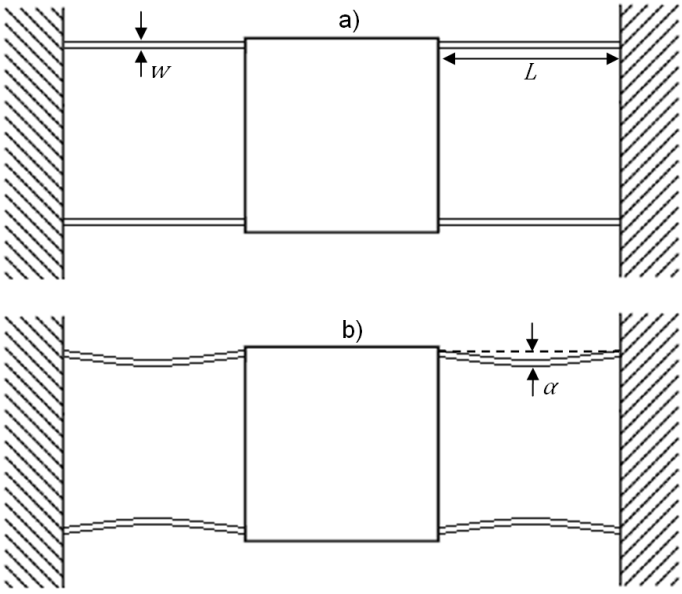

Figure 3.5: a) Plate suspended by four straight, cantilevered beams, b) Plate suspended by four cantilevered beams with a curved profile due to some external force

The lowest order polynomial which can satisfy all of the boundary conditions is fourth order:

$$f(x,\alpha) = a_0 + a_1 x + a_2 x^2 + a_3 x^3 + a_4 x^4 \tag{3.1}$$

The first two coefficients are found immediately:

$$f(0,\alpha) = 0 \rightarrow a_0 = 0 \tag{3.2}$$

$$f'(0,\alpha) = 0 \rightarrow a_1 = 0 \tag{3.3}$$

The remaining conditions are used to create a system of equations in order to solve for the remaining coefficients.

$$f(L,\alpha) = L^2(a_2 + a_3 L + a_4 L^2) = 0 \tag{3.4}$$

$$f'(L,\alpha) = L(2a_2 + 3a_3 L + 4a_4 L^2) = 0 \tag{3.5}$$

$$f\left(\frac{L}{2},\alpha\right) = \frac{a_2 L^2}{4} + \frac{a_3 L^3}{8} + \frac{a_4 L^4}{16} = \alpha \tag{3.6}$$

$$\begin{bmatrix} 1 & L & L^2 \\ 2 & 3L & 4L^2 \\ \frac{L^2}{4} & \frac{L^3}{8} & \frac{L^4}{16} \end{bmatrix} \begin{bmatrix} a_2 \\ a_3 \\ a_4 \end{bmatrix} = \begin{bmatrix} 0 \\ 0 \\ \alpha \end{bmatrix} \tag{3.7}$$

Solving the system the final polynomial is found.

$$f(x,\alpha) = \frac{16\alpha}{L^2}x^2 - \frac{32\alpha}{L^3}x^3 + \frac{16\alpha}{L^4}x^4 \tag{3.8}$$

3.3.2 Finding 'α' for the Mathematical Description of Beam Shape

Further to determining a mathematical description of the beam shape, the value of α for a given force can be found. Under static conditions, assuming no deformation of the suspended plate, each beam can be considered fixed-fixed since neither end can rotate or translate. The deflection of the center of such a beam given a point-load at the center is well-known and is given by [27]:

$$\alpha = \frac{FL^3}{192EI} \tag{3.9}$$

Where E is Young's Modulus for the device layer (169 GPa for silicon in the SOIMUMPs process) and I is the area moment of inertia, which for a beam with a rectangular cross-section is given by:

$$I = \frac{hw^3}{12} \tag{3.10}$$

If the force and dimensions of the beams are known, then it is trivial to determine the deflection of the center of the beam, and therefore the deflection at any point along the beam can be found.

3.3.3 Electrostatic Spring Softening

Originally it was hypothesized that pre-bending the beams in this way before excitation would lead to an axial-strain and a resulting increase in stiffness. However, simulation of each design and testing data from the electrostatic design contests this supposition. Instead, increasing the voltage between the second resonator and the perturbation driver (a gap-closing driver in the electrostatic case and a comb-drive in the mechanical case) acts to decrease the stiffness and therefore decrease the resonant frequency. Figure 3.6 presents the shift in the in-phase resonant frequency as simulated in CoventorWare and Figure 3.7 depicts the same except for the anti-phase resonant frequency. The resonant frequencies show a quadratic dependence on perturbation voltage, with the fit passing within the margin of error based on the resolution of the simulations (±1.75 Hz). It may also be noticed that the in-phase resonant frequency is higher than the anti-phase resonant frequency due to the negative coupling.

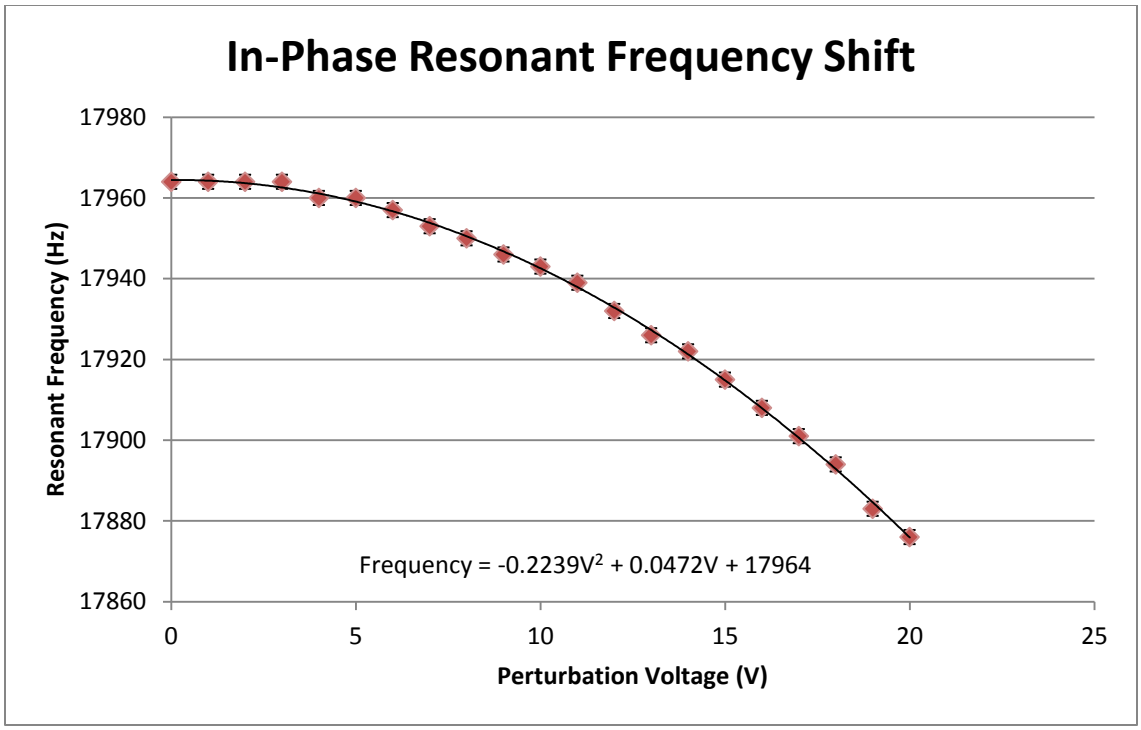

Figure 3.6: Simulated shift in in-phase resonant frequency for the large electrostatically perturbed system including quadratic fit to the results.

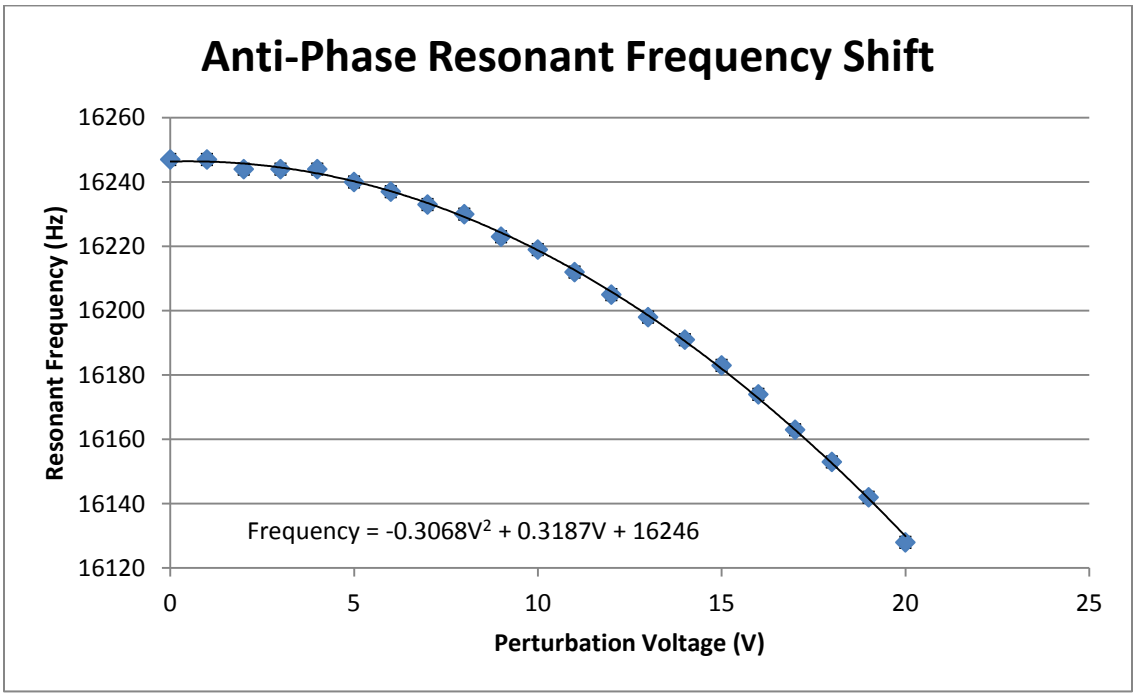

Figure 3.7: Simulated shift in anti-phase resonant frequency for the large electrostatically perturbed system including quadratic fit to the results.

The explanation is electrostatic spring softening, an effect that crops up often in microsystems. This nonlinear effect will be most easily illustrated in the electrostatic design. In the static case when no time-varying signal is applied to the system, there will be an electrostatic attraction between the perturbation beam and the suspension beam. This electrostatic force is balanced by the beam acting as a spring. If this situation is modeled as an example of a parallel-plate capacitor, the magnitude of the force of attraction is given by:

$$F = -\frac{1}{2}\frac{\varepsilon A V^2}{d^2} \tag{3.11}$$

Clearly the force is a nonlinear function of the gap distance 'd'. When a driving signal is applied to the resonators and they respond, the separation between the suspension beams and the perturbation beam changes, leading to a time-varying force. This is usually written as:

$$F = -\frac{1}{2}\frac{\varepsilon A V^2}{(d-x)^2} \tag{3.12}$$

where 'x' is a decrease in gap distance. Performing a Taylor expansion and keeping only the linear terms, the electrostatic force can be approximated as:

$$F \approx -\frac{1}{2}\frac{\varepsilon A V^2}{d^2}\left(1+\frac{2}{d}x\right) \tag{3.13}$$

Spring softening can now be examined by balancing all of the forces in an example system. Neglecting damping, the sum of the forces for the oscillatory system in Figure 3.8 is:

$$m\ddot{x} + kx - \frac{1}{2}\frac{\varepsilon A V^2}{d^2}\left(1+\frac{2}{d}x\right) = 0 \tag{3.14}$$

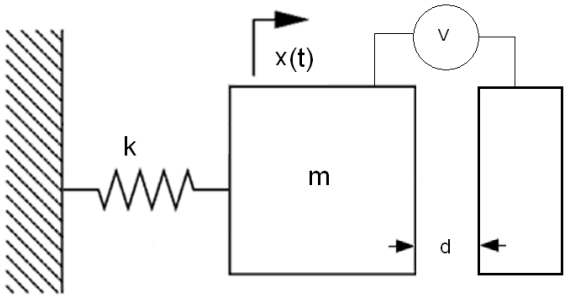

Figure 3.8: Spring-mass system which forms a parallel plate capacitor through its mutual area with another electrode when a potential difference 'V' is applied across the gap

With simple rearrangement:

$$m\ddot{x} + \left(k - \frac{\varepsilon A V^2}{d^3}\right)x - \frac{1}{2}\frac{\varepsilon A V^2}{d^2} = 0 \qquad (3.15)$$

Since ε, A, V, and d are all positive, the mechanical spring constant is reduced by a factor k_e where $k_e = -\frac{\varepsilon A V^2}{d^3}$.

Now the designed systems will be analyzed using the full expression for the electrostatic force (not the linearized version). Consider the actual electrostatic resonator design in Figure 3.9. Here the balance of the forces is:

$$m_2\ddot{x_2} + k_{tot}x_2 - \frac{\varepsilon A V^2}{(d - x_2')^2} + \frac{\varepsilon A V^2}{(d + x_2')^2} = 0 \qquad (3.16)$$

In this equation, k_{tot} is taken to be the entire mechanical contribution of the suspension beams to the spring constant. This includes both the inherent spring behaviour of a straight beam, and any increase in stiffness due to stresses induced by the force from electrostatic attraction. The third and fourth terms account for the four electrostatic coupling gaps, one on each side of each of the perturbation beams. Multiplying these terms by $\frac{x_2}{x_2}$ yields:

$$m_2\ddot{x_2} + (k_{tot} - \frac{\varepsilon AV^2}{x_2(d - x_2')^2} - \frac{\varepsilon AV^2}{x_2(d + x_2')^2})x_2 = 0 \quad (3.17)$$

Therefore:

$$k_e = -\frac{1}{x_2}\left(\frac{\varepsilon AV^2}{(d - x_2')^2} - \frac{\varepsilon AV^2}{(d + x_2')^2}\right) \quad (3.18)$$

$$k_e \approx -\frac{4\varepsilon AV^2}{d^3 x_2} x_2' \quad (3.19)$$

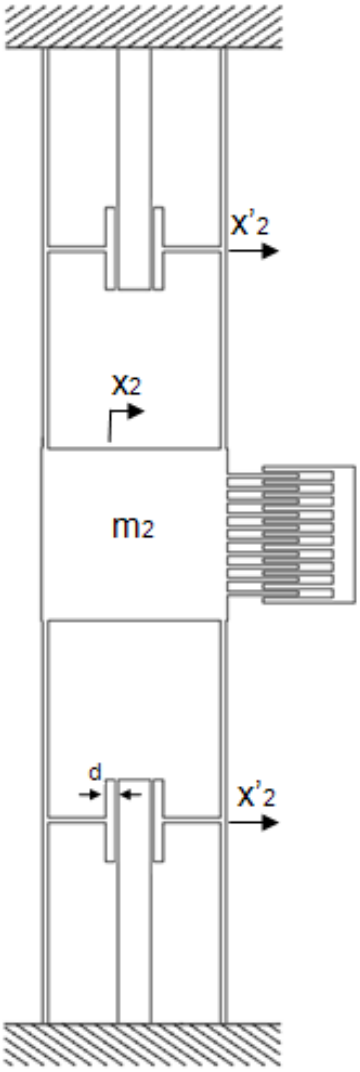

Figure 3.9: Perturbing the second resonator. A potential difference is developed between the thick beams at the top and bottom and the suspension beams, halfway down their length

Clearly k_e will always be negative since the signs of x_2 and x_2' are always the same. Additionally, as a result of simulation and data from the electrostatic design, k_e seems to overpower the increase in stiffness from the pre-bending of the beams as seen in Figure 3.10.

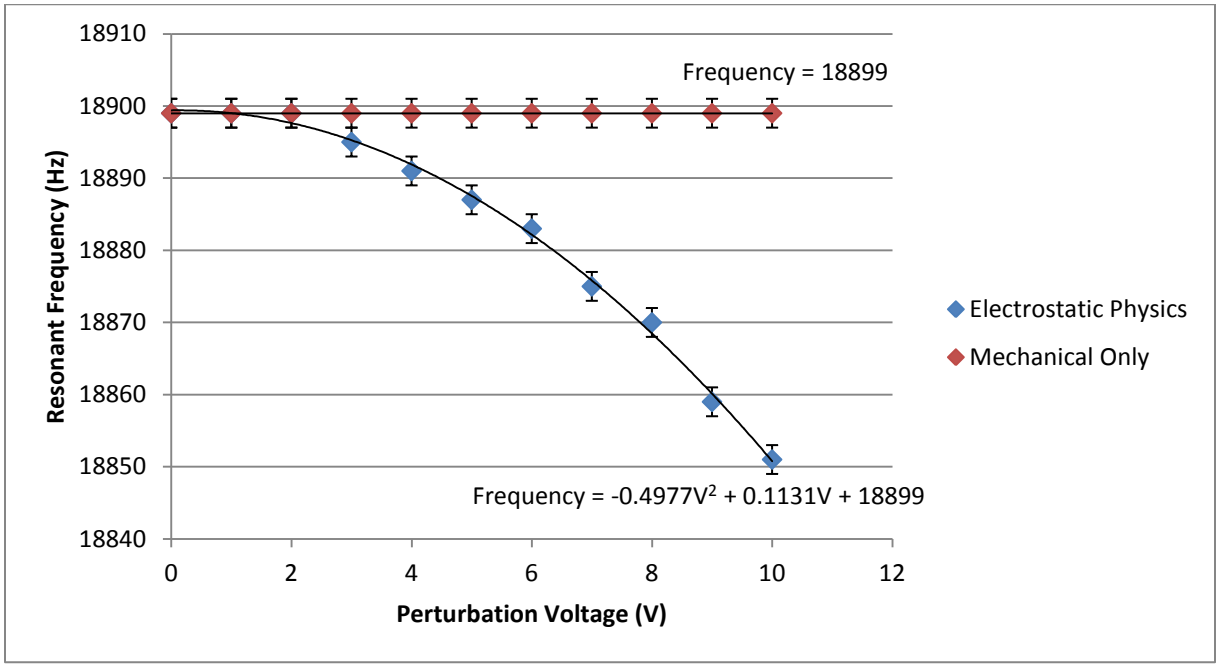

Figure 3.10: Resonant frequency shift simulation including electrostatic physics or for a pure mechanical force

Figure 3.10 was obtained by simulating just one of the resonators from the electrostatic system in CoventorWare. Including the electrostatic physics, the resonant frequency decreased quadratically with increasing potential. The resonator was simulated again but removing the electrostatic physics and applying a pure mechanical force to the beams of the same magnitude as generated in the electrostatic gap. At this resolution, the mechanical force failed to affect the resonant frequency at all. In order to prove the hypothesis that a pure mechanical force should lead to an increased resonant frequency by pre-stressing the suspensions,

the simulations were rerun but using force magnitudes 100 times greater than are generated in the electrostatic gap. The results of this simulation are seen in Figure 3.11.

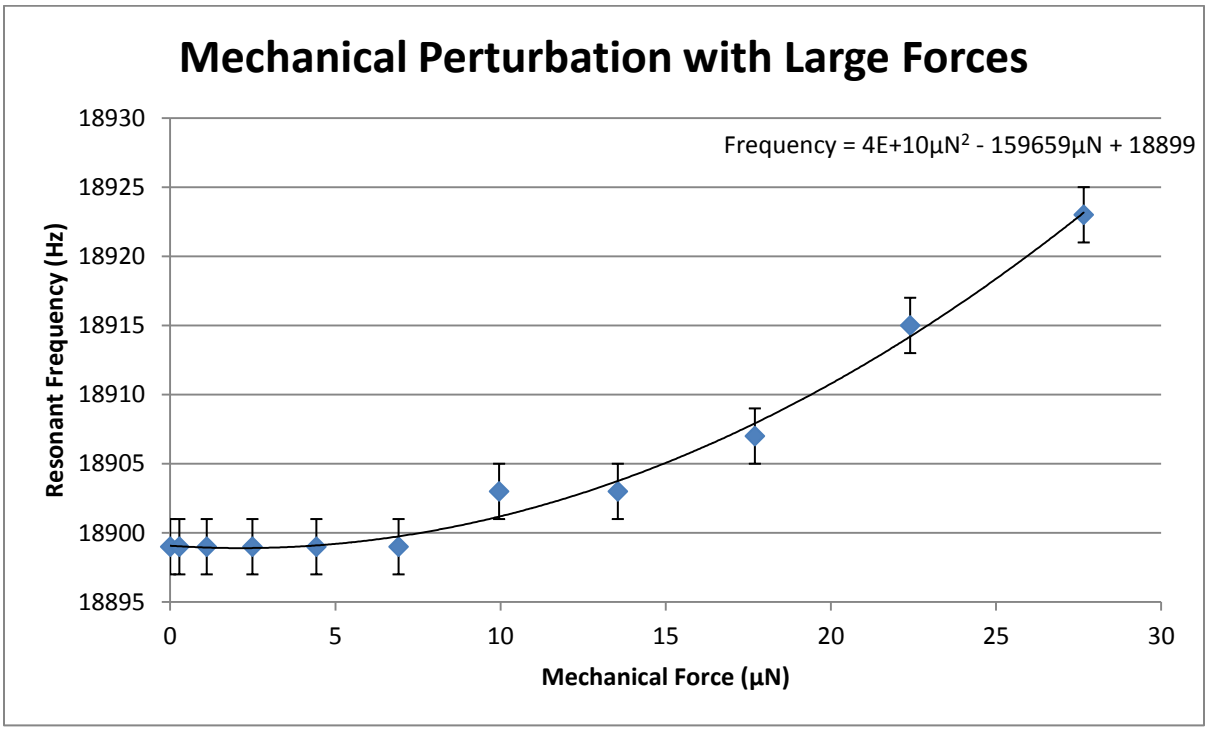

Figure 3.11: Resonant frequency shifts with a pure mechanical force as opposed to one that includes electrostatic interactions

This effect is actually the same as that used for the coupling of the resonators in the system. The negative nature of k_e is the negative coupling formed by the mutual capacitance between the two plates. Regardless of the method of perturbation, the salient fact is that a perturbation is induced, and it is measurable as will be demonstrated later in this chapter.

3.3.4 Perturbation in the Mechanical Design

The second design which was intended to induce a perturbation by physically linking the center of the beams to an electrostatic comb-drive also exhibited a lowered

resonant frequency and therefore reduced stiffness when simulated in CoventorWare. This result may be somewhat more surprising than with the electrostatic design but could still be explained by an electrostatic spring softening effect.

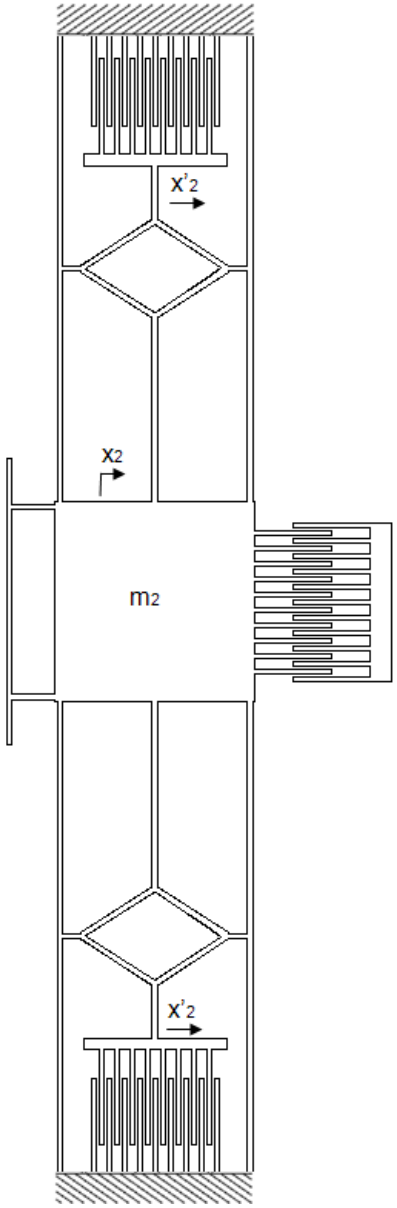

Figure 3.12: Mechanically perturbed design. In this design, a potential is developed between the anchored combs and those attached to the parallelograms at the top and bottom.

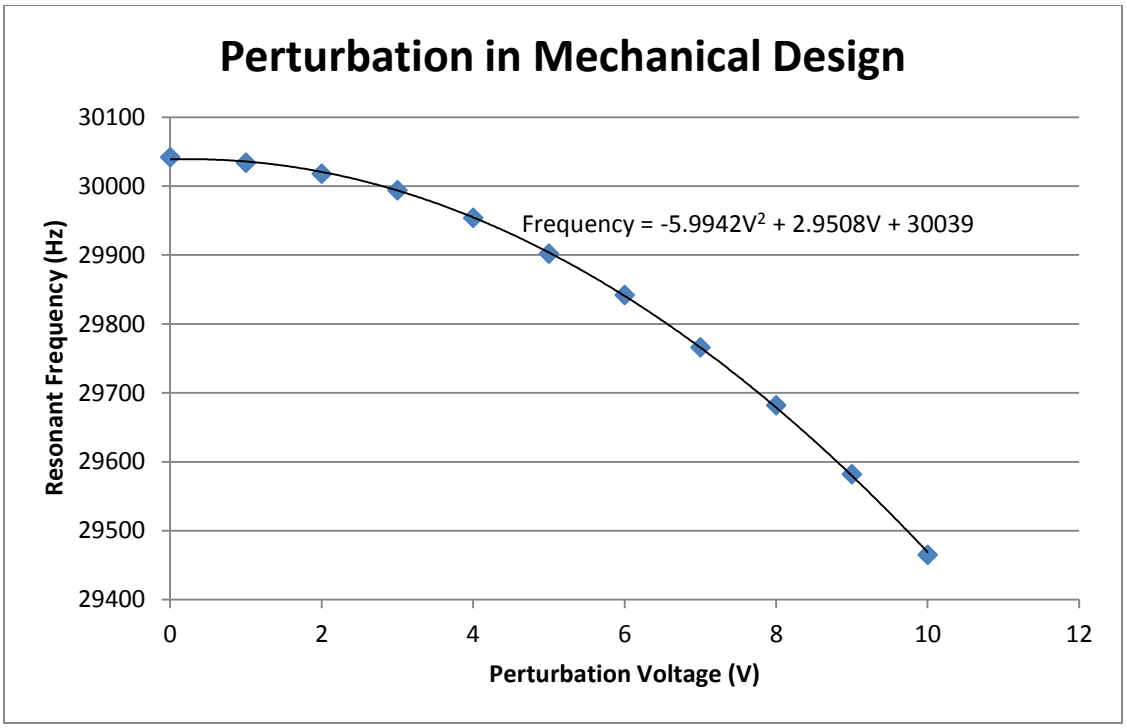

Figure 3.13: resonant frequency dependence on perturbation voltage for simulated system including electrostatic physics

Figure 3.12 shows the movable fingers linked to the suspension beams through a parallelogram structure. This structure translates the vertical displacement of the combs into a horizontal displacement of the center of the suspension beams. Again, it was hypothesized that this pre-bending of the suspension beams would dominate, and the stiffness of the equivalent spring for the second mass would increase. However, since the resonant frequency decreases, there must be another effect in play. One solution is that the comb drive not only acts as a linear actuator in the y-direction, it also acts as a gap-closing actuator since the movable fingers will experience a small displacement in the x-direction as the plate oscillates in the x-direction. This would lead to an almost identical balance of forces as for the

electrostatic actuator except the mutual area, A, is much larger in this case, being formed on either side of every comb.

Analysis of the mechanical system with a pure mechanical force also yielded an interesting result. When a pure force was applied to the parallelogram structure in the same direction as the comb-drive actuator (remember, comb-drive actuators are attractive only), the resonant frequency still decreased. When a pure mechanical force was applied in the opposite direction (toward the suspended plate from either side), the resonant frequency increased. This behaviour can be witnessed in Figure 3.14.

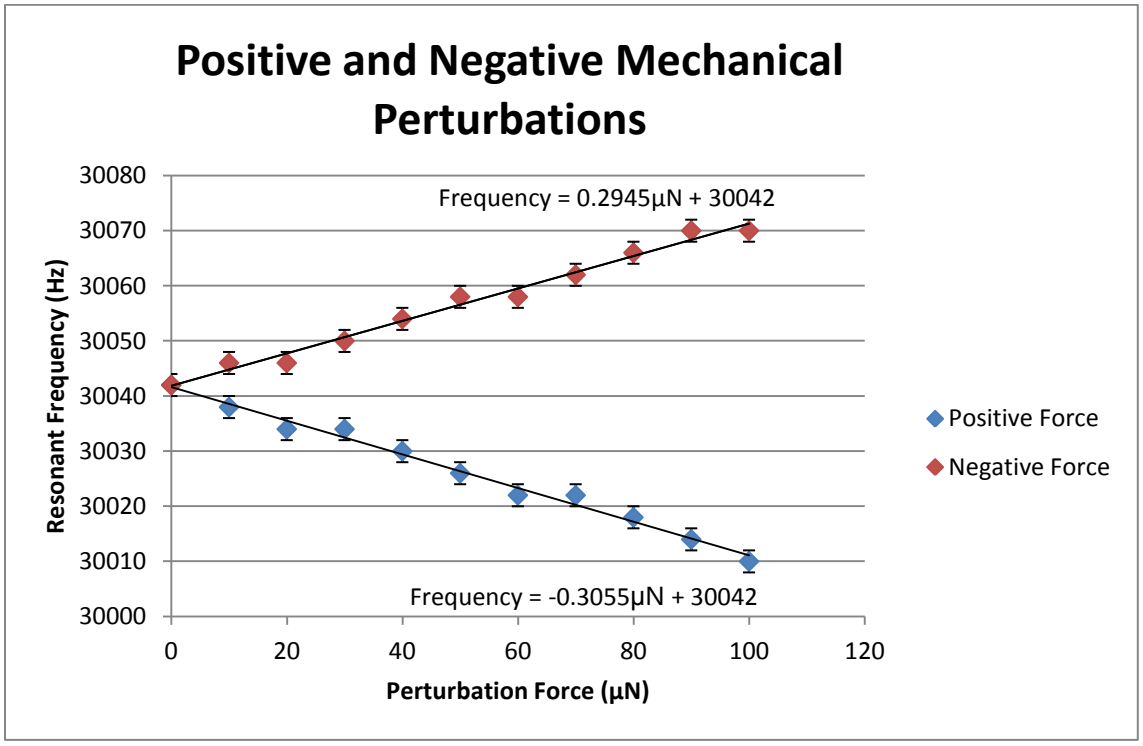

Figure 3.14: Pure mechanical perturbations on the mechanical system

Furthermore, the lowest order fit to the simulated data was linear. This behaviour is caused by the parallelogram structure itself. When stretched in the y-direction as with the comb-drive actuator or the positive mechanical force, the parallelogram

creates a softer effective spring in the direction of motion of the plate. When compressed in the y-direction, the parallelogram is stiffer due to a reduced effective length. It also seems that the parallelogram partially compensates for the quadratic dependence on force seen for the electrostatic system, allowing the dependence to be linear.

3.4 Testing

Experimentation on the fabricated chips took place at the University of British Columbia in the spring of 2012. The equipment was available until May 31, 2012, at which point the equipment was to be shipped to the manufacturer for hardware upgrades.

3.4.1 Testing Equipment

The fabricated chips were tested using a Polytec MSA-500 Micro System Analyzer with their Planar Motion Analyzer (PMA) software for non-contact, in-plane analysis of motion (see Figure 3.15). The MSA-500 consists of several components: the MSA Optical Unit, the MSA Processing Unit, and the MSA Software [28]. The optical unit has microscope optics with maximum magnification of 20 times. Integrated with the microscope optics are an LED for illumination and a progressive scan video camera [28]. The data from the video camera are fed to the processing unit, which consists of the junction box and the Data Management System; a computer running Windows XP with the proprietary Polytec software included [28]. The system is also capable of laser interferometry measurements for out-of-plane motion but this capability was unnecessary for these experiments [28]. The junction box contains a function generator and is where the driving signals for experimentation originate.

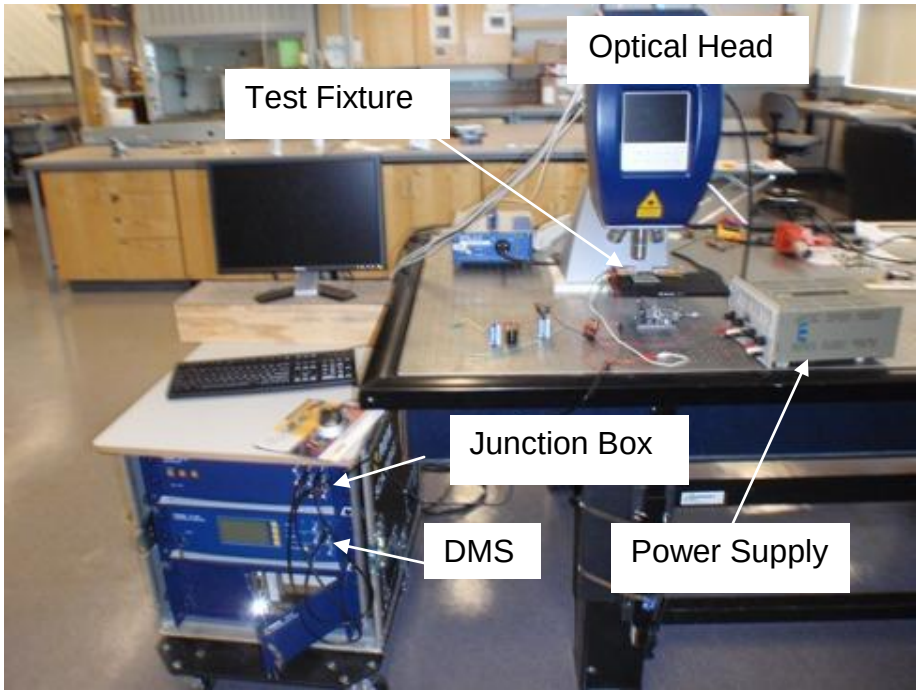

Figure 3.15: Testing setup. The junction box and DMS are in the cabinet on the left. The optical head, power supply, and test fixture are on the table.

The experiments also used a 20V power supply and 9V batteries. The batteries were used to bias the chips without the footprint expense of an additional power supply.

3.4.2 Video Stroboscopy

The MSA-500 system using the PMA software uses a video stroboscopy approach to in-plane motion measurements. The basic idea behind video stroboscopy is to excite the sample and then capture “frozen” images of its motion. By syncing the illumination (using an LED) with the excitation signal and processing the digital image by checking user-selected marker points, the motion of the sample can be determined. Figure 3.16 shows a close-up view of the test fixture under the optical head.

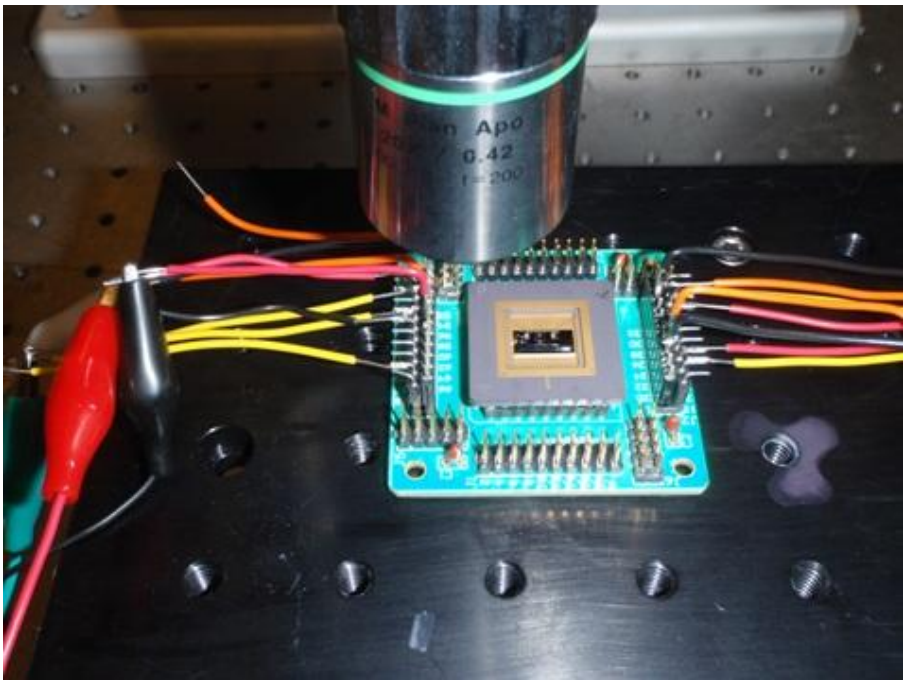

Figure 3.16: Close-up of 68-pin package in test fixture and optics.

In Figure 3.17 the user-selected zones can be seen from an actual test on one of the systems. It is possible to analyze up to two parts of the frame simultaneously, so the motion of both the left and right masses could be captured in each test. In the figure, the red boxes represent the stationary point set before the excitation signal is applied. The yellow boxes are the current position of that part of the microstructure and the green boxes simply enclose and mark the positions where measurements are taking place. In this case, both the ‘A’ and ‘B’ reference points have moved left and up relative to their initial positions. It is important that prior to applying the excitation signal that the user checks to ensure that the red box is completely covered by the yellow box. The user must also select a portion of the frame to measure which has discernible borders which enable the image to be processed.

For example, in Figure 3.17, the ‘B’ marker is a box which encloses the corner of the

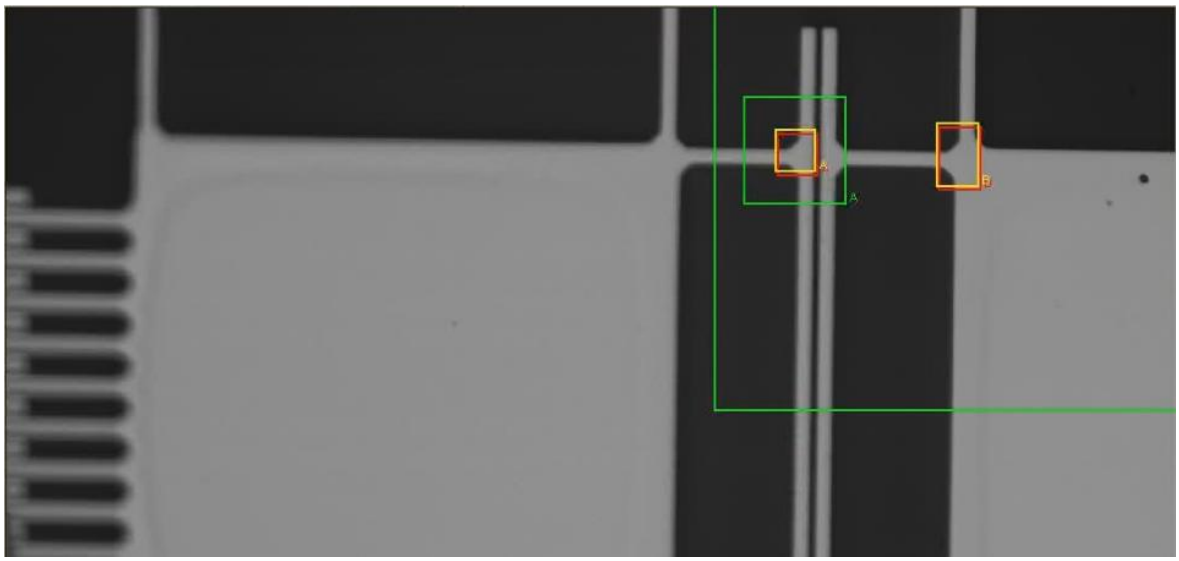

Figure 3.17: Screen capture from a PMA experiment. The left measurement area is marked 'A' and the right measurement area is marked 'B'.

suspended mass. This selection exhibits a border between light gray (the mass) and black (empty space) in both the x and y directions allowing the motion to be faithfully captured in both axes.

3.4.3 Experimental Setup and Procedure

Figure 3.18 provides a schematic of the experimental setup. Four 9V batteries in series with the sinusoidal signal (10 Vp-p) from the Polytec system provided the excitation to the combs on the first resonator. This resonator is also treated as the common ground in the setup. The batteries were tapped at the center and connected to the second resonator such that an 18 V potential was developed across the coupling gap between the two resonators. The perturbation signal was achieved by routing this 18 V line through a variable DC power supply and then to each of the perturbation beams on the chip (only one connection is depicted in

Figure 3.18). The combs of the second resonator were left floating so that the system is actuated single-endedly.

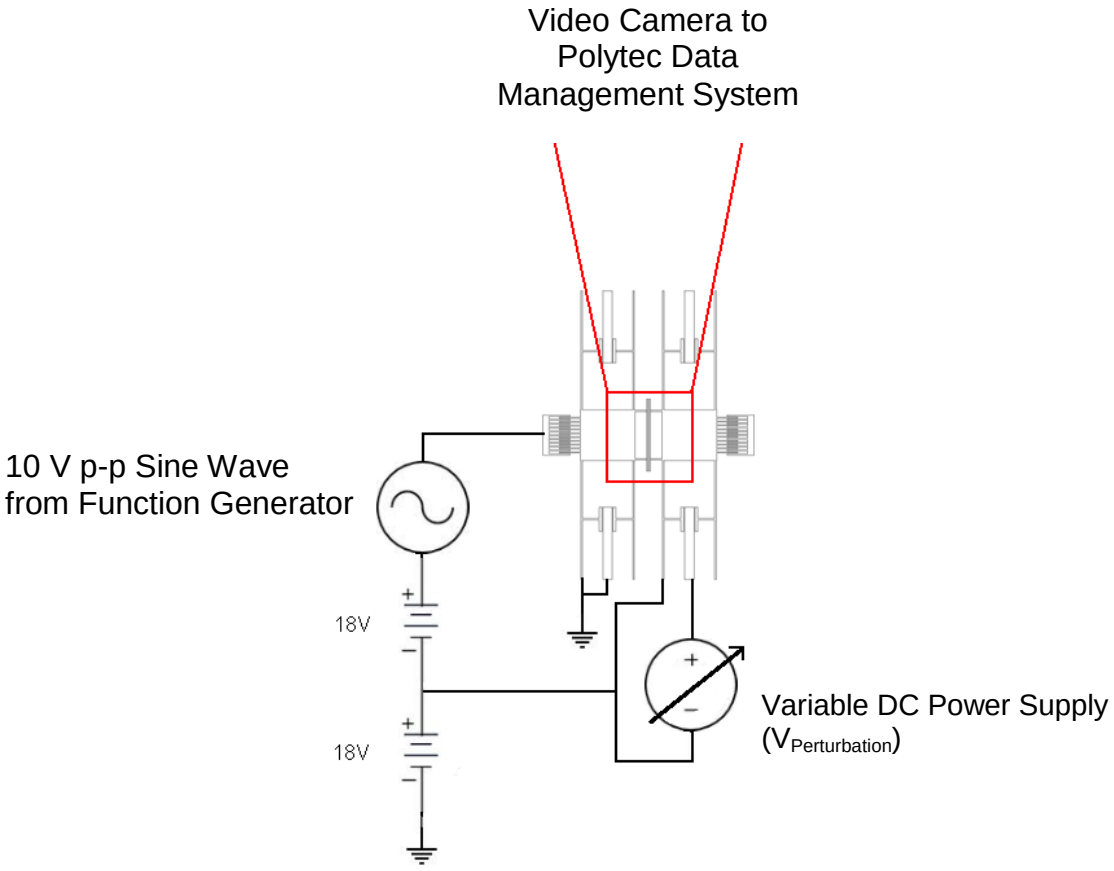

Figure 3.18: Schematic of the experimental setup

The driving signal generated in the PMA software steps up through a defined frequency range in discrete steps indicated by the user. For the experiments on the large electrostatic design, the frequency range was 16.8 kHz to 17.6 kHz in steps of 10 Hz. This isolates the resonant peak associated with the in-phase mode of vibration. This mode was selected since damping is higher for the out-of-phase mode due to the squeezing of air between the two plates of the coupling gap. Eight shots were taken by the camera per excitation signal after a settling period of 500 ms.

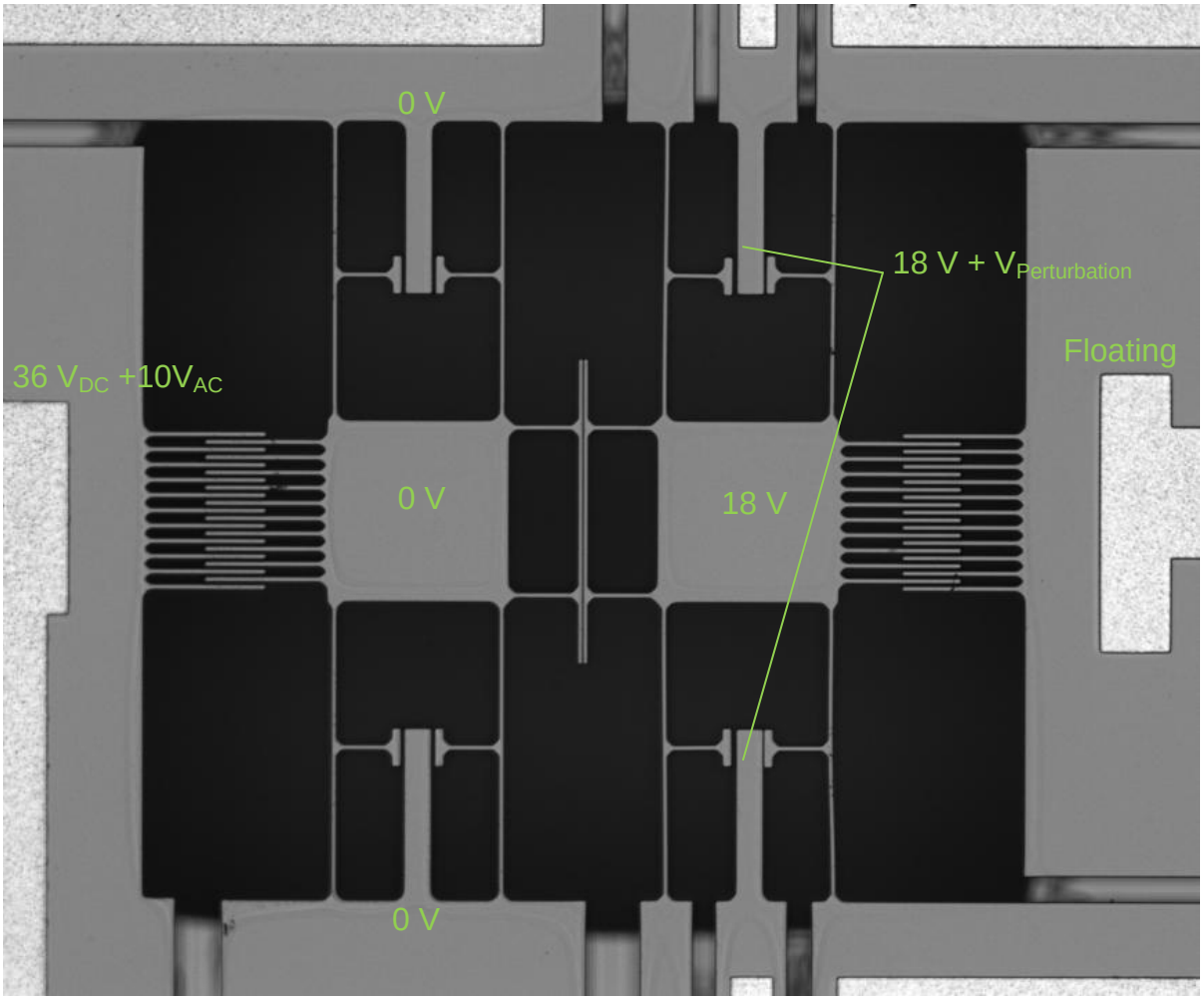

Figure 3.19: Voltages on the chip during testing

To generate one complete data set, the wired connections were made as directed in Figure 3.18. The variable source was set to 0V (i.e. $V_{Perturbation}$ = 0 V). This means that there is no potential across the gap on the suspension beams on the second resonator and therefore no perturbation. Two measurement zones ‘A’ and ‘B’ are selected on-screen, similar to Figure 3.17. Then the excitation signal is turned on and the system takes over. The system generates a 16.8 kHz sine wave and waits 500 ms for the system transients to settle. The LED then illuminates the sample eight times, synchronized with the driving signal. These 8 frozen images are sent to

the Data Management System for later processing. Then, the excitation signal is automatically stepped up by 10 Hz and the process repeats. Once the measurements for 17.6 kHz have been made, the excitation signal turns off and the data is processed using digital image processing techniques to determine the amplitudes of motion in both x and y directions for each measurement area (‘A’ and ‘B’) and for each frequency (16.8 kHz – 17.6 kHz with 10 Hz resolution).

At this point, the user increases the voltage of the variable supply by 1 V (inducing a perturbation) and repeats the process. Perturbations up to 20 V with 2.5 V or smaller resolution were performed. An additional set of data for the large electrostatic system was obtained but instead of an 18 V potential across the coupling gap, a 23 V potential was used. The perturbation beams were also fed a signal of 23 V + $V_{Perturbation}$. With a higher coupling potential, the coupling stiffness magnitude is higher and the eigenvectors should exhibit a reduced sensitivity to perturbation while the eigenvalue sensitivity should remain unchanged.

3.5 Results

Three measurement sets were prepared during testing from the large electrostatically perturbed system on two different chips; one for an 18 V coupling potential on chip one, and one each for an 18 V and 23 V coupling potential on chip two. The data points for the magnitude data were fitted in Mathematica assuming a second-order system since measurement points were clustered around only one of the resonant peaks. The fit function was of the following form:

$$H_{mag} = \frac{H_{dc}}{\sqrt{\left(\left(1 - \left(\frac{f}{f_0}\right)^2\right)^2\right) + \frac{1}{Q^2}\left(\frac{f}{f_0}\right)^2}} \tag{3.20}$$

This fitting process yielded an estimation of the resonant frequency of each mass (f_0), DC displacement of each mass (H_{dc}), and quality factor (Q) of each resonator for each of the perturbations. In general, the standard errors in the fitted data were more than an order of magnitude smaller than the estimated values. This fact coupled with visual confirmation when the fit is plotted with the measurement points provides a good degree of confidence in the quality of the fitting procedure. The quality factors in general were on the order of 100 which supports the claim in Chapter 2 concerning damping in MEMS. An example fit for one set of data is shown in Figure 3.20.

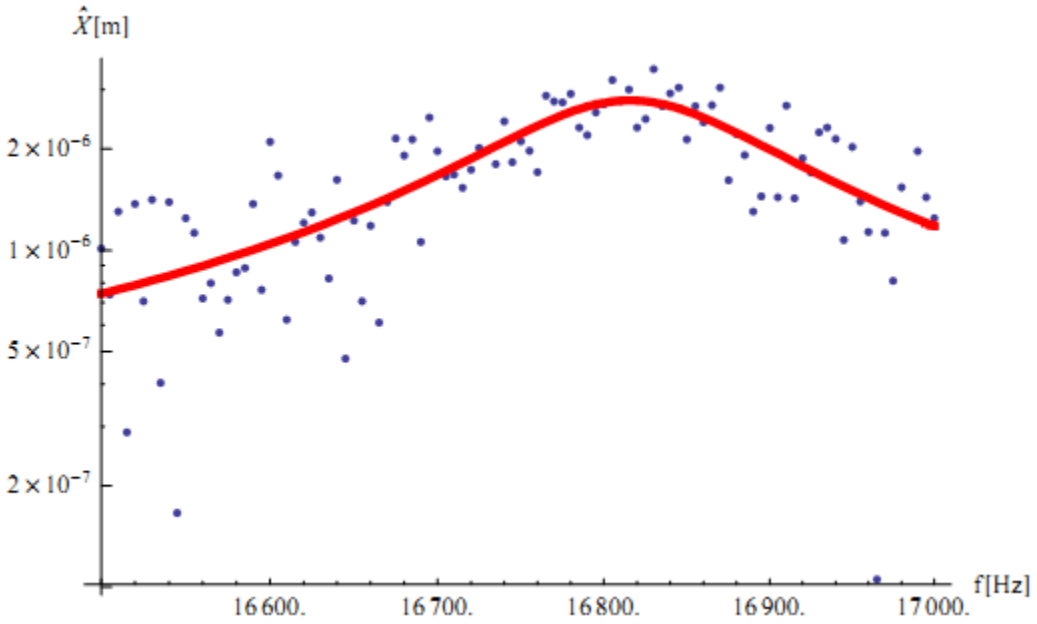

Figure 3.20: Example of fitting the data with a second order transfer function in Mathematica

3.5.1 Chip 1 with 18 V Coupling: Resonant Frequency Shifts

The first interesting aspect of Figure 3.21 is that the estimates of the resonant frequency for each of the masses are not the same. This suggests some asymmetry in the system that is likely a result from the asymmetrical excitation. The inability of the excitation signal to excite a single resonant mode leads to a superposition of each mode for each mass. Even if the weighting of the in-phase mode is much higher than the anti-phase mode, the weightings are not necessarily the same for each mass and this can lead to the difference. However, it is validating that the general response of the resonant frequency of either mass to a perturbation voltage is a decrease in frequency that is roughly second order. This matches the expectations from the simulation results earlier in this chapter.

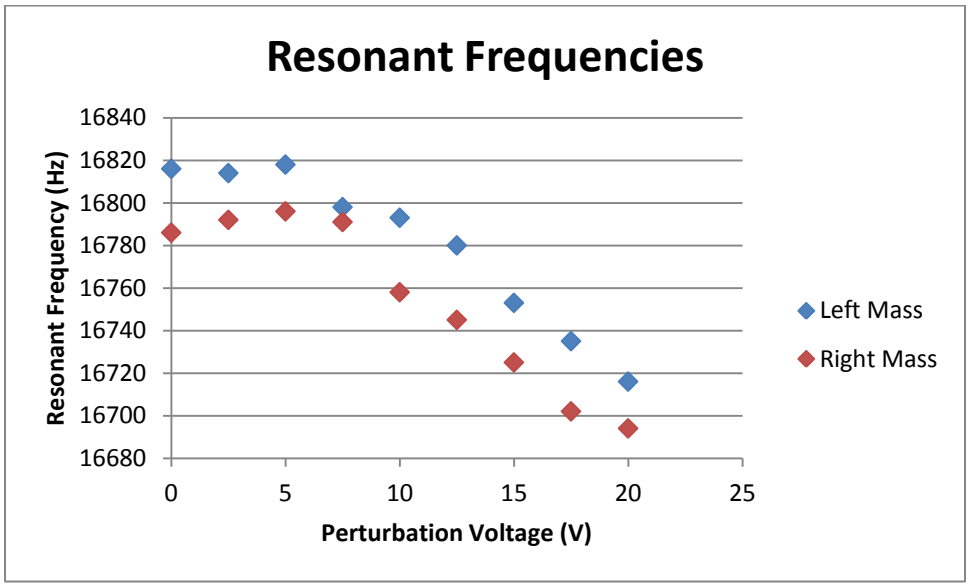

Figure 3.21: Resonant frequency dependence on perturbation voltage for the fits on each of the left and right masses

Another interesting behaviour exhibited in Figure 3.21 is that the difference between the resonant frequencies is not constant and it is minimized for the measurement at

7.5 V. This suggests that the weightings for the superposition of modes are at least partially compensated at this voltage leading to the greatest degree of symmetry in the system. Later, 0 V and 7.5 V will each in turn be used as a reference point for relative shifts in the system. 0 V is used since this is the designed symmetry point and 7.5 V is used due to the reasoning above.

Using the measure of sensitivity introduced in Chapter 2, the following two plots (Figure 3.22 and Figure 3.23) illustrate the percentage shift of the resonant frequencies relative to two different resonant frequencies, the resonant frequency for 0 V and the resonant frequency for 7.5 V.

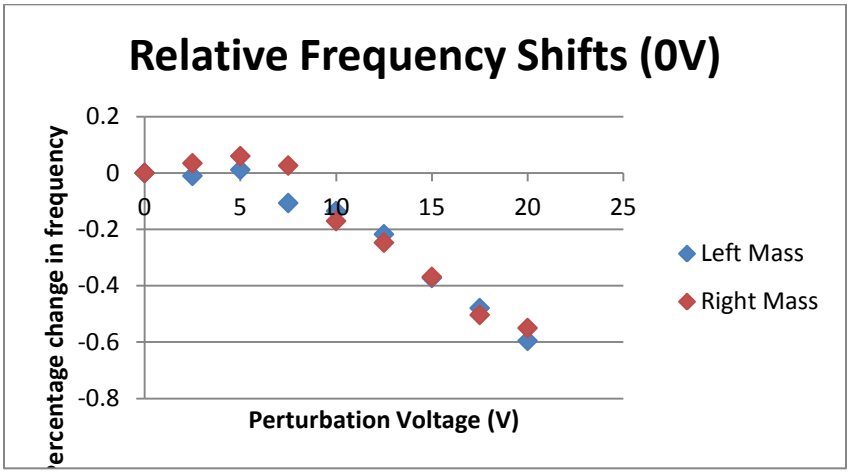

Figure 3.22: Relative shifts in resonant frequency using the 0 V perturbation data as a reference

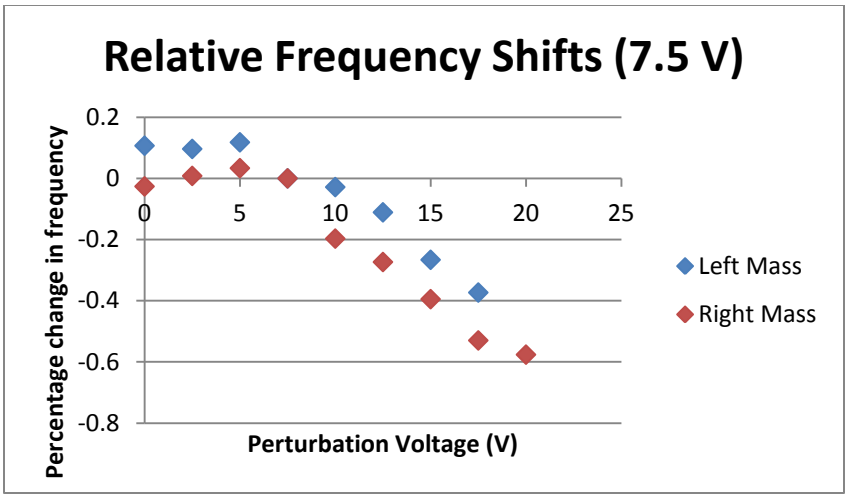

Figure 3.23: Relative shifts in resonant frequency using the 7.5 V perturbation data as a reference

The main conclusion that can be drawn from Figure 3.22 and Figure 3.23 is that the magnitudes of the relative shifts in the resonant frequency are about 0.6% for maximum perturbation regardless of the chosen reference point.

3.5.2 Chip 1 with 18 V Coupling: Eigenvector Shifts

The eigenvector shifts are also calculated as first present in Chapter 2, that is:

$$\frac{|\boldsymbol{\varphi_n} - \boldsymbol{\varphi_{0n}}|}{|\boldsymbol{\varphi_{0n}}|} \tag{3.21}$$

In order to populate the eigenvectors from the analyzed data there are several choices. The first is to use the peak values from each of the resonators for each perturbation voltage:

$$\boldsymbol{\varphi} = \begin{bmatrix} A_{max1} \\ A_{max2} \end{bmatrix} \tag{3.22}$$

However, since the maximum amplitudes for each mass occur at different frequencies for each perturbation level, it makes more sense to use the analyzed data twice. Once populating the vectors with the maximum amplitude for the first

resonator and the amplitude of vibration for the second resonator at the frequency associated with maximum amplitude for the first resonator and vice versa.

$$\boldsymbol{\varphi} = \begin{bmatrix} A_{max1} \\ A_{2@frequency\ for\ max1} \end{bmatrix} \text{ or } \boldsymbol{\varphi} = \begin{bmatrix} A_{1@frequency\ for\ max2} \\ A_{max2} \end{bmatrix} \tag{3.23}$$

The plots of the relative eigenvector shifts are found in Figure 3.24 and Figure 3.25.

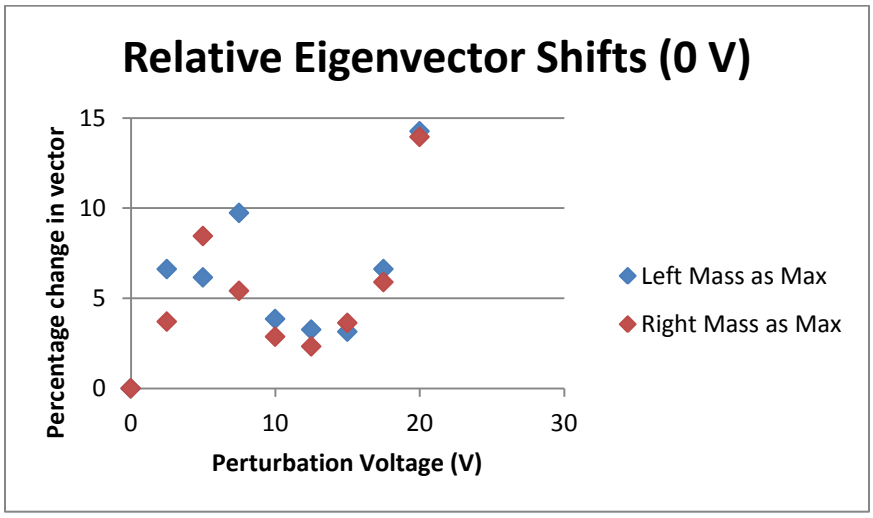

Figure 3.24: Percentage change in eigenvectors using 0 V perturbation as the reference. The blue points populate the original vectors with the absolute maximum for the left mass and the associated right mass amplitude for that frequency.

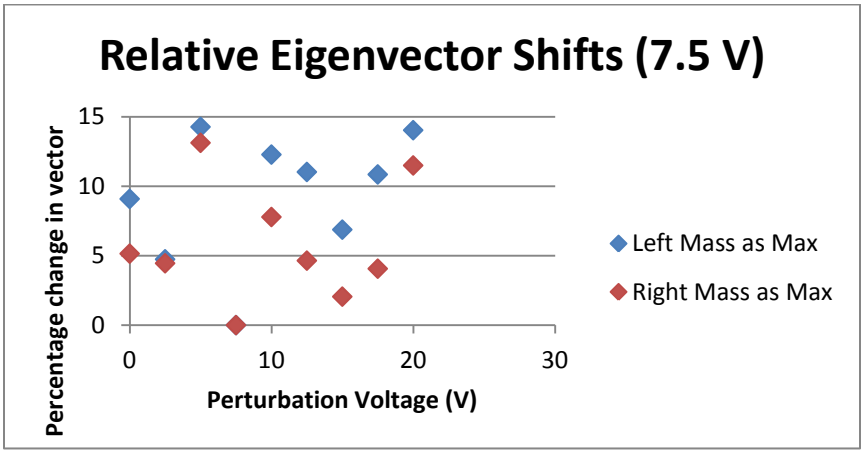

Figure 3.25: Percentage change in eigenvectors using 7.5 V perturbation as the reference. The blue points populate the original vectors with the absolute maximum for the left mass and the associated right mass amplitude for that frequency.

It is difficult to discern a trend in the above data though it may be noticed that the percentage change in the eigenvectors is generally more than an order of magnitude greater than the percentage change in the resonant frequencies. This result will be discussed in greater detail at the end of the chapter.

3.5.3 Chip 2 with 18 V Coupling: Resonant Frequency Shifts

As with the first chip earlier, the first plot (Figure 3.26) presented here depicts the absolute changes in resonant frequency for each of the masses for each perturbation voltage.

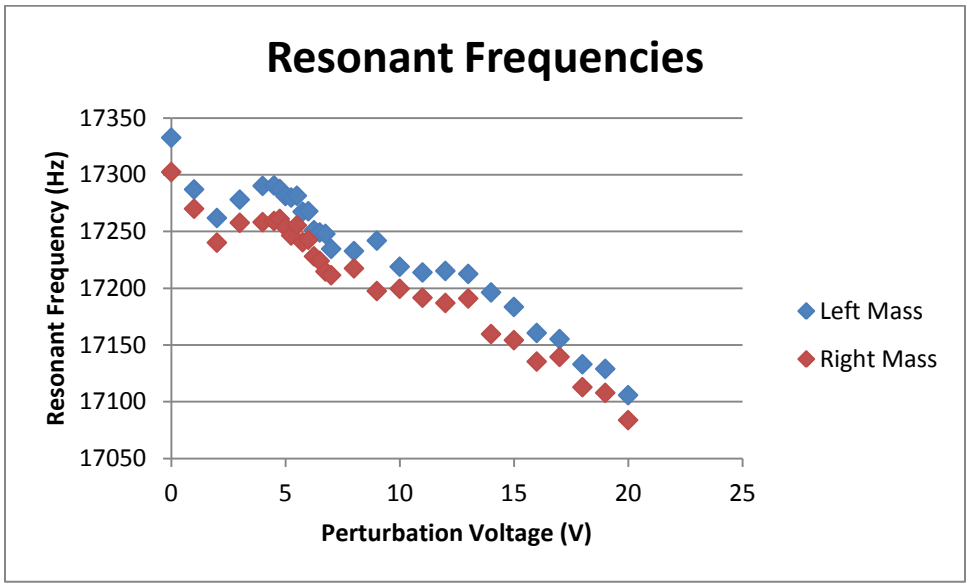

Figure 3.26: Absolute change in resonant frequency for different perturbation potentials on Chip 2

Again the resonant frequencies trend down as perturbation voltage increases. The difference between the left and right mass resonant frequencies was computed and it was found that the smallest difference was for an 8 V perturbation. This means that two different chips both exhibited the greatest degree of symmetry for this excitation method around the same perturbation voltage (7.5 V versus 8 V). For this

data, the relative shifts in the resonant frequency were therefore calculated using 0 V as a reference and with 8 V as a reference. This can be seen in the following two plots (Figure 3.27 and Figure 3.28).

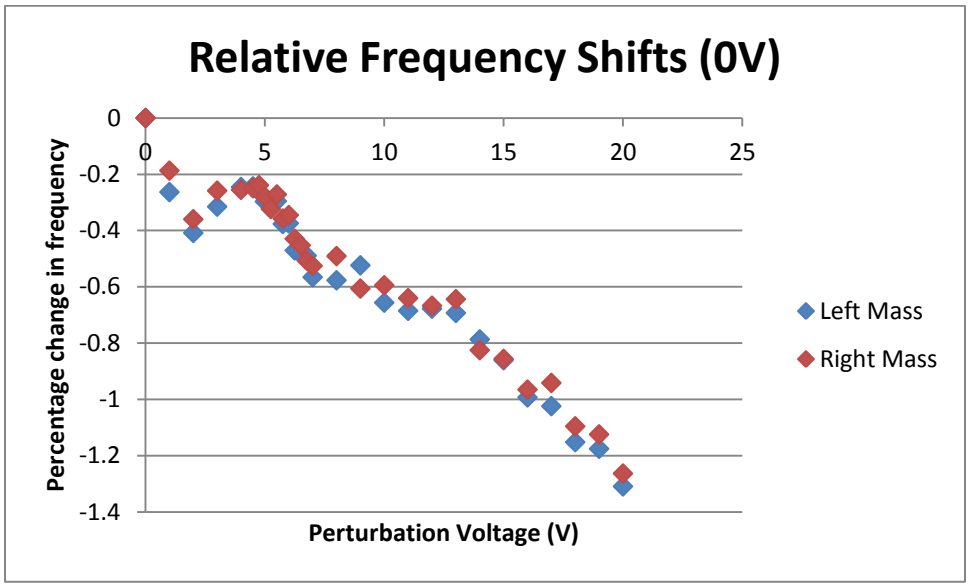

Figure 3.27: Relative shifts in resonant frequency using the 0 V perturbation data as a reference

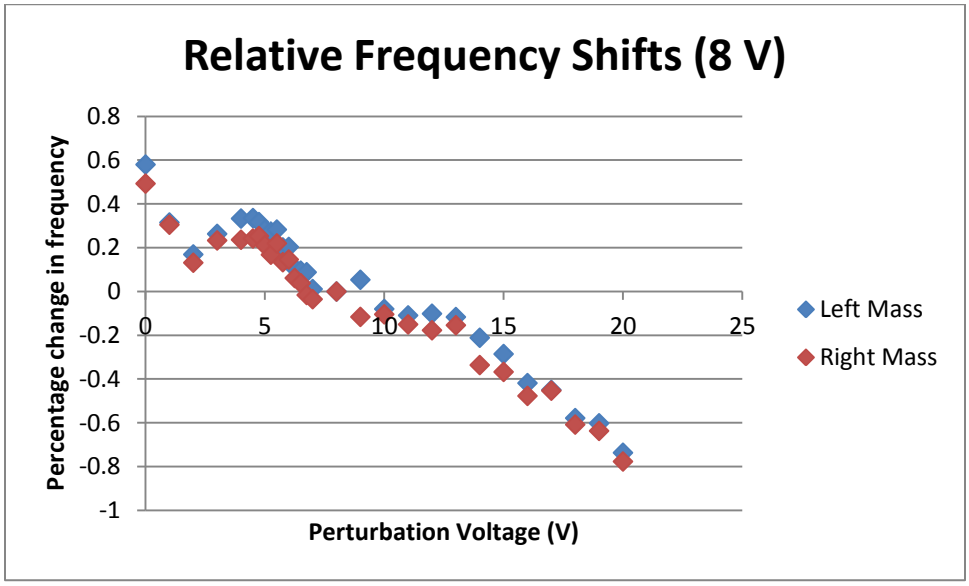

Figure 3.28: Relative shifts in resonant frequency using the 8 V perturbation data as a reference

Figure 3.27 and Figure 3.28 both show that the overall relative frequency shift for this chip is about 1.4% regardless of reference point.

3.5.4 Chip 2 with 18 V Coupling: Eigenvector Shifts

The same plots that were produced for the first chip are repeated here (Figure 3.29 and Figure 3.30) but, again, no trend is readily identifiable. Compared with the first chip, the relative eigenvector changes are also higher and again are more than an order of magnitude greater than the relative shifts in the estimated resonant frequencies.

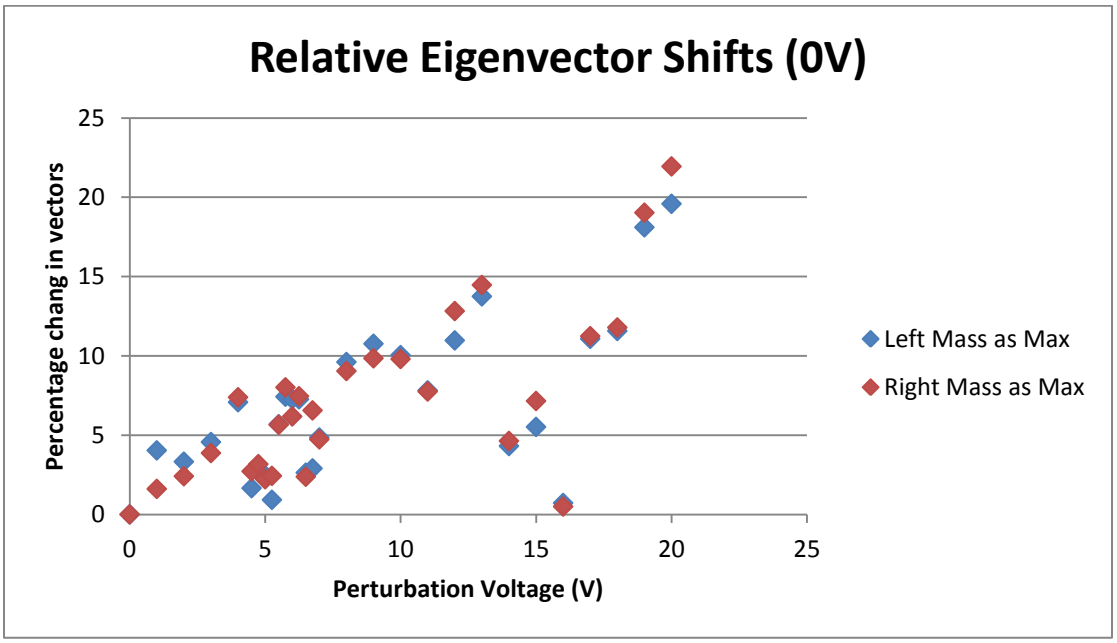

Figure 3.29: Percentage change in eigenvectors using 0 V perturbation as the reference. The blue points populate the original vectors with the absolute maximum for the left mass and the associated right mass amplitude for that frequency.

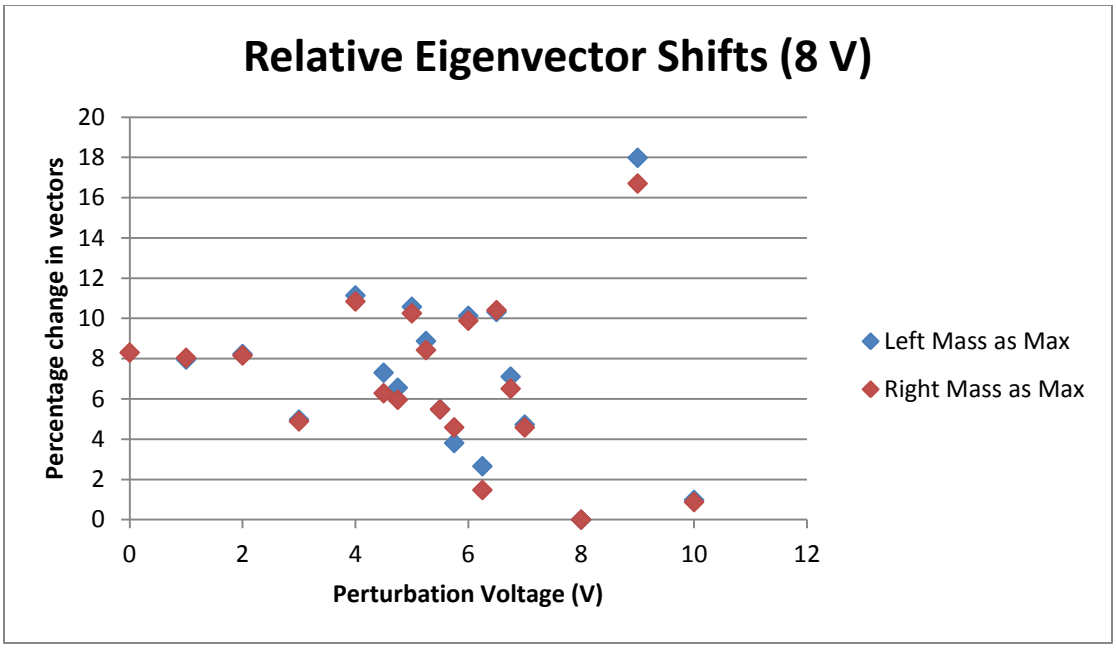

Figure 3.30: Percentage change in eigenvectors using 8 V perturbation as the reference. The blue points populate the original vectors with the absolute maximum for the left mass and the associated right mass amplitude for that frequency.

3.5.5 Chip 2 with 23 V Coupling: Resonant Frequency Shifts

The second chip was tested a second time with a 23 V potential across the coupling gap. Due to the coupling stiffness dependence on the square of the voltage, this would yield about a 60% increase in coupling stiffness with all else being equal. The intention of this test was to demonstrate the tunability of the coupling leading to the ability to control the range and sensitivity of a sensor based on the veering principle. The data was analyzed in the same way as before and can be seen in Figure 3.31, Figure 3.32, and Figure 3.33.

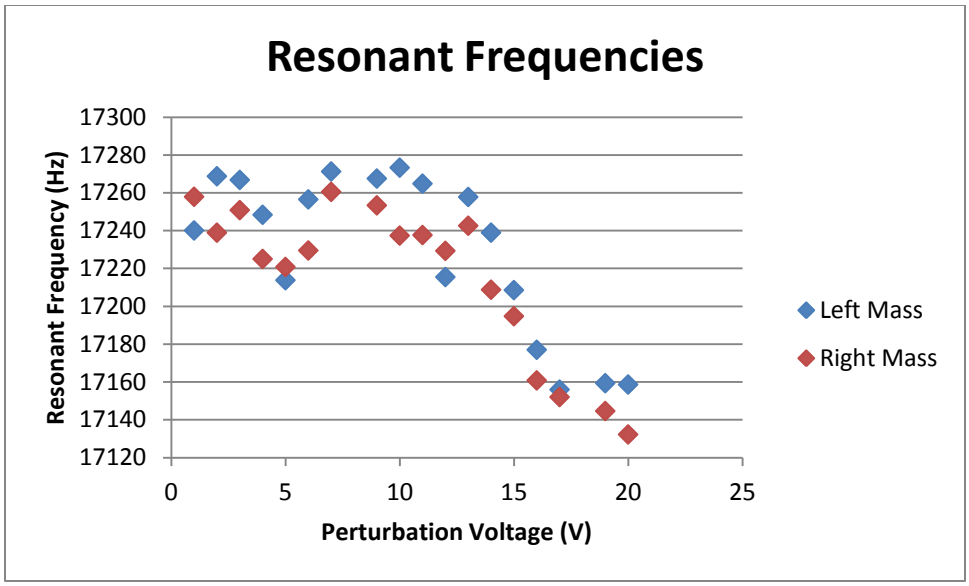

Figure 3.31: Absolute change in resonant frequency for different perturbation potentials

For this configuration, the minimum separation between the left and right resonant frequencies (greatest symmetry) was for a 5 V perturbation.

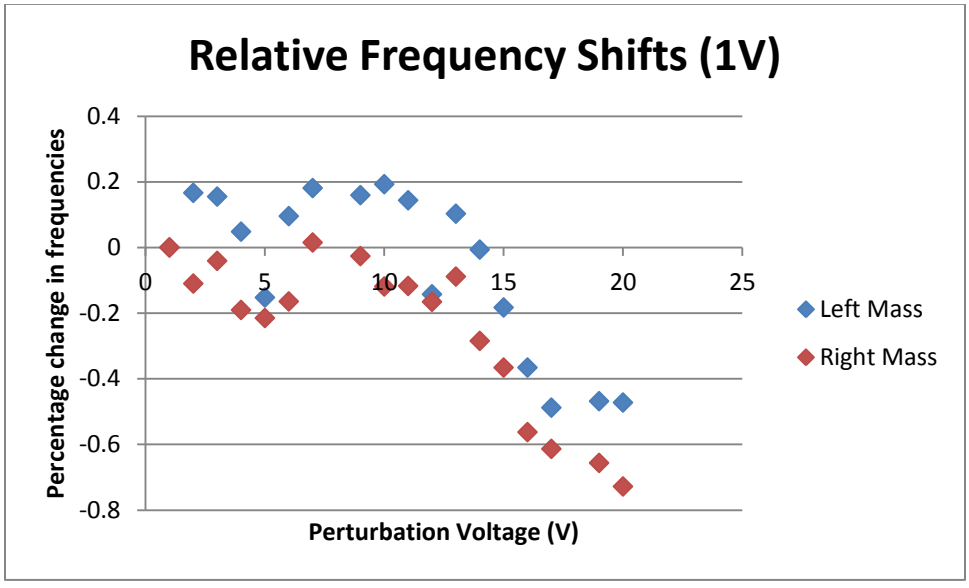

Figure 3.32: Relative shifts in resonant frequency using the 1 V perturbation data as a reference

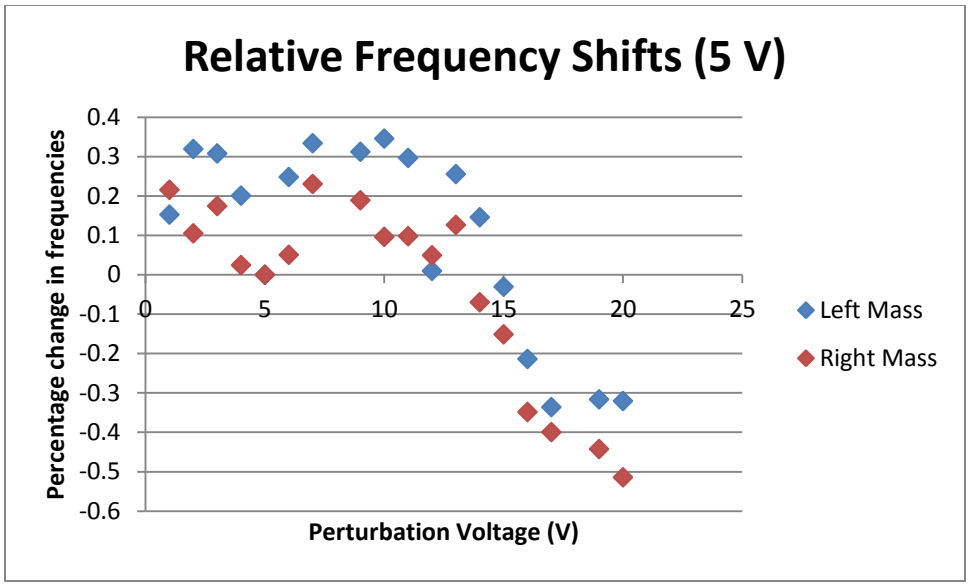

Figure 3.33: Relative shifts in resonant frequency using the 5 V perturbation data as a reference

The relative shifts in resonant frequency continue to be about 1%.

3.5.6 Chip 2 with 23 V Coupling: Eigenvector Shifts

The analyzed data for the eigenvector shifts continues to be difficult to interpret. Ideally, with a stronger coupling a reduced sensitivity to the perturbation voltage should have been demonstrated. However, little change is seen in the data (see Figure 3.34 and Figure 3.35). It continues to exhibit an undefined trend but still shows at least an order of magnitude gain over the shifts in resonant frequency. It does not demonstrate a reduced sensitivity. The cause of this will be discussed in the next section.

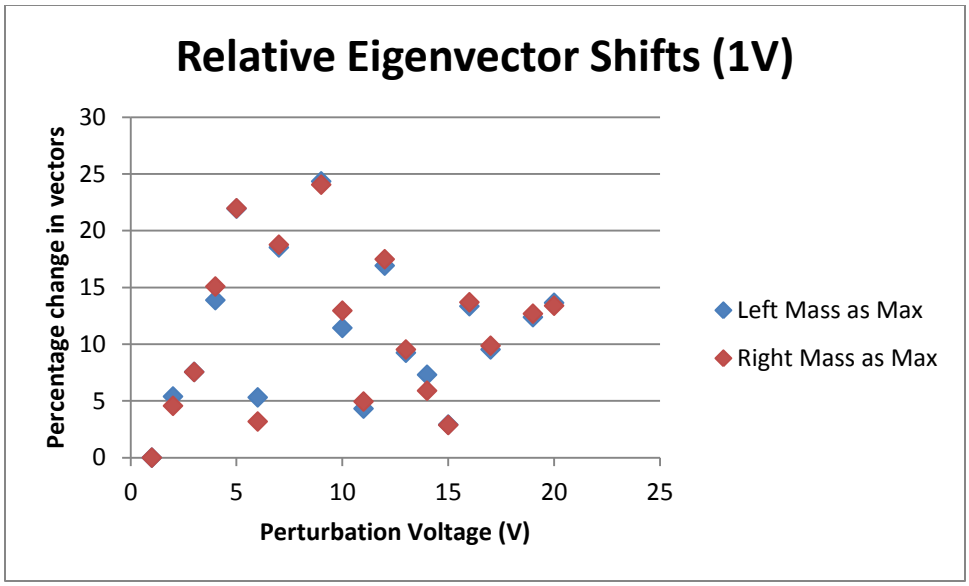

Figure 3.34: Percentage change in eigenvectors using 0 V perturbation as the reference. The blue points populate the original vectors with the absolute maximum for the left mass and the associated right mass amplitude for that frequency.

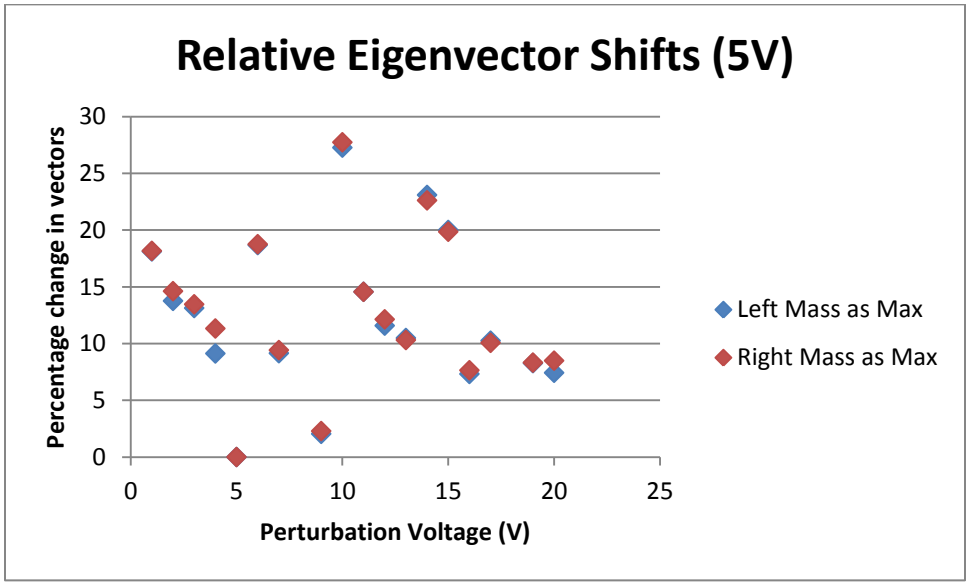

Figure 3.35: Percentage change in eigenvectors using 5 V perturbation as the reference. The blue points populate the original vectors with the absolute maximum for the left mass and the associated right mass amplitude for that frequency.

3.5.7 Discussion of Results

Overall it seems that the behaviour of the resonant frequencies was as expected. That is, they decreased with increasing perturbation voltage with a definite trend. The eigenvector shifts were not so well behaved. In general, the eigenvector shifts were an order of magnitude greater than the shifts in frequency but there is not one definite trend. This behaviour is attributed to two factors: nonlinearities at high perturbation voltages and a time-varying stiffness of the coupling between the two resonators.

The time-varying stiffness is likely the dominant effect since there can be up to a 300% range in stiffness values between measurements. This is due both to the superposition of modes and to the nature of energy localization since both contribute to modulate the gap distance in the coupling. In a perfectly symmetric system with no perturbation, the coupling gap distance is constant when excited in the in-phase mode. This is not realizable practically so even for a symmetric system, the contribution of the anti-phase mode in the superposition leads to a time-varying gap. Energy localization also leads to a time-varying gap since it is manifested as a difference in amplitude of vibration for each resonator even if the resonant frequency and phase is identical. In this system, the gap distance is designed to be 2 μm. The amplitudes of vibration are on the order of 0.2 μm. This means the range of the gap distance is about 1.6 μm (for purely anti-phase at minimum separation) to 2.4 μm (for purely anti-phase at maximum separation. Since the coupling magnitude is inversely proportional to the cube of gap distance, the coupling stiffness for a 1.6 μm gap is more than three times stronger than the coupling stiffness for a 2.4 μm gap.

The time-varying nature of the coupling stiffness can then be used to rationalize the measured relative shifts of the eigenvector. Since the coupling stiffness is already much less than the grounding spring stiffness, the shifts in eigenvectors are expected to be larger than the shifts in resonant frequency. This is observed (compare ~20% shift in the eigenvectors to a 1.4% shift in the resonant frequencies of the second chip for an 18 V coupling). However, a trend in the eigenvector shifts was not isolated in this thesis since it is impossible to predict the coupling gap for each measurement or to account for its change during the course of a measurement. This time-varying nature needs to be addressed in future designs in order to better compare the shift in eigenvectors to the theory.

Chapter 4: Three Degree of Freedom Systems

As has been demonstrated theoretically and experimentally, an improvement in sensitivity to perturbation can be attained using a 2DOF system when compared to a single DOF system. Here the idea is extended to 3DOF systems analytically and with simulated results.

4.1 Introduction

Similar to Chapter 2, here a 3DOF system free from damping will be analyzed. The basic system is described schematically in Figure 4.1. For the 3DOF system, each mass is suspended by a grounding spring referred to as 'k_j' where the subscript 'j' denotes the mass number. The coupling springs are labeled '$k_{j,j+1}$' where the subscript denotes the two masses which the spring couples.

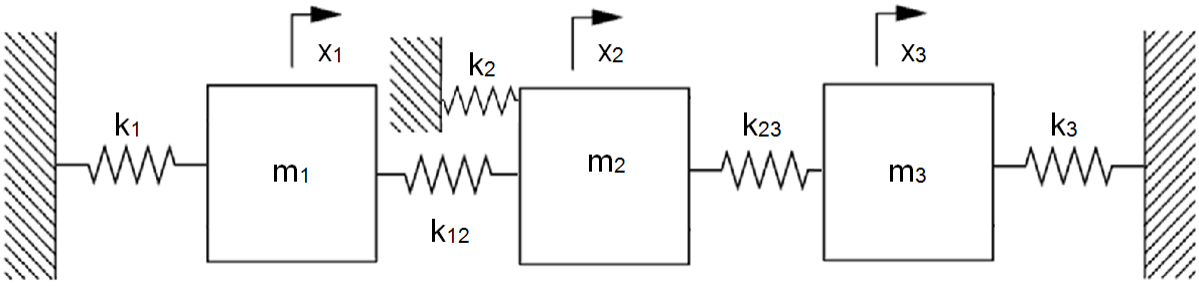

Figure 4.1: Schematic of the 3DOF spring-mass system

In the case of the 3DOF system, there are multiple approaches to perturbing the system. One option is to perturb any one of the masses. This yields two unique approaches since the system is symmetric and therefore a perturbation only on mass one is equivalent to a perturbation applied only to mass three. Another option, which lends itself to differential sensing, is to perturb the first mass and apply the

opposite perturbation to the third mass, for example increasing the stiffness of k_1 while decreasing the stiffness of k_3 by the same magnitude.

4.1.1 Vibration Modes

In addition to choosing how to perturb the system, it is also important to know what the mode shapes look like. The first mode (lowest frequency) is the in-phase mode in which all three masses oscillate with the same phase and the same amplitude. This differs slightly from the more classic 3DOF spring-mass system in which the center mass does not have its own grounding spring. In the classic system, the amplitude of vibration for the center mass in the first mode is a factor of $\sqrt{2}$ larger than either the amplitude of the first or third mass.

In the second mode, the first and third masses oscillate out-of-phase with each other but with the same amplitude and the middle mass remains stationary.

In the third mode (highest frequency), the first and third mass oscillate in phase with each other and the middle mass oscillates out-of-phase with each of the others and with an amplitude that is twice as large. These modes are true for positive coupling springs, but the first and third modes will be swapped for negative coupling.

It is important to note that the scheme in which only the middle mass is perturbed will have no effect on the system if it is being driven in the second mode since the middle mass is motionless in this mode regardless of coupling.

4.1.2 Veering in 3DOF Systems

Another difference between 2DOF and 3DOF systems is the number of veering zones. A graphical depiction of the veering zones for a 3DOF system with positive

coupling can be found in Figure 4.2. Just like in the 2DOF system, the trajectories of the loci of the eigenvalues seem to “trade” between modes.

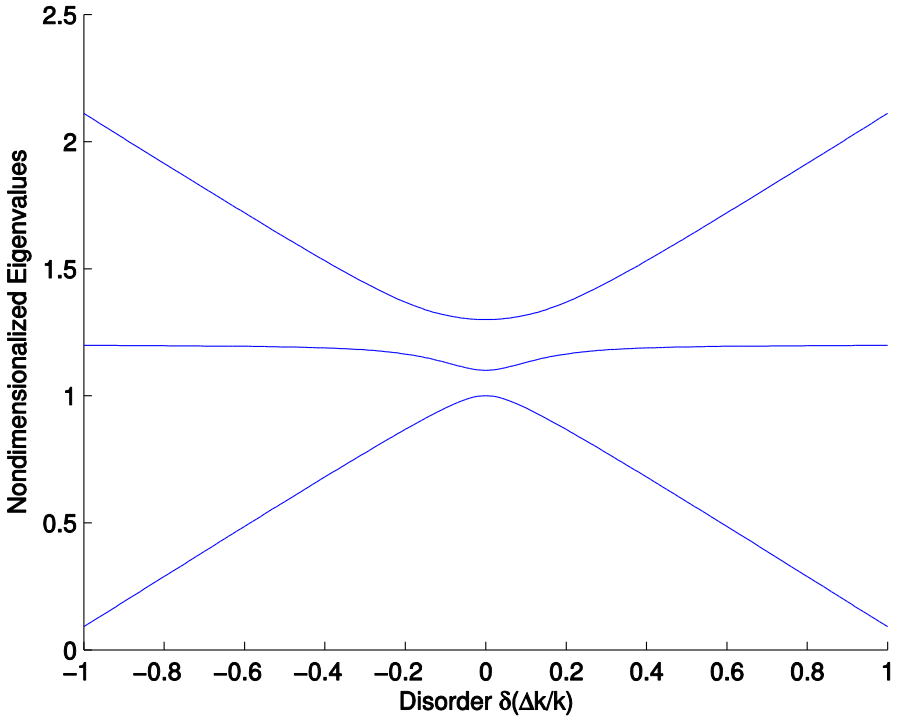

Figure 4.2: Graphical depiction of veering in the 3DOF system with positive coupling

4.2 Perturbation on the Third Mass

For 3DOF systems, the approach used in Chapter 2 for solving for the eigenvalue and eigenvector sensitivities is unwieldy. Instead, the eigen derivatives method will be used. This approach yields the same results for a 2DOF system as the approach used earlier which helps validate those findings. This approach was developed by Fox and Kapoor [29] and was found referenced in another paper by du Bois, Adhikari, and Lieven [30]. Using this method, the sensitivity of the eigenvalues to a disorder parameter is given by the following for an undamped system [30]:

$$\frac{\partial \lambda_i}{\partial \delta} = \boldsymbol{\phi}_i^T \left(\frac{\partial \boldsymbol{K}}{\partial \delta} - \lambda_i \frac{\partial \boldsymbol{M}}{\partial \delta} \right) \boldsymbol{\phi}_i \tag{4.1}$$

where λ_i is the eigenvalue and $\boldsymbol{\phi_i}$ is the mass-normalized eigenvector of the ith mode. $\boldsymbol{K}$ and $\boldsymbol{M}$ are the system's stiffness and mass matrices respectively.

The eigenvector sensitivity expression is also given [30]:

$$\frac{\partial \boldsymbol{\phi_i}}{\partial \delta} = -\frac{\boldsymbol{\phi_i^T}\frac{\partial \boldsymbol{M}}{\partial \delta}\boldsymbol{\phi_i}}{2}\boldsymbol{\phi_i} + \sum_{r \neq i}\frac{\boldsymbol{\phi_r^T}\left(\frac{\partial \boldsymbol{K}}{\partial \delta} - \lambda_i\frac{\partial \boldsymbol{M}}{\partial \delta}\right)\boldsymbol{\phi_i}}{\Delta\lambda_{ir}}\boldsymbol{\phi_r} \tag{4.2}$$

The definition of $\Delta\lambda_{ir}$ is simply $\lambda_i - \lambda_r$. The eigen derivatives method is a closed-form solution for "*a self-adjoint, discrete, undamped structural dynamic eigenproblem*" [30] and is valid for any number of degrees of freedom. Since we have high quality factors in MEMS, a good match is expected from this method.

This approach will now be used in full for this perturbation approach (stiffness perturbation on the third mass) in order to find the eigenvalue and eigenvector sensitivities as defined in Chapter 2. In the following sections, the results of this method will be summarized for the additional perturbation schemes introduced at the beginning of this chapter.

For the 3DOF system as defined earlier, the mass and stiffness matrices for the unperturbed system are as follows:

$$\boldsymbol{K} = \begin{pmatrix} k + k_c & -k_c & 0 \\ -k_c & k + 2k_c & -k_c \\ 0 & -k_c & k + k_c \end{pmatrix} \text{ and } \boldsymbol{M} = \begin{pmatrix} m & 0 & 0 \\ 0 & m & 0 \\ 0 & 0 & m \end{pmatrix} \tag{4.3}$$

This assumes that $k_1 = k_2 = k_3 = k$ and $k_{12} = k_{23} = k_c$ and that all of the masses are identical. This would be true of a symmetric system. As before, a modified stiffness matrix is used which scales the original stiffness matrix by a factor of $\frac{1}{k}$.

$$\boldsymbol{K} = \begin{pmatrix} 1+\kappa & -\kappa & 0 \\ -\kappa & 1+2\kappa & -\kappa \\ 0 & -\kappa & 1+\kappa \end{pmatrix}, \kappa = \frac{k_c}{k} \tag{4.4}$$

Using the same definition of the eigenvalue problem as in Chapter 2, the eigenvalues and mass-normalized eigenvectors for the 3DOF system are:

$$\lambda_{01} = 1 \qquad \boldsymbol{\phi_{01}} = \begin{bmatrix} \frac{1}{\sqrt{3}} \\ \frac{1}{\sqrt{3}} \\ \frac{1}{\sqrt{3}} \end{bmatrix}$$

$$\lambda_{02} = 1+\kappa \qquad \boldsymbol{\phi_{02}} = \begin{bmatrix} \frac{-1}{\sqrt{2}} \\ 0 \\ \frac{1}{\sqrt{2}} \end{bmatrix} \tag{4.5}$$

$$\lambda_{03} = 1+3\kappa \qquad \boldsymbol{\phi_{03}} = \begin{bmatrix} \frac{1}{\sqrt{6}} \\ \frac{-\sqrt{2}}{\sqrt{3}} \\ \frac{1}{\sqrt{6}} \end{bmatrix}$$

These eigenvalues and eigenvectors are the basis for the analysis. At this point, the mass and stiffness matrices for the perturbed system need to be defined. For a stiffness perturbation applied only to the third mass, these matrices are:

$$\boldsymbol{K} = \begin{pmatrix} 1+\kappa & -\kappa & 0 \\ -\kappa & 1+2\kappa & -\kappa \\ 0 & -\kappa & 1+\kappa+\delta \end{pmatrix} \text{ and } \boldsymbol{M} = \begin{pmatrix} m & 0 & 0 \\ 0 & m & 0 \\ 0 & 0 & m \end{pmatrix}, \delta = \frac{\Delta k}{k}, \kappa = \frac{k_c}{k} \tag{4.6}$$

4.2.1 Sensitivity of the Eigenvalue for the First Mode

Using the eigenvalue derivative equation, the sensitivity of λ_{01} to the disorder parameter is found by simply substituting the relevant vectors and matrices. The derivative of the stiffness matrix to the disorder parameter is trivial to solve since the perturbation is added to the original stiffness. The derivative of the mass matrix will be zero throughout since only a stiffness perturbation is considered here.

$$\frac{\partial \lambda_{01}}{\partial \delta} = \begin{bmatrix} \frac{1}{\sqrt{3}} & \frac{1}{\sqrt{3}} & \frac{1}{\sqrt{3}} \end{bmatrix} \begin{bmatrix} 0 & 0 & 0 \\ 0 & 0 & 0 \\ 0 & 0 & 1 \end{bmatrix} \begin{bmatrix} \frac{1}{\sqrt{3}} \\ \frac{1}{\sqrt{3}} \\ \frac{1}{\sqrt{3}} \end{bmatrix} = \frac{1}{3} \tag{4.7}$$

$$\lambda_1 = \lambda_{01} + \delta \frac{\partial \lambda_{01}}{\partial \delta} = \lambda_{01} + \frac{\delta}{3} \tag{4.8}$$

$$\frac{\lambda_1 - \lambda_{01}}{\lambda_{01}} = \frac{1 + \frac{\delta}{3} - 1}{1} = \frac{\delta}{3} = \frac{\Delta k}{3k} \tag{4.9}$$

4.2.2 Sensitivity of the Eigenvalue for the Second Mode

The same approach applied to the second eigenvalue actuated in the second mode:

$$\frac{\partial \lambda_{02}}{\partial \delta} = \begin{bmatrix} \frac{-1}{\sqrt{2}} & 0 & \frac{1}{\sqrt{2}} \end{bmatrix} \begin{bmatrix} 0 & 0 & 0 \\ 0 & 0 & 0 \\ 0 & 0 & 1 \end{bmatrix} \begin{bmatrix} \frac{-1}{\sqrt{2}} \\ 0 \\ \frac{1}{\sqrt{2}} \end{bmatrix} = \frac{1}{2} \tag{4.10}$$

$$\lambda_2 = \lambda_{02} + \frac{\delta}{2} \tag{4.11}$$

$$\frac{\lambda_2 - \lambda_{02}}{\lambda_{02}} = \frac{\delta}{2} = \frac{\Delta k}{2k} \text{ iff } k_c \ll k \tag{4.12}$$

In this thesis the magnitude of the coupling stiffness has normally been regarded to be much smaller than for a grounding spring. This simplification will continue to be used throughout this analysis.

4.2.3 Sensitivity of the Eigenvalue for the Third Mode

And again for the third mode:

$$\frac{\partial \lambda_{03}}{\partial \delta} = \begin{bmatrix} \frac{1}{\sqrt{6}} & \frac{-\sqrt{2}}{\sqrt{3}} & \frac{1}{\sqrt{6}} \end{bmatrix} \begin{bmatrix} 0 & 0 & 0 \\ 0 & 0 & 0 \\ 0 & 0 & 1 \end{bmatrix} \begin{bmatrix} \frac{1}{\sqrt{6}} \\ \frac{-\sqrt{2}}{\sqrt{3}} \\ \frac{1}{\sqrt{6}} \end{bmatrix} = \frac{1}{6} \tag{4.13}$$

$$\lambda_3 = \lambda_{03} + \frac{\delta}{6} \tag{4.14}$$

$$\frac{\lambda_3 - \lambda_{03}}{\lambda_{03}} = \frac{\delta}{6} = \frac{\Delta k}{6k} \; iff \; k_c \ll k \tag{4.15}$$

Unlike in the 2DOF system, it is shown that the sensitivity of the eigenvalues is different for each mode.

4.2.4 Sensitivity of the Eigenvector for the First Mode

Again, using the eigenvector sensitivity equation and making the relevant substitutions, the sensitivity of the first eigenvector to the disorder parameter is found.

$$\frac{\partial \boldsymbol{\phi_{01}}}{\partial \delta} = \frac{\begin{bmatrix} -\frac{1}{\sqrt{2}} & 0 & 1/\sqrt{2} \end{bmatrix} \begin{bmatrix} 0 & 0 & 0 \\ 0 & 0 & 0 \\ 0 & 0 & 1 \end{bmatrix} \begin{bmatrix} \frac{1}{\sqrt{3}} \\ \frac{1}{\sqrt{3}} \\ \frac{1}{\sqrt{3}} \end{bmatrix}}{1 - (1+\kappa)} \begin{bmatrix} -\frac{1}{\sqrt{2}} \\ 0 \\ \frac{1}{\sqrt{2}} \end{bmatrix} + \frac{\begin{bmatrix} \frac{1}{\sqrt{6}} & -\frac{\sqrt{2}}{\sqrt{3}} & \frac{1}{\sqrt{6}} \end{bmatrix} \begin{bmatrix} 0 & 0 & 0 \\ 0 & 0 & 0 \\ 0 & 0 & 1 \end{bmatrix} \begin{bmatrix} \frac{1}{\sqrt{3}} \\ \frac{1}{\sqrt{3}} \\ \frac{1}{\sqrt{3}} \end{bmatrix}}{1 - (1+3\kappa)} \begin{bmatrix} \frac{1}{\sqrt{6}} \\ -\frac{\sqrt{2}}{\sqrt{3}} \\ \frac{1}{\sqrt{6}} \end{bmatrix} \tag{4.16}$$

$$\frac{\partial \boldsymbol{\phi_{01}}}{\partial \delta} = -\frac{1}{\sqrt{2}\sqrt{3}\kappa} \begin{bmatrix} -\frac{1}{\sqrt{2}} \\ 0 \\ \frac{1}{\sqrt{2}} \end{bmatrix} + \frac{-1}{\sqrt{6}\sqrt{3}3\kappa} \begin{bmatrix} \frac{1}{\sqrt{6}} \\ -\frac{\sqrt{2}}{\sqrt{3}} \\ \frac{1}{\sqrt{6}} \end{bmatrix} \tag{4.17}$$

Since the length of all of the mass-normalized eigenvector is 1, the sensitivity of the eigenvectors as defined in Chapter 2, $\frac{|\boldsymbol{\phi_1} - \boldsymbol{\phi_{01}}|}{|\boldsymbol{\phi_{01}}|}$, is simply the length of the product of δ with (4.17).

$$(4.17)\delta = \begin{bmatrix} \frac{\delta}{2\sqrt{3}\kappa} \\ 0 \\ \frac{-\delta}{2\sqrt{3}\kappa} \end{bmatrix} + \begin{bmatrix} -\frac{\delta}{6\sqrt{3}3\kappa} \\ \frac{\sqrt{2}\delta}{\sqrt{6}3^2\kappa} \\ -\frac{\delta}{6\sqrt{3}3\kappa} \end{bmatrix} = \begin{bmatrix} \frac{4\sqrt{3}\delta}{27\kappa} \\ \frac{\sqrt{3}\delta}{27\kappa} \\ \frac{-5\sqrt{3}\delta}{27\kappa} \end{bmatrix} \tag{4.18}$$

$$\frac{|\boldsymbol{\phi_1} - \boldsymbol{\phi_{01}}|}{|\boldsymbol{\phi_{01}}|} = \frac{\sqrt{126}}{27}\frac{\delta}{\kappa} = \frac{\sqrt{126}}{27}\frac{\Delta k}{k_c} \approx 0.42\frac{\Delta k}{k_c} \tag{4.19}$$

Therefore, the sensitivity of the first eigenvector is about 68% greater than for an equivalent 2DOF system ($\frac{|\boldsymbol{\phi_1} - \boldsymbol{\phi_{01}}|}{|\boldsymbol{\phi_{01}}|} = 0.25\frac{\Delta k}{k_c}$).

4.2.5 Sensitivity of the Eigenvector for the Second Mode

Repeating the procedure for the eigenvector of the second mode, the sensitivity is found to be:

$$\frac{|\boldsymbol{\phi_2} - \boldsymbol{\phi_{02}}|}{|\boldsymbol{\phi_{02}}|} = \frac{\sqrt{12}}{8}\frac{\delta}{\kappa} \approx 0.43\frac{\Delta k}{k_c} \tag{4.20}$$

This is an improvement of about 72% over the 2DOF system.

4.2.6 Sensitivity of the Eigenvector for the Third Mode

Repeating the procedure a third time for the eigenvector of the third mode, the sensitivity is found to be:

$$\frac{|\boldsymbol{\phi_3} - \boldsymbol{\phi_{03}}|}{|\boldsymbol{\phi_{03}}|} = \frac{\sqrt{29}}{\sqrt{324}}\frac{\delta}{\kappa} \approx 0.30\frac{\Delta k}{k_c} \tag{4.21}$$

This is an improvement of about 20% over the 2DOF system.

4.2.7 Summary of the Perturbation on the Third Mass Scheme

Comparing the sensitivities of the eigenvectors, it is seen that actuation in the second mode yields the greatest sensitivity. It is also trivial to show that for coupling stiffnesses $k_c < 0.86k$, the sensitivity of the eigenvector when excited in the second mode is greater than the sensitivity of the eigenvalue when excited in the second mode. This requirement is actually less restrictive than it was in the 2DOF system. Finally, all else being equal, it is seen that the sensitivity of the eigenvector in the second mode is about 70% better than for a 2DOF at the expense of area of the sensor and complexity (signal processing on three output signals rather than two).

4.3 Perturbation on the Center Mass

Another suggested technique was to perturb just the center mass. The results of the eigen derivative method are presented here. In this scheme, the mass and stiffness matrices for the system are:

$$\boldsymbol{K} = \begin{pmatrix} 1+\kappa & -\kappa & 0 \\ -\kappa & 1+2\kappa+\delta & -\kappa \\ 0 & -\kappa & 1+\kappa \end{pmatrix} \text{ and } \boldsymbol{M} = \begin{pmatrix} m & 0 & 0 \\ 0 & m & 0 \\ 0 & 0 & m \end{pmatrix}, \delta = \frac{\Delta k}{k} \tag{4.22}$$

4.3.1 Eigenvalue Sensitivities for Center Mass Stiffness Perturbation

$$\frac{\lambda_1 - \lambda_{01}}{\lambda_{01}} = \frac{\delta}{3} = \frac{\Delta k}{3k} \tag{4.23}$$

$$\frac{\lambda_2 - \lambda_{02}}{\lambda_{02}} = 0 \tag{4.24}$$

$$\frac{\lambda_1 - \lambda_{01}}{\lambda_{01}} = \frac{2\delta}{3} = \frac{2\Delta k}{3k} \; iff \; k_c \ll k \tag{4.25}$$

The most interesting thing to notice about this scheme is that the calculated sensitivity of the eigenvalue of the second mode is zero. This result can be explained intuitively since in the second mode the center mass is stationary, i.e. its grounding spring does not do any work. If the spring doesn't do work, changes to its stiffness will not be manifested elsewhere. This will also be true of the eigenvector sensitivity of the second mode.

4.3.2 Eigenvector Sensitivities for Center Mass Stiffness Perturbation

$$\frac{|\boldsymbol{\phi_1} - \boldsymbol{\phi_{01}}|}{|\boldsymbol{\phi_{01}}|} = \frac{\sqrt{2}}{9}\frac{\delta}{\kappa} \approx 0.16\frac{\Delta k}{k_c} \tag{4.26}$$

$$\frac{|\boldsymbol{\phi_2} - \boldsymbol{\phi_{02}}|}{|\boldsymbol{\phi_{02}}|} = 0 \tag{4.27}$$

$$\frac{|\boldsymbol{\phi_3} - \boldsymbol{\phi_{03}}|}{|\boldsymbol{\phi_{03}}|} = \frac{\sqrt{2}}{\sqrt{9}}\frac{\delta}{\kappa} \approx 0.16\frac{\Delta k}{k_c} \tag{4.28}$$

Unsurprisingly, given the symmetry of the system when perturbed under this scheme the sensitivities of the first and third eigenvectors are identical.

4.3.3 Summary of the Perturbation on the Center Mass Scheme

In this approach the second mode has no sensitivity to stiffness (or mass) perturbations. The sensitivities are equal for the eigenvectors actuated in either the first or third modes with coupling stiffness constraints of $k_c < 0.48k$ and $k_c < 0.24k$ respectively in order to achieve a greater sensitivity than the associated eigenvalues. However, these sensitivities are less than can be achieved with a 2DOF system. Therefore this approach is less suitable for sensing applications but it was important for completeness to explore the possibility.

4.4 Perturbation on the First and Third Masses

The last suggested technique was investigated since it seems to lend itself well to differential sensing. In this case a positive stiffness perturbation is applied to the first mass and a negative stiffness perturbation is applied to the third mass. As such, the stiffness and mass matrices for this system are as follows:

$$\boldsymbol{K} = \begin{pmatrix} 1+\kappa+\delta & -\kappa & 0 \\ -\kappa & 1+2\kappa & -\kappa \\ 0 & -\kappa & 1+\kappa-\delta \end{pmatrix} \text{ and } \boldsymbol{M} = \begin{pmatrix} m & 0 & 0 \\ 0 & m & 0 \\ 0 & 0 & m \end{pmatrix}, \delta = \frac{\Delta k}{k} \tag{4.29}$$

4.4.1 Eigenvalue Sensitivities

Somewhat surprisingly, the eigenvalue sensitivities for this approach are the same for each mode and are all zero!

$$\frac{\lambda_n - \lambda_{0n}}{\lambda_{0n}} = 0 \tag{4.30}$$

4.4.2 Eigenvector Sensitivities

Even though the sensitivities of the eigenvalues are zero for this scheme, the sensitivities of the eigenvectors are not. Using the same method as before, the sensitivities were found to be:

$$\frac{|\boldsymbol{\phi_1} - \boldsymbol{\phi_{01}}|}{|\boldsymbol{\phi_{01}}|} = \sqrt{\frac{2}{3}}\frac{\delta}{\kappa} \approx 0.82\frac{\Delta k}{k_c} \tag{4.31}$$

$$\frac{|\boldsymbol{\phi_2} - \boldsymbol{\phi_{02}}|}{|\boldsymbol{\phi_{02}}|} = \sqrt{\frac{3}{4}}\frac{\delta}{\kappa} \approx 0.87\frac{\Delta k}{k_c} \tag{4.32}$$

$$\frac{|\boldsymbol{\phi_3} - \boldsymbol{\phi_{03}}|}{|\boldsymbol{\phi_{03}}|} = \sqrt{\frac{1}{3}}\frac{\delta}{\kappa} \approx 0.29\frac{\Delta k}{k_c} \tag{4.33}$$

4.4.3 Summary of Sensitivities

Compared to the 2DOF system, all three of the modes exhibit sensitivity improvements which range from about 15% to 250% with all else being equal. Clearly this approach yields the greatest sensitivity improvement for the increase in area if the perturbation signal can be made differential. If, for example, only positive influences are available (such as mass adsorption at the surface), the scheme presented in Section 4.2 is the best. Since this system exhibited the greatest performance, the full mathematical analysis can be examined in Appendix C.

Perhaps the greatest benefit of this approach is not that the sensitivity improvement is the greatest of any system presented, but that the eigenvalues are insensitive to the perturbation. This means that the system doesn't require any feedback control to remain at resonance. Once excited in the desired mode (most likely the second since it provides the greatest sensitivity) the driving signal can remain constant. This is advantageous because of its simplicity and speed.

4.5 Comparison with Numerical Approach

A 3DOF system with a positive coupling was defined in MATLAB in order to compare the results of the eigen derivatives analytical method with a numeric approximation and show that they are virtually identical for the range of perturbations that are ±10% of the unperturbed stiffness. The differential approach to perturbation was used. The three modes are depicted in Figures 4.3 – 4.5.

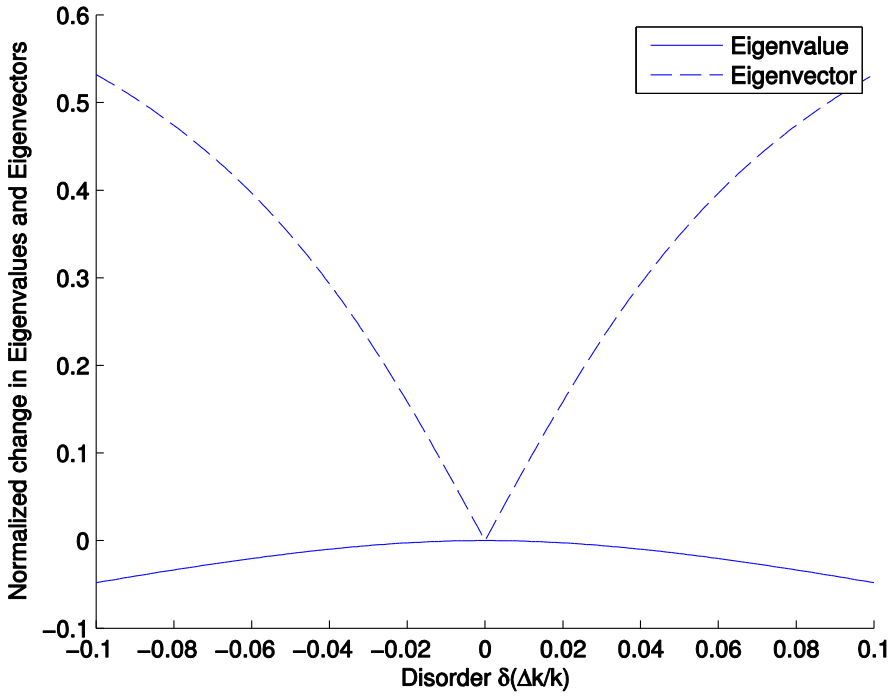

Figure 4.3: Comparison of eigenvector and eigenvalue sensitivities from a numerical analysis of the first mode for a 3DOF system with a coupling stiffness magnitude 1/10th of a grounding spring stiffness.

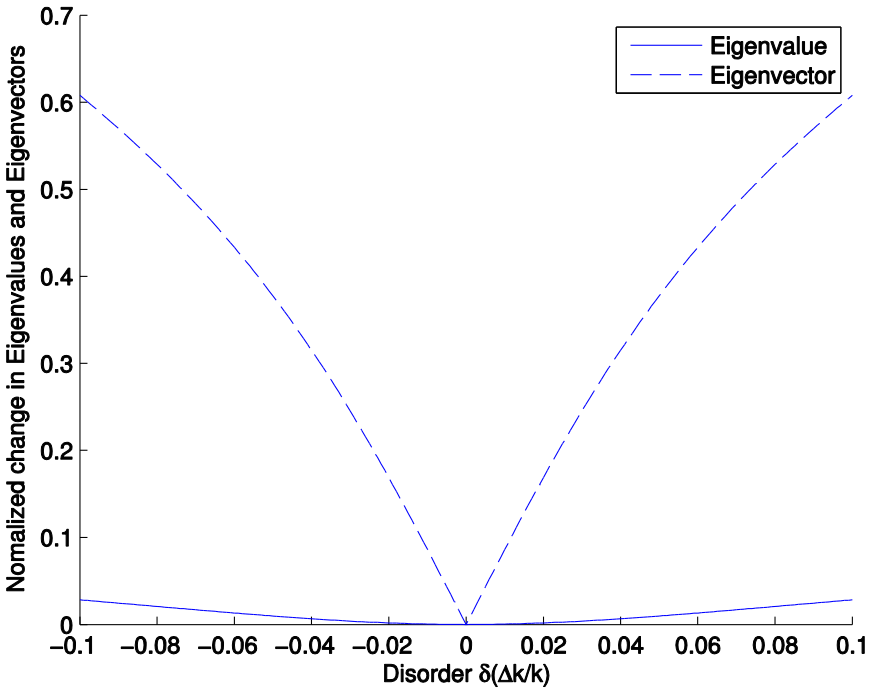

Figure 4.4: Comparison of eigenvector and eigenvalue sensitivities from a numerical analysis of the second mode for a 3DOF system.

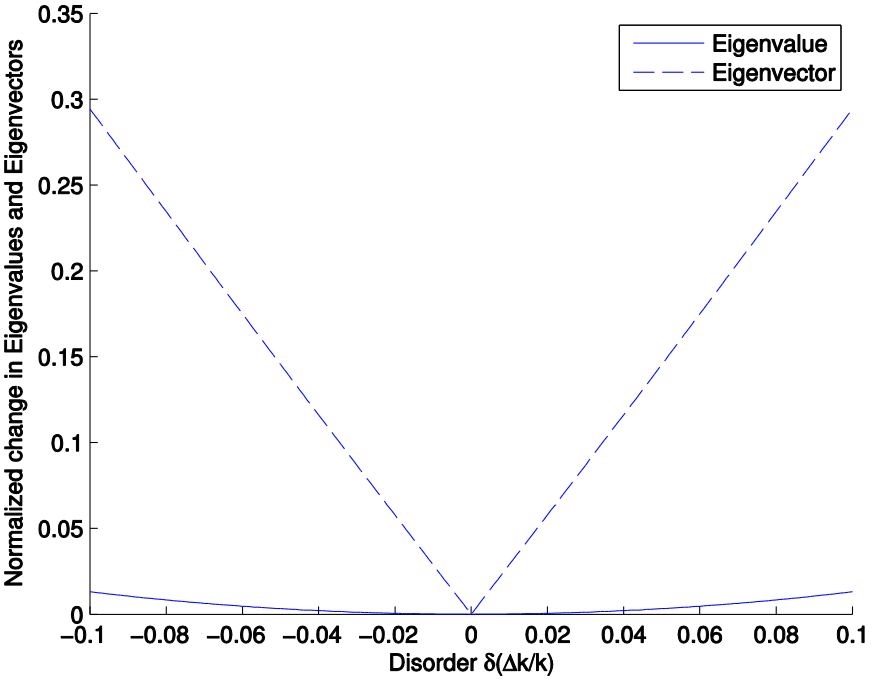

Figure 4.5: Comparison of eigenvector and eigenvalue sensitivities from a numerical analysis of the third mode for a 3DOF system.

The comparison can be made by noticing that the coupling stiffness magnitude is 10% of the grounding stiffness. Therefore the quantity $\frac{\Delta k}{k_c}$ becomes $10\left(\frac{\Delta k}{k}\right)$, with $\frac{\Delta k}{k}$ being the x-axis. The table below compares the analytical results with those found from the numerical simulation.

Table 4.1: Comparison of eigenvector and eigenvalue sensitivities from analytical and numerical approaches for 1% perturbation

	Eigenvalues		**Eigenvectors**	
Mode	**Analytical**	**Numerical**	**Analytical**	**Numerical**
First	0	0.00066	0.82	0.81
Second	0	0.00045	0.87	0.86
Third	0	0.00013	0.29	0.29

Table 4.2: Comparison of eigenvector and eigenvalue sensitivities from analytical and numerical approaches for 10% perturbation

	Eigenvalues		**Eigenvectors**	
Mode	**Analytical**	**Numerical**	**Analytical**	**Numerical**
First	0	0.048	0.82	0.53
Second	0	0.028	0.87	0.61
Third	0	0.013	0.29	0.29

The comparison shows that the analytical eigenvalue sensitivity expression is compelling for even a large perturbation of 10%. The analytical eigenvector sensitivity expression is only about 1.2% off at worst for a 1% perturbation but this rises to about 35% for a 10% perturbation. A designer can make the tradeoff for a larger range of perturbations at the expense of accuracy, though error correction through the use of lookup tables could also be used.

Chapter 5: Conclusion

This area of research continues to provide a wealth of opportunities for improvement and novel discovery. Here it has been confirmed for 2DOF systems that a sensitivity improvement over resonant frequency based sensors of the same size is possible and is practically limited by the ratio of the grounding spring stiffness to the coupling spring stiffness. It has also been shown that 3DOF systems promise to yield even greater benefits (250% improvement) than the 2DOF systems.

It is also evident that another design iteration would be prudent in order to address the practical issues apparent in the current MEMS system. Advice for improving the existing system and avenues for future work are summarized in the following chapter. Still, the current system successfully exhibits the resonant frequency dependence of these coupled systems to perturbation while simultaneously demonstrating that the eigenvector sensitivity can be an order of magnitude larger even if a consistent trend is not readily evident. Since this was the first MEMS design to leverage energy localization at this institution, it lays the groundwork for the continuation of the area of research at UBC and gives a base off of which future researchers can build.

Chapter 6: Future Work

6.1 Further Testing on Existing Systems

Four experimental systems were designed and fabricated on each chip but only one of these systems – the large dimensioned electrostatic perturbation system – underwent complete testing. This was due to limited availability of testing equipment since the Micro System Analyzer was to be returned to Polytec for hardware upgrades over the course of several months in 2012. Therefore the first order of business for future work is the characterization of the other three systems, starting with the large dimensioned mechanical perturbation system. Since these systems were designed as a proof-of-concept for the sensing paradigm and for these specific approaches to inducing perturbation, the smaller dimensioned systems are of less importance. However, it can be seen that the electrostatic comb drive in the mechanically perturbed system could easily be replaced by an inertial mass in order to make a practical accelerometer. Therefore characterization of this approach is of the most interest. It would also be interesting to see if beam softening is the dominant effect in the system as it was in the simulation results. A wideband power amplifier may be necessary for characterizing this system since it is stiffer than the electrostatic system by design and the Polytec system signal generator is limited to ±10 V.

6.2 Account for the Time-Varying Nature of the Coupling Spring

The time-varying nature of the coupling gap can be compensated for by either a geometric design change or through feedback control of the potential across the coupling. The geometric design change could have the effective area of the

capacitance be a function of the separation gap in such a way that it offsets the cubic dependence on the coupling gap in the case of the flat-surfaced gap-varying coupling used in this research.

6.3 3DOF Experimental System

The next order of business for future work is the design, fabrication, and testing of a 3DOF system to support the analytical results presented earlier in this thesis. Another student in the research group has been taking over in this respect and should be able to provide results in several months.

6.4 Higher Order Systems: Analysis and Experiment

Since an improvement in sensitivity was found when increasing from single DOF sensors to 2DOF sensors, and again when moving to 3DOF sensors, it makes sense to explore higher order systems both analytically and experimentally. The most interesting aspect will be to optimize the order of the system for the desired sensitivity since the penalty of higher order systems is size and signal processing given that the length of the eigenvectors is equal to the number of degrees of freedom. Some thought must also be given to the method of measuring the motion of the resonators since the MSA can only measure two areas of the frame. One possibility is to move to on-chip sensing with capacitance measurements. Higher order systems also present an increase in the number of perturbation schemes which leads to longer analysis in order to compare the alternatives.

6.5 Different Perturbation Frequencies

All analysis in this thesis was performed assuming static perturbation. This was assumed valid since, when operated as a sensor, the variations in quantities of

interest are typically at a much lower frequency than the resonant modes of the oscillators. It may be interesting to explore the possibilities when the perturbation frequency approaches that of the oscillation modes. Extending this thought, the reaction of the system to perturbation signals which vary much faster than the frequency of the oscillators could also be investigated.

6.6 Generic Architecture

There are numerous resonator designs and methods of actuation in microsystems. Optimizing a generic architecture for sensing specific quantities which could be used as building blocks by other designers could prevent a lot of repetition in the design process. A well characterized design also reduces opportunities for errors in a system. By developing standard architectures, comparison between different projects would also be made easier.

6.7 Energy Domains

Finally, the veering phenomenon is not constrained to the mechanical energy domain. Some research has been started in the group toward creating sensors based on resonance in electrical circuits. The electrical domain is exciting since the size of a system is minute, and the “amplitudes” of vibration are simply electrical signals which can be measured with ease when compared to the physical masses in MEMS. The optical domain may be another path of research.

References

[1] P. Anderson, “Absence of Diffusion in Certain Random Lattices,” *Physical Review,* vol. 109, no. 5, pp. 1492-1505, March 1958.

[2] N. Mott, “Electrons in Disordered Structures,” *Advances in Physics,* vol. 16, no. 61, pp. 49-144, 1967.

[3] N. Mott, "Conduction in Non-Crystalline Systems," *Philosoph. Mag.,* vol. 17, no. 150, pp. 1259-1268, 1968.

[4] M. Cutler and N. F. Mott, “Observation of Anderson Localization in an Electron Gas,” *Physical Review,* vol. 181, no. 3, pp. 1336-1340, May 1969.

[5] March 2012. [Online]. Available: http://www.nobelprize.org/nobel_prizes/physics/laureates/1977/.

[6] P. Dean, “The Vibrational Properties of Disorder Systems: Numerical Studeis,” *Reviews of Modern Physics,* vol. 44, no. 2, pp. 127-168, April 1972.

[7] C. H. Hodges, "Confinement of Vibration by Strucutral Irregularity," *J. of Sound and Vibration,* vol. 82, no. 3, pp. 411-424, June 1982.

[8] C. H. Hodges and J. Woodhouse, "Vibration Isolation from Irregularity in a Nearly Periodic Structure: Theory and Measurements," *J. of the Acoust. Soc. of Amer.,* vol. 74, no. 3, pp. 894-905, September 1983.

[9] C. Pierre and E. H. Dowell, "Localization of Vibrations by Structural Irregularity," *J. of Sound and Vibration,* vol. 114, no. 3, pp. 549-564, 1987.

[10] C. Pierre, "Mode Localizationand Eigenvalue Veering Phenomena in Disorder

Structures," *J. of Sound and Vibration,* vol. 126, no. 3, pp. 485-502, 1988.

[11] A. W. Leissa, "On a Curve Veering Aberration," *J. of Appl. Math. and Physics,* vol. 25, pp. 99-111, 1974.

[12] R. S. MacKay and P. G. Saffman, "Stability of Water Waves," *Proc. R. Soc. Lond. A,* vol. 406, pp. 115-125, 1986.

[13] B. R. Mace and E. Manconi, "Wave motion and dispersion phenomena: Veering, Locking, and strong coupling effects," *J. Acoust. Soc. Am.,* vol. 131, no. 2, pp. 1015-1028, Feb. 2012.

[14] N. G. Stephen, "On Veering of Eigenvalue Loci," *J. of Vibration and Acoust.,* vol. 131, no. 5, pp. 054501-1-054501-5, Oct. 2009.

[15] M. Spletzer, A. Raman, A. Q. Wu, X. Xu and R. Reifenberger, “Ultrasensitive mass sensing using mode localization in coupled microcentilevers,” *Appl. Phys. Lett.,* vol. 88, no. 25, p. 254102, June 2006.

[16] M. Spletzer, A. Raman, H. Sumali and J. P. Sullivan, “Highly sensitive mass detection and identification using vibration localization in coupled microcantilever arrays,” *Appl. Phys. Lett.,* vol. 92, no. 11, p. 114102, March 2008.

[17] B. E. DeMartini, J. H. Rhoads, S. W. Shaw and K. L. Turner, "A single input-single output coupled microresonator array for the detection and identification of multiple analytes," *Appl. Physics Lett.,* vol. 93, no. 5, pp. 054102-1-054102-3, August 2008.

[18] P. Thiruvenkatanathan, J. Yan, J. Woodhouse and A. A. Seshia, "Enhancing

Parametric Sensitivity in Electrically Coupled MEMS Resonators," *J. MEMS,* vol. 18, no. 5, pp. 1077-1085, October 2009.

[19] P. Thiruvenkatanathan, J. Yan, J. Woodhouse, A. Aziz and A. A. Seshia, "Ultrasensitive mode-localized mass sensor with electrically tunable parametric sensitivity," *Appl. Physics Lett.,* vol. 96, no. 8, pp. 081913-1-081913-2, February 2010.

[20] P. Thiruvenkatanathan, J. Yan and A. A. Seshia, "Ultrasensitive Mode-Localized Micromechanical Electrometer," in *Frequency Control Symp. (FCS), 2010 IEEE International*, Newport Beach, 2010.

[21] E. Gil-Santos, D. Ramos, V. Pini, M. Calleja and J. Tamayo, "Exponential tuning of the coupling constant of coupled microcantilevers by modifying their separation," *Appl. Physics Lett.,* vol. 98, no. 12, pp. 123108-1-123108-3, March 2011.

[22] "CoventorWare Architect Reference Version 2010," Cary, 2010.

[23] "CoventorWare Designer Reference Version 2010," Cary, 2010.

[24] "CoventorWare Analyzer Reference Version 2010," Cary, 2010.

[25] K. Miller, A. Cowen, G. Hames and B. Hardy, "SOIMUMPs Design Handbook Rev. 4.0," 2004.

[26] T. Thundat, P. Oden and R. Warmack, "Microcantilever Sensors," *Microscale Thermophysical Eng.,* vol. 1, no. 3, pp. 185-199, 1997.

[27] American Wood Council, Beam Design Formulas with Shear and Moment Diagrams, Washington, 2007.

[28] Polytec, 2012. [Online]. Available: http://www.polytec.com/uk/products/vibration-sensors/microscope-based-systems/msa-500-micro-system-analyzer/.

[29] R. L. Fox and M. P. Kapoor, "Rates of Change of Eigenvalues and Eigenvectors," *AIAA J.,* vol. 256, no. 3, pp. 2426-2429, 1968.

[30] J. L. du Bois, S. Adhikari and N. A. J. Lieven, "On the Quantification of Eigenvalue Curve Veering: A Veering Index," *J. of Appl. Mech.,* vol. 78, no. 4, pp. 041007-1 - 041007-8, July 2011.

Appendices

Appendix A Derivation of Electrostatic Spring Equation

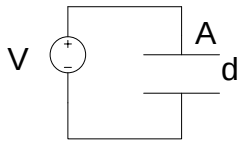

Capacitance of a parallel plate capacitor is given by with a shrinking of the gap d by amount x:

$$C = \frac{\varepsilon A}{(d - x)} \tag{A.1}$$

The energy stored in a fully charged capacitor is given by the equation:

$$E = \frac{1}{2} CV^2 = \frac{1}{2} \frac{\varepsilon A V^2}{(d - x)} \tag{A.2}$$

Force is the derivative of energy:

$$F = \frac{dE}{dx} = -\frac{1}{2} \frac{\varepsilon A V^2}{(d - x)^2} \tag{A.3}$$

Taking the first order Taylor series approximation in x:

$$F \approx -\frac{1}{2} \frac{\varepsilon A V^2}{d^2} \left(1 + \frac{2}{d} x\right) \tag{A.4}$$

The term that scales linearly with x is:

$$k_e = -\frac{\varepsilon A V^2}{d^3} \tag{A.5}$$

The equivalent spring constant formed in an electrostatic gap has the following properties:

1) Negative sign
2) Inverse cube relationship to displacement
3) Proportional to the square of the potential difference between the surfaces
4) Proportional to the mutual area of the two surfaces

Appendix B Design Parameters

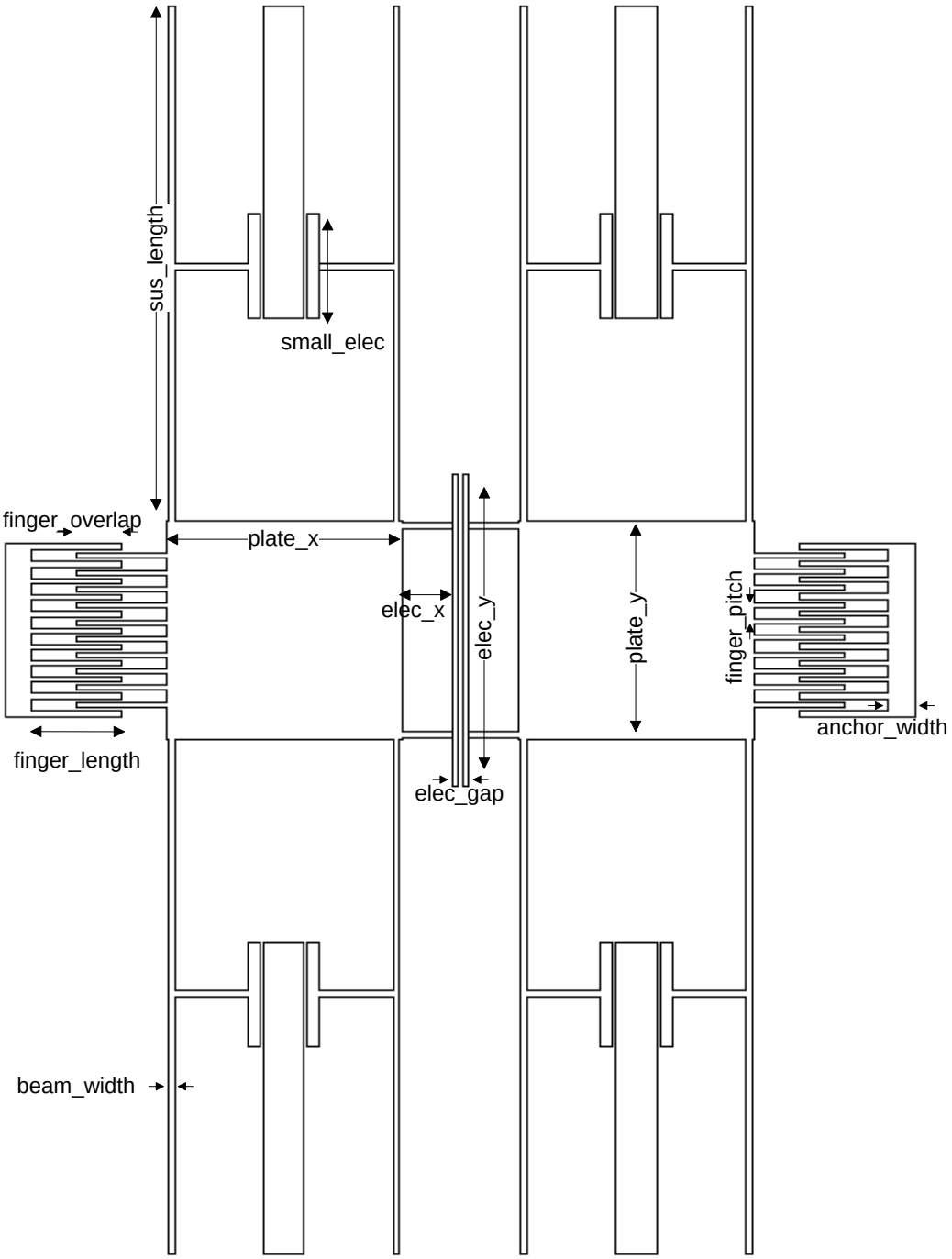

Figure B.1: Layout for electrostatically perturbed systems

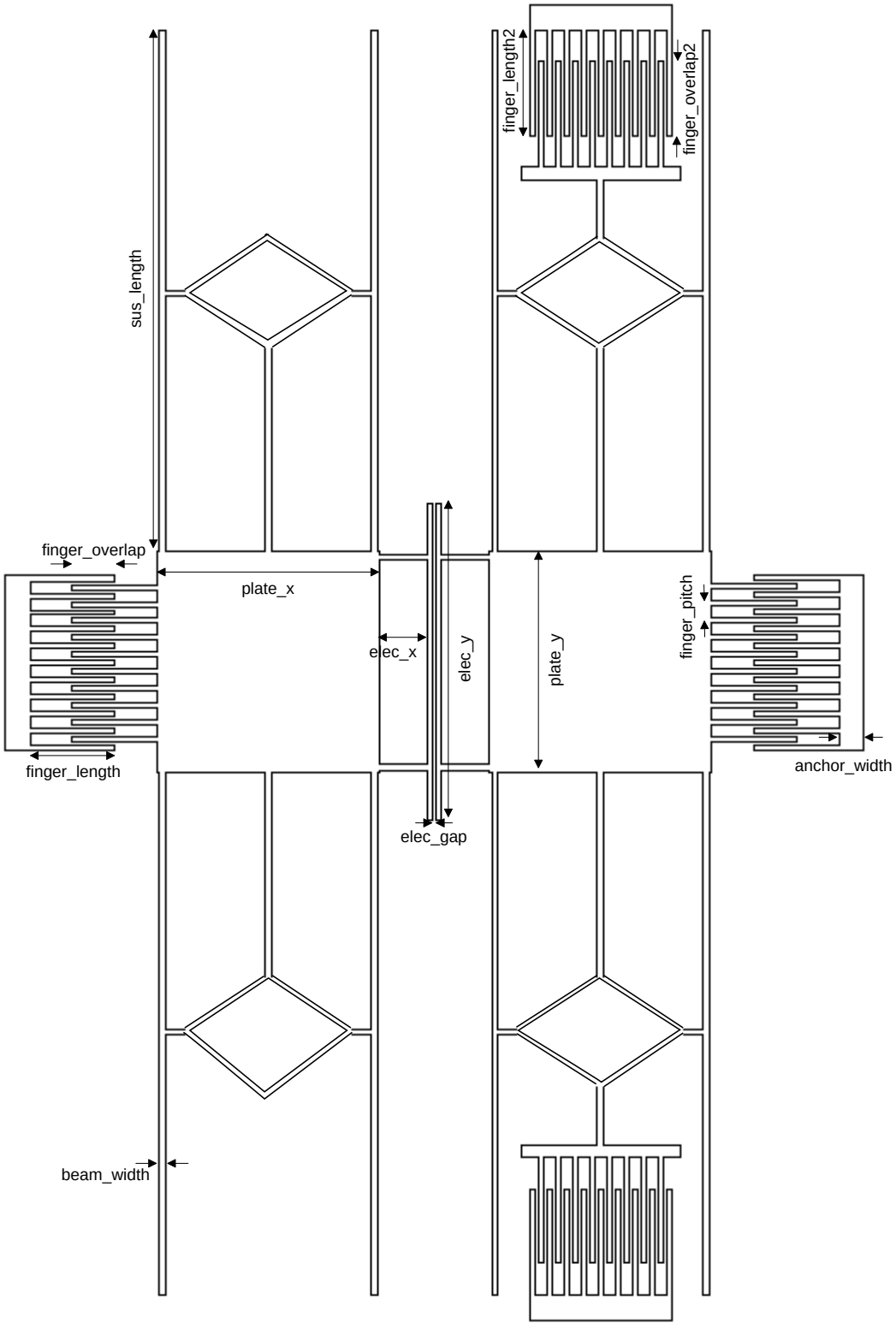

Figure B.2: Layout of mechanically perturbed systems

Table B.1: Design parameters for large and small electrostatic systems

Physical Variable	Value for Large System	Value for Small System
plate_x	210 μm	110 μm
plate_y	210 μm	110 μm
sus_length	500 μm	200 μm
beam_width	6 μm	3 μm
elec_x	50 μm	50 μm
elec_y	300 μm	200 μm
electrode_gap	2 μm	2 μm
finger_length	80 μm	80 μm
finger_width	6 μm	3 μm
finger_pitch	16 μm	10 μm
finger_overlap	40 μm	40 μm
anchor_width	24 μm	24 μm
num_combs	10	10
small_elec	100 μm	25 μm

Table B.2: Design parameters for large and small mechanical systems

Physical Variable	Value for Large System	Value for Small System
plate_x	210 μm	110 μm
plate_y	210 μm	110 μm
sus_length	500 μm	200 μm
beam_width	6 μm	3 μm
elec_x	50 μm	50 μm
elec_y	300 μm	200 μm
electrode_gap	2 μm	2 μm
finger_length	80 μm	80 μm
finger_width	6 μm	3 μm
finger_pitch	16 μm	10 μm
finger_overlap	40 μm	40 μm
anchor_width	24 μm	24 μm
num_combs	10 μm	10
finger_length2	100 μm	50 μm
finger_overlap2	70 μm	40 μm
num_combs2	8	8

Appendix C Analysis of 3DOF System

This is the full mathematical treatment of the 3DOF system with a positive perturbation to the first mass's stiffness and an equal but negative perturbation to the third mass's stiffness using the eigen derivatives method.

Unperturbed Solutions

The unperturbed mass and stiffness matrices for the 3DOF system are:

$$\boldsymbol{K} = \begin{pmatrix} k + k_c & -k_c & 0 \\ -k_c & k + 2k_c & -k_c \\ 0 & -k_c & k + k_c \end{pmatrix} \text{ and } \boldsymbol{M} = \begin{pmatrix} m & 0 & 0 \\ 0 & m & 0 \\ 0 & 0 & m \end{pmatrix} \tag{C.1}$$

The equations of motion are then summarized as:

$$\boldsymbol{M\ddot{x}} + \boldsymbol{Kx} = \boldsymbol{f} \tag{C.2}$$

Assuming a solution of $\boldsymbol{x} = [x_1 \quad x_2 \quad x_3] = \boldsymbol{u_n} e^{j\omega_n t}, n = 1,2,3$

$$\boldsymbol{M\ddot{x}} + \boldsymbol{Kx} = \boldsymbol{0} \tag{C.3}$$

$$-\omega_n^2 \boldsymbol{M u_n} e^{j\omega_n t} + \boldsymbol{K u_n} e^{j\omega_n t} = 0 \tag{C.4}$$

$$\boldsymbol{K u_n} = \omega_n^t \boldsymbol{M u_n} \tag{C.5}$$

Now the stiffness matrix is modified by scaling it by $\frac{1}{k}$:

$$\boldsymbol{K'} = \frac{\boldsymbol{K}}{k} = \begin{bmatrix} 1 + \kappa & -\kappa & 0 \\ -\kappa & 1 + 2\kappa & -\kappa \\ 0 & -\kappa & 1 + \kappa \end{bmatrix}, \kappa = \frac{k_c}{k} \tag{C.6}$$

The eigenvalue problem is then:

$$\boldsymbol{K'u_n} = \frac{\omega_n^2}{\frac{k}{m}} \boldsymbol{I u_n} = \lambda_n \boldsymbol{I u_n} \tag{C.7}$$

where λ_n is the nth eigenvalue and $\boldsymbol{u_n}$ is the associated eigenvector.

The solutions to this eigenvalue problem are as follows, noting that the mass-normalized eigenvectors ($\boldsymbol{\phi_n}$) are given, having been solved for by: $\boldsymbol{\phi_n} = \frac{\boldsymbol{u_n}}{\sqrt{\boldsymbol{u_n^T I u_n}}}$

$$\lambda_{01} = 1 \qquad \boldsymbol{\phi_{01}} = \begin{bmatrix} \frac{1}{\sqrt{3}} \\ \frac{1}{\sqrt{3}} \\ \frac{1}{\sqrt{3}} \end{bmatrix}$$

$$\lambda_{02} = 1 + \kappa \qquad \boldsymbol{\phi_{02}} = \begin{bmatrix} \frac{-1}{\sqrt{2}} \\ 0 \\ \frac{1}{\sqrt{2}} \end{bmatrix} \tag{C.8}$$

$$\lambda_{03} = 1 + 3\kappa \qquad \boldsymbol{\phi_{03}} = \begin{bmatrix} \frac{1}{\sqrt{6}} \\ \frac{-\sqrt{2}}{\sqrt{3}} \\ \frac{1}{\sqrt{6}} \end{bmatrix}$$

Applying Perturbations

For a positive perturbation on the first mass's stiffness and a negative perturbation on the third mass's stiffness, the modified stiffness matrix and mass matrix are:

$$\boldsymbol{K} = \begin{pmatrix} k + k_c + \delta & -k_c & 0 \\ -k_c & k + 2k_c & -k_c \\ 0 & -k_c & k + k_c - \delta \end{pmatrix} \text{ and } \boldsymbol{M} = \begin{pmatrix} m & 0 & 0 \\ 0 & m & 0 \\ 0 & 0 & m \end{pmatrix}, \delta = \frac{\Delta k}{k} \tag{C.9}$$

Using the eigen derivatives method, changes in the eigenvalues and eigenvectors can be found:

$$\frac{\partial \lambda_i}{\partial \delta} = \boldsymbol{\phi_i^T} \left(\frac{\partial \boldsymbol{K}}{\partial \delta} - \lambda_i \frac{\partial \boldsymbol{M}}{\partial \delta} \right) \boldsymbol{\phi_i} \tag{C.10}$$

$$\frac{\partial \boldsymbol{\phi_i}}{\partial \delta} = -\frac{\boldsymbol{\phi_i^T} \frac{\partial \boldsymbol{M}}{\partial \delta} \boldsymbol{\phi_i}}{2} \boldsymbol{\phi_i} + \sum_{r \neq i} \frac{\boldsymbol{\phi_r^T} \left(\frac{\partial \boldsymbol{K}}{\partial \delta} - \lambda_i \frac{\partial \boldsymbol{M}}{\partial \delta} \right) \boldsymbol{\phi_i}}{\Delta \lambda_{ir}} \boldsymbol{\phi_r} \tag{C.11}$$

Perturbed Eigenvalues

Solving for the sensitivity of the first eigenvalue:

$$\frac{\partial \lambda_{01}}{\partial \delta} = \boldsymbol{\phi_{01}^T}\left(\frac{\partial \boldsymbol{K}}{\partial \delta} - \lambda_{01}\frac{\partial \boldsymbol{M}}{\partial \delta}\right)\boldsymbol{\phi_{01}}$$

$$= \begin{bmatrix}\frac{1}{\sqrt{3}} & \frac{1}{\sqrt{3}} & \frac{1}{\sqrt{3}}\end{bmatrix}\left(\begin{bmatrix}1 & 0 & 0\\ 0 & 0 & 0\\ 0 & 0 & -1\end{bmatrix} - \lambda_{01}\begin{bmatrix}0 & 0 & 0\\ 0 & 0 & 0\\ 0 & 0 & 0\end{bmatrix}\right)\begin{bmatrix}\frac{1}{\sqrt{3}}\\ \frac{1}{\sqrt{3}}\\ \frac{1}{\sqrt{3}}\end{bmatrix} = \frac{1}{3} - \frac{1}{3} = 0 \qquad \text{(C.12)}$$

Similarly for the second and third eigenvalues:

$$\frac{\partial \lambda_{02}}{\partial \delta} = 0 \qquad \text{(C.13)}$$

$$\frac{\partial \lambda_{02}}{\partial \delta} = 0 \qquad \text{(C.14)}$$

Perturbed Eigenvectors

Solving for the sensitivity of the first eigenvector

$$\frac{\partial \boldsymbol{\phi_{01}}}{\partial \delta} = -\frac{\boldsymbol{\phi_{01}^T}\frac{\partial \boldsymbol{M}}{\partial \delta}\boldsymbol{\phi_{01}}}{2}\boldsymbol{\phi_i} + \sum_{r=02,03}\frac{\boldsymbol{\phi_r^T}\left(\frac{\partial \boldsymbol{K}}{\partial \delta} - \lambda_{01}\frac{\partial \boldsymbol{M}}{\partial \delta}\right)\boldsymbol{\phi_{01}}}{\Delta\lambda_{ir}}\boldsymbol{\phi_r} \qquad \text{(C.15)}$$

$$= \begin{bmatrix} 0 & 0 & 0 \\ 0 & 0 & 0 \\ 0 & 0 & 0 \end{bmatrix} \begin{bmatrix} \frac{1}{\sqrt{3}} \\ \frac{1}{\sqrt{3}} \\ \frac{1}{\sqrt{3}} \end{bmatrix} + \frac{\begin{bmatrix} \frac{-1}{\sqrt{2}} & 0 & \frac{1}{\sqrt{2}} \end{bmatrix} \left(\begin{bmatrix} 1 & 0 & 0 \\ 0 & 0 & 0 \\ 0 & 0 & -1 \end{bmatrix} - \lambda_{01} \begin{bmatrix} 0 & 0 & 0 \\ 0 & 0 & 0 \\ 0 & 0 & 0 \end{bmatrix} \right) \begin{bmatrix} \frac{1}{\sqrt{3}} \\ \frac{1}{\sqrt{3}} \\ \frac{1}{\sqrt{3}} \end{bmatrix}}{1 - (1 + 2\kappa)} \begin{bmatrix} \frac{-1}{\sqrt{2}} \\ 0 \\ \frac{1}{\sqrt{2}} \end{bmatrix} \tag{C.16}$$

$$+ \frac{\begin{bmatrix} \frac{1}{\sqrt{6}} & \frac{-\sqrt{2}}{\sqrt{3}} & \frac{1}{\sqrt{6}} \end{bmatrix} \left(\begin{bmatrix} 1 & 0 & 0 \\ 0 & 0 & 0 \\ 0 & 0 & -1 \end{bmatrix} - \lambda_{01} \begin{bmatrix} 0 & 0 & 0 \\ 0 & 0 & 0 \\ 0 & 0 & 0 \end{bmatrix} \right) \begin{bmatrix} \frac{1}{\sqrt{3}} \\ \frac{1}{\sqrt{3}} \\ \frac{1}{\sqrt{3}} \end{bmatrix}}{1 - (1 + 3\kappa)} \begin{bmatrix} \frac{1}{\sqrt{6}} \\ -\frac{\sqrt{2}}{\sqrt{3}} \\ \frac{1}{\sqrt{6}} \end{bmatrix}$$

$$= \frac{\sqrt{2}}{\sqrt{3}\kappa} \begin{bmatrix} \frac{-1}{\sqrt{2}} \\ 0 \\ \frac{1}{\sqrt{2}} \end{bmatrix} \tag{C.17}$$

$$\boldsymbol{\phi_1} = \boldsymbol{\phi_{01}} + \delta \frac{\partial \boldsymbol{\phi_{01}}}{\partial \delta} = \begin{bmatrix} \frac{1}{\sqrt{3}} \\ \frac{1}{\sqrt{3}} \\ \frac{1}{\sqrt{3}} \end{bmatrix} + \frac{\sqrt{2}\delta}{\sqrt{3}\kappa} \begin{bmatrix} \frac{-1}{\sqrt{2}} \\ 0 \\ \frac{1}{\sqrt{2}} \end{bmatrix} \tag{C.18}$$

Since all of the eigenvectors were mass-normalized (and therefore have magnitudes of 1), the sensitivity of the eigenvectors are:

$$\frac{|\boldsymbol{\phi_1} - \boldsymbol{\phi_{01}}|}{|\boldsymbol{\phi_{01}}|} = |\boldsymbol{\phi_1} - \boldsymbol{\phi_{01}}| = \left| \frac{\sqrt{2}\delta}{\sqrt{3}\kappa} \begin{bmatrix} \frac{-1}{\sqrt{2}} \\ 0 \\ \frac{1}{\sqrt{2}} \end{bmatrix} \right| = \sqrt{\frac{2}{3}} \frac{\delta}{\kappa} \approx \frac{0.82\Delta k}{k_c} \tag{C.19}$$

Similarly for the second and third eigenvectors:

$$\frac{|\boldsymbol{\phi_2} - \boldsymbol{\phi_{02}}|}{|\boldsymbol{\phi_{02}}|} = \sqrt{\frac{3}{4}}\frac{\delta}{\kappa} \approx \frac{0.87\Delta k}{k_c} \tag{C.20}$$

$$\frac{|\boldsymbol{\phi_3} - \boldsymbol{\phi_{03}}|}{|\boldsymbol{\phi_{03}}|} = \sqrt{\frac{1}{3}}\frac{\delta}{\kappa} \approx \frac{0.29\Delta k}{k_c} \tag{C.21}$$